The Effects of Static Aeroelastic Properties on Aircraft Performance and Shockwave Formation

by

Benjamin Webb

A Thesis Presented in Partial Fulfillment
of the Requirements for the Degree
Master of Science

Approved November 2022 by the
Graduate Supervisory Committee:

Timothy Takahashi, Chair
Marcus Herrmann
Ruben Perez

ARIZONA STATE UNIVERSITY

December 2022

ABSTRACT

As the push to develop ever more efficient aircraft increases, the use of lightweight composite materials to meet this push has increased. Traditional aircraft structural component sizing has revolved around the tensile yield strength of materials. Since composite materials excel in tensile strength, these traditional sizing tools provide overly optimistic weight reduction predictions. Furthermore, composite materials, in general, are weak under compression and shear. Thus, proper structural sizing yields heavier-than-expected designs.

Nevertheless, a wing using thin, lightweight composites in the primary load-bearing components significantly impacts its static aeroelastic properties. These thin structures have a decreased flexural rigidity, making them more susceptible to bending. The bending of swept wings decreases the design wing twist and dihedral angle, potentially impacting the aerodynamic performance and the lateral stability and control, respectively. This work aims to determine what, if any, are the effects of excessive static aeroelastic properties on the aerodynamic performance of an aircraft. Does the perceived gain in the theoretical reduction in structural weight outweigh the potential reduction in aerodynamic performance?

DEDICATION

This work is dedicated to my family and friends. To my family, who have supported me throughout this challenging journey. In particular, my mother and father who have always encouraged me to pursue my dreams. They have always encouraged me and pushed me to keep going during challenging times.

ACKNOWLEDGMENTS

I want to thank Dr. Takahashi for distilling all his knowledge and passion for the aerospace industry with me. Your no-nonsense and practical approach has provided me with knowledge that most may only hope to gain after years of industry experience. Your insights and help made finishing this thesis work possible, thank you.

TABLE OF CONTENTS

Page

LIST OF TABLES vi

LIST OF FIGURES vii

LIST OF SYMBOLS / NOMENCLATURE xii

CHAPTER

1 INTRODUCTION 1

Background 1

The Aerodynamics 2

The Problem 4

2 TRANSONIC AERODYNAMICS 10

Background 10

Obert's Principles of Wing Design 11

Further Insight on Swept Wing Design 13

3 CONSTRUCTING THE MODEL 17

Basis of Design 17

VORLAX 19

The Model 20

4 ANALYZING BASIS EIGENFUNCTIONS 23

Generating Basis Eigenfunctions 23

Analyzing The Response Eigenfunctions 24

CHAPTER Page

5 MODEL WING DESIGN 32

Defining Twist, Camber, and Thickness 32

6 AEROELASTIC MODEL 42

Defining The Research Space 42

Defining Wing Structure 46

Euler-Bernoulli Beam Equation 50

Aeroelastic Solver 54

7 RESULTS 61

1-gee Aeroelastic Effects 61

Aeroelastic Effects of nZ_{max} 71

Aeroelastic Effects of nZ_{min} 82

Aeroelastic Effects of Constant C_L Fuel Burn 88

8 CONCLUSION 106

REFERENCES 110

APPENDIX

A WIDEBODY AIRCRAFT DATA 113

LIST OF TABLES

Table Page

1. Key Model Dimensions 20
2. Sample Wing t/c and Camber Distribution 24
3. Model Wing Twist, Thickness, and Camber Distribution 35
4. Design Flight Conditions 35
5. Comparison of Measured C_p 39
6. Key Aircraft/Wing Inertial Loads 44
7. Derated Tensile Strengths of Each Model 46
8. 1-gee Aeroelastic Wing Twist and Dihedral Angle 65
9. Key Aircraft/Wing Inertial Loads at MTOW x nZ_{max} 72
10. Wing Washout at nZ_{max} 74
11. Key Aircraft/Wing Inertial Loads at MTOW x nZ_{min} 82
12. Lift-Induced Drag (CD_i) at Several Fuel Loads 99
13. Dimensionalize CD_i for Each Model 100
14. Maximum Upper Surface C_P and M_{cr} for Each Model 104

LIST OF FIGURES

Figure Page

1. The Flexibility of Boeing 787 Wing 2
2. Example of Wing Twist on CF-18 3
3. Projection of Transverse Bending into the Wind Reference Frame 8
4. Carbon-Fiber Laminate used in Boeing 787 Wing 18
5. Carbon-Fiber Sandwich used in Boeing 787 Wing 18
6. Flat-Plate Model in VORLAX 21
7. Sandwich Model in VORLAX 21
8. Example Lift Perturbation Response 25
9. Optimized Lift Perturbation Eigenvalues 26
10. Twist Only Optimized Lift Distribution 27
11. Midspan Cross-Sectional Pressure Distribution 28
12. Outer Midspan Cross-Sectional Pressure Distribution 29
13. Upper Surface Critical Flow Regions 30
14. Comparison of Baseline Airfoil Geometry 33
15 NACA 64 Camber Profile and Model Airfoil 34
16. Design Wing Twist Distribution 36
17. Design Wing Thickness Distribution 36
18. Chordwise Profile of Control Points 1 and 2 37
19. Chordwise Profile of Control Points 4 and 6 37
20. Chordwise Profile of Control Points 8 and 12 38

Figure Page

21. Spanwise Lift Distribution of Wing 39

22. Upper Surface Pressure Distribution of Wing 39

23. Upper Surface Critical Flow Conditions 40

24. Aero-Reference Frame 43

25. Inertial Loads of the 46-ksi Model 45

26. Sketch of Wing Torque Box Structure 47

27. Resolving of the Wing Bending Moment into Forces 48

28. Wing Shear Force at 1-gee for 46-ksi Wing 52

29. Wing Bending Moment at 1-gee for 46-ksi Wing 52

30. Wing Deflection Slope at 1-gee for 46-ksi Wing 53

31. Wing Deflection at 1-gee for 46-ksi Wing 53

32. Aeroelastic Twist at 1-gee for 46-ksi Wing 54

33. Aeroelastic Dihedral at 1-gee for 46-ksi Wing 54

34. 1-gee Aeroelasticity Solution Procedure 59

35. Load Factor and Constant C_L Fuel Burn Solution Procedure 60

36. Aeroelastic Twist for 46-ksi Wing 61

37. Aeroelastic Dihedral for 46-ksi Wing 62

38. Aeroelastic Twist for 69-ksi Wing 62

39. Aeroelastic Dihedral for 69-ksi Wing 63

40. Aeroelastic Twist for 105-ksi Wing 63

41. Aeroelastic Dihedral for 105-ksi Wing 64

42. Aeroelastic Twist for 180-ksi Wing 64

Figure Page

43. Aeroelastic Dihedral for 180-ksi Wing 65

44. Jig Twist for 46-ksi Wing 66

45. Relative Jig Height for 46-ksi Wing 67

46. Jig Twist for 69-ksi Wing 67

47. Relative Jig Height for 69-ksi Wing 68

48. Jig Twist for 105-ksi Wing 68

49. Relative Jig Height for 105-ksi Wing 69

50. Jig Twist for 180-ksi Wing 69

51. Relative Jig Height for 180-ksi Wing 70

52. Wing Twist at nZ_{max} for 46-ksi Wing 72

53. Wing Twist at nZ_{max} for 69-ksi Wing 73

54. Wing Twist at nZ_{max} for 105-ksi Wing 73

55. Wing Twist at nZ_{max} for 180-ksi Wing 74

56. Wing Deflection at nZ_{max} for 46-ksi Wing 75

57. Wing Deflection at nZ_{max} for 69-ksi Wing 75

58. Wing Deflection at nZ_{max} for 105-ksi Wing 76

59. Wing Deflection at nZ_{max} for 180-ksi Wing 76

60. Spanwise Lift Distribution at nZ_{max} for 46-ksi Wing 77

61. Spanwise Lift Distribution at nZ_{max} for 69-ksi Wing 78

62. Spanwise Lift Distribution at nZ_{max} for 105-ksi Wing 78

63. Spanwise Lift Distribution at nZ_{max} for 180-ksi Wing 79

64. Upper Surface Critical Flow at nZ_{max} for 46-ksi Wing 80

Figure Page

65. Upper Surface Critical Flow at nZ_{max} for -69-ksi Wing 80

66. Upper Surface Critical Flow at nZ_{max} for 105-ksi Wing 81

67. Upper Surface Critical Flow at nZ_{max} for 180-ksi Wing 81

68. Wing Twist at nZ_{min} for 46-ksi Wing 83

69. Wing Twist at nZ_{min} for 69-ksi Wing 83

70. Wing Twist at nZ_{min} for 105-ksi Wing 84

71. Wing Twist at nZ_{min} for 180-ksi Wing 84

72. Wing Deflection at nZ_{min} for 46-ksi Wing 85

73. Wing Deflection at nZ_{min} for 69-ksi Wing 86

74. Wing Deflection at nZ_{min} for 105-ksi Wing 86

75. Wing Deflection at nZ_{min} for 180-ksi Wing 87

76. Wing Twist at 80% Fuel Load 88

77. Wing Twist at 60% Fuel Load 89

78. Wing Twist at 40% Fuel Load 89

79. Wing Twist at 20% Fuel Load 90

80. Wing Deflection at 80% Fuel Load for 46-ksi and 180-ksi Wings 91

81. Wing Deflection at 60% Fuel Load for 46-ksi and 180-ksi Wings 91

82. Wing Deflection at 40% Fuel Load for 46-ksi and 180-ksi Wings 92

83. Wing Deflection at 20% Fuel Load for 46-ksi and 180-ksi Wings 92

84. Wing Twist as a Function of the Fuel Load at the Wingtip 94

85. Wing Twist as a Function of the Fuel Load at the ¾ Semi-Span 94

86. Wing Twist as a Function of the Fuel Load at the ½ Semi-Span 95

Figure Page

87. Wing Twist as a Function of the Fuel Load at the ¼ Semi-Span 95

88. Spanwise Lift Distribution of 46-ksi and 180-ksi Wings at 80% Fuel Load 97

89. Spanwise Lift Distribution of 46-ksi and 180-ksi Wings at 60% Fuel Load 97

90. Spanwise Lift Distribution of 46-ksi and 180-ksi Wings at 40% Fuel Load 98

91. Spanwise Lift Distribution of 46-ksi and 180-ksi Wings at 20% Fuel Load 98

92. Upper Surface Critical Flow of 46-ksi and 180-ksi Wings at 80% Fuel Load .101

93. Upper Surface Critical Flow of 46-ksi and 180-ksi Wings at 60% Fuel Load .101

94. Upper Surface Critical Flow of 46-ksi and 180-ksi Wings at 40% Fuel Load .102

95. Upper Surface Critical Flow of 46-ksi and 180-ksi Wings at 20% Fuel Load .102

96. Upper Surface Pressure of 46-ksi and 180-ksi Wings at 80% Fuel Load 103

97. Upper Surface Pressure of 46-ksi and 180-ksi Wings at 60% Fuel Load 103

98. Upper Surface Pressure of 46-ksi and 180-ksi Wings at 40% Fuel Load 103

99. Upper Surface Pressure of 46-ksi and 180-ksi Wings at 20% Fuel Load 104

LIST OF SYMBOLS/ NOMENCLATURE

AoA	= Angle of Attack	[°]
$\bar{c}$	= Average Chord Length	[ft]
CD_i	= Induced-Drag Coefficient	
C_L	= Lift Coefficient	
C_P	= Pressure Coefficient	
C_P^*	= Critical Pressure Coefficient	
EI	= Flexural Rigidity	[lb-in^2]
FOS	= Factor of Safety	
F_{ty}	= Material Tensile Yield Strength	[ksi]
I	= Area Moment of Inertia	[in^4]
$M(y)$	= Bending Moment	[ft-lb]
M_{cr}	= Critical Mach Number	
M_{DD}	= Drag Divergence Mach Number	
$MTOW$	= Maximum Takeoff Weight	[lbm]
nZ_{max}	= Maximum Limit Maneuvering Load	
nZ_{min}	= Minimum Limit Maneuvering Load	
$P(y)$	= Applied Wing Force	[lbf]
$V(y)$	= Wing Shear Force	[lbf]
VLM	= Vortex Lattice Method	
$w(y)$	= Aeroelastic Wing Deflection	[in]
θ	= Wing Bending Slope	
$\Phi(y)$	= Aeroelastic Wing Dihedral	[°]
$\Psi(y)$	= Aeroelastic Wing Twist	[°]
λ	= Ratio of Specific Heats	[1.4 for air]
Λ	= Wing Sweep Angle	[°]

CHAPTER 1

INTRODUCTION

Background

Powered flight is a remarkable achievement that requires the aircraft design team to find a balance between aerodynamics, propulsion, stability and control, and structures. Each of these specialties comes with competing interests and nuances that must be well understood throughout the team. As designs continue to evolve and modern designs are introduced, there has been a push in the industry and society to create ever more efficient aircraft. The quest for more efficient designs has been achieved primarily through three major factors. The first is the immense increase in propulsive efficiency. The second is the use of slender, high-aspect-ratio wings. The third is the use of advanced alloys and composite materials in the construction of an aircraft and, of particular interest, the construction of the wings.

The second and third factors compete, which often leads to unintended outcomes. The aerodynamicists use these slender, high-aspect-ratio wings to reduce drag and increase aerodynamic efficiency. From an aerodynamicist's perspective, the goal is to minimize all forms of drag as much as reasonably possible. Structural engineers use high-strength metal alloys and composite materials to increase fuel efficiency and reduce emissions. The theoretical increase in fuel efficiency that can be found in using these materials stems from the need to use less material in constructing the primary load-bearing structural components of the wings. All things being equal, the need to use less material leads to decreased aircraft weight, leading to decreased fuel burn and emissions.

It should be noted that reducing the drag as much as reasonably possible, leads to a decrease in fuel burn and emissions if all other factors are equal. However, in this work, the focus is on aerodynamic efficiency. A notable example of these two competing factors at work is the Boeing 787 aircraft shown in Figure (1).

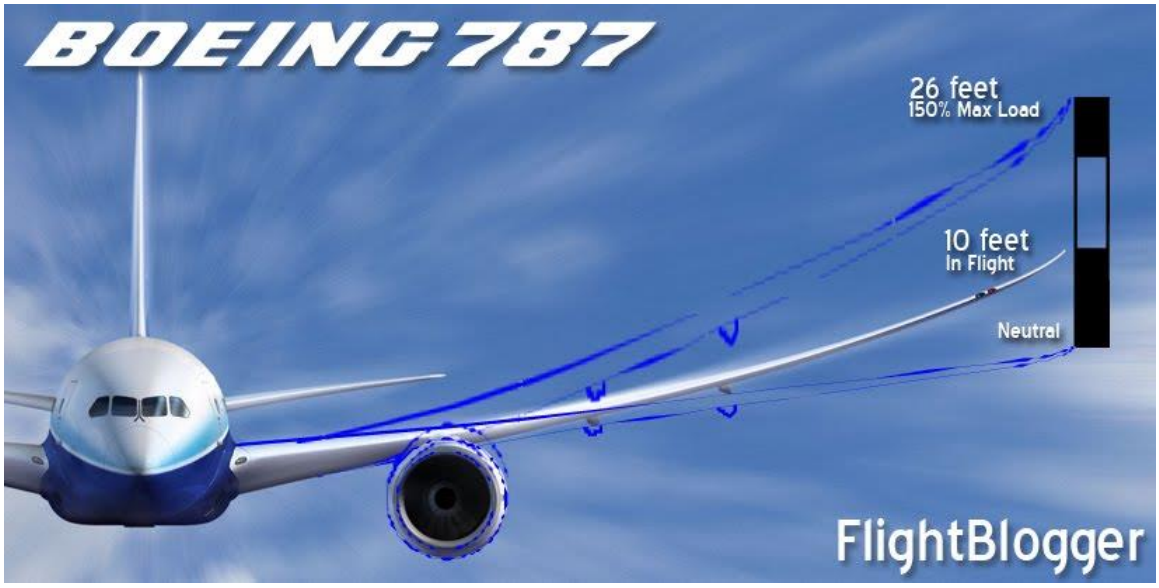

Figure 1. The Flexibility of Boeing 787 Wing. [1]

The Aerodynamics

Figure (1) illustrates a potentially unexpected outcome when the second and third factors compete without understanding the nuances involved with wing design and aerodynamics. Figure (1) shows the incredible flexibility the 787 wing demonstrates during flight. At design cruise conditions, the Boeing 787 wing flexes upwards by ten feet from the jig position, i.e., when the aircraft is on the ground and the wing is not generating any lift. This amount of flexibility has the potential to alter the fundamental aerodynamic design characteristics of the wing.

The design of a modern transonic wing is incredibly nuanced. While a wing design may seem relatively simple to a casual viewer, it features a complex distribution of twist, camber, and wing thickness. Incorporating control surfaces and high-lift devices will further increase the complexity of the design. Thus, wing twist, the geometric incidence of any airfoil on the wing, is a critical aspect of aircraft wing design.

Figure 2. Example of Wing Twist on CF-18. [2]

Figure 2 shows the change in wing twist from the root to the tip of the wing on a CF-18 Hornet jet. The CF-18 features about four degrees of washout [2], which means that the wingtip is tilted four degrees below the root of the wing. Wing washout is often necessary to achieve an elliptical spanwise lift distribution. An elliptical lift distribution is desired to minimize lift-induced drag [3]. As Max Munk said, "The induced drag is an evil, because all drag is an evil, but it is a necessary evil at least and expended for something we want" [3]. In this vein, an aircraft wing designer wishes to minimize, as much as possible, the amount of lift-induced drag. Thus, a variation of wing twist is needed, often with washout, to achieve an elliptical lift distribution.

A second potentially unexpected outcome of not fully understanding the coupling of various aspects of the aerodynamics of an aircraft wing is the change in the pressure distribution across the wing due to changes in the wing geometry. Not only does an aircraft wing designer wish to minimize the amount of lift-induced drag, but they also seek to minimize the transonic pressure drag that occurs from the presence of shockwaves. The pressure distribution across a wing heavily depends on wing twist, camber, and thickness. Thus, changing the wing twist can significantly impact the pressure distribution. This change in the pressure distribution affects the introduction and propagation of shockwaves. Unfortunately, this aerodynamic design goal has the potential to run counter to the structural design goal of minimizing the structural weight.

To answer the question of when or at what pressure a shockwave forms, the designer can turn to the critical pressure coefficient, Cp^*. The critical pressure coefficient is the pressure coefficient at which the flow around the wing transitions from subsonic to supersonic flow. The specifics of the critical pressure and its corresponding critical Mach number, M_{cr}, are discussed later.

The Problem

A significant emphasis has been placed on reducing aircraft weight to increase fuel efficiency, often as it seems to the detriment of the aircraft's aerodynamic performance. Much interest has been placed in using lightweight carbon fiber composite materials in aircraft construction to reduce weight. Many carbon fiber composites have stronger tensile strength properties than traditional aerospace aluminum alloys, and some are even on par with steel [4]. However, these composites are lighter than steel and

aluminum [4]. By using carbon fiber composite materials in the construction of the load-bearing structural components of the wing, the design team can save a significant amount of weight in theory. Furthermore, because many of these composites have strength properties that are significantly greater than traditional aluminum alloys, less of the composite material can be used. This introduces yet even more potential weight savings.

While using carbon fiber composite materials may seem like a perfect choice in aircraft construction, a couple of essential issues must be addressed and better understood. The first issue is that a carbon fiber composite material is traditionally strong in tension but weak under compressive loads [5]. During flight, one side of the wing torque box is always under tension and the other under compression. During typical positive gee scenarios, the lower surface of the torque box is under tension as the wing flexes upwards, while the upper surface is under compression. Conversely, the lower surface is under compression during a negative gee maneuver while the upper surface is in tension. During typical cruise conditions, the wing experiences positive one-gee forces; thus, the upper surface is under compression. The ply orientation of the composite material can be altered between the upper and lower surfaces to help alleviate some of the weakness in compression. Additional material could be added on the upper surface to help increase the compressive strength, but this could reduce the expected weight savings.

Furthermore, this cannot prevent all scenarios in which a part of the wing experiences a substantial compressive load. Wind gusts impart a temporary oscillatory

aerodynamic force on the wing. This oscillatory force can introduce compressive forces on both sides of the wing.

Additionally, composite materials may not fail at the macro level yet still suffer from failure at the individual ply level [4]. Over time the failures of individual plies will not only cause additional maintenance but could easily lead to catastrophic failure at the macro level of the composite. There is also a concern regarding the fatigue life of composite materials. Traditional materials, like aluminum, have well-documented fatigue life and analysis procedures, which stems from the overall isotropic nature of metals. Composites, on the other hand, are anisotropic. The overall fatigue life, as well as the analysis of the fatigue life of composite materials, is not nearly as well understood as it is for metal alloys [4].

Considering all this, the design team must design the wing to avoid the most critical failure mode, i.e., the mode that fails first. In this case, the weak compressive strength of composite material causes it to fail under compression before it fails under tension. Thus, additional material may need to be added to the structural components to avoid this failure. The additional material could lead to a wing design that does not have the theoretical weight savings initially implied by composite materials.

Traditional aircraft structural sizing, including wing structural sizing, is based on the tensile yield strength of a material [6]. Since composites generally excel in tensile strength, these traditional sizing techniques provide overly optimistic weight estimations based on unfulfillable designs [5].

The second key issue is that any structural component of a wing, whether constructed of aluminum or a carbon fiber composite, sees a reduction in its flexural rigidity, *EI*, as the cross-sectional area of the component decreases.

$$EI = E\left(\frac{bh^3 - b_1h_1^3}{12}\right) \quad (1)$$

Equation (1) shows the flexural rigidity of a hollow rectangle with an outer height and width of h and b and an inner height and width of h_1 and b_1. This equation can be used to model the torque box of a wing, which can be thought of as the wing skeleton. When the material thickness of the torque box becomes thinner, the inner height and width, h_1 and b_1, increase since the hollowed-out portion of the torque box increases in volume. As b_1 and h_1 increase, I decreases. This decrease in I decreases the flexural rigidity of the wing torque box, making it more susceptible to excessive bending and deformation.

Furthermore, with long, slender wings, the moments caused by the aerodynamic forces increase with this increased wingspan, further magnifying the effect of decreased flexural rigidity. In addition, modern, high-aspect-ratio wings increasingly have less volume near the outboard sections of the wings. This decreased volume necessitates the use of even smaller, thinner structural components. All this is taken to mean that thin, lightweight structural components in a wing can lead to a significant amount of wing flex, as shown on the Boeing 787 in Figure (1).

The increased flexibility of a long, high-aspect-ratio wing constructed primarily of composite material could decrease the aerodynamic performance and efficiency of the aircraft. This aerodynamic performance and efficiency decrease are attributable to

changes in the wing twist. Almost all wings used on transonic aircraft today are swept wings. The swept wing increases the critical Mach number by reducing the velocity normal to the wing's leading edge. This normal velocity dictates the critical Mach number of a particular wing section. Unfortunately, this sweeping of the wing causes the bending of a wing to be not straightforward.

As a swept wing bends up and down along its principal axis, the projection of this bending into the wind axes is seen as a change in wing dihedral and wing twist. In this context, the wing twist and dihedral are referred to as the aeroelastic twist and dihedral to distinguish them from the design wing twist and dihedral. The aeroelastic twist and dihedral are departures from the design twist and dihedral. The departure of the wing twist degrades the wing's aerodynamic efficiency, while the departure in the wing dihedral angle can alter the aircraft's lateral stability and control characteristics. The projection of the wing bending into the wind reference frame is demonstrated in Figure (3).

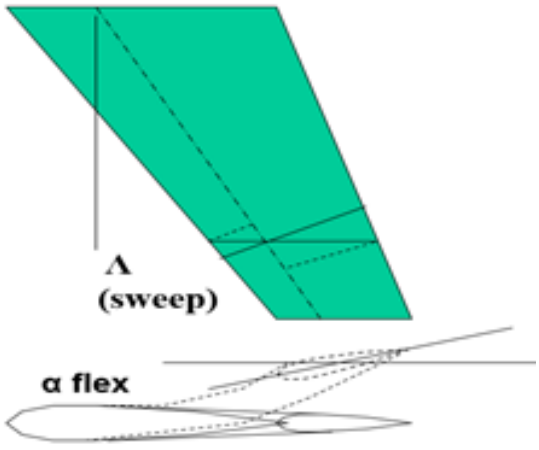

Figure 3. Projection of Transverse Bending into the Wind Reference Frame. [7]

The design of an efficient transonic wing is complex. The design team needs to have a solid understanding of all disciplines, particularly aerodynamics and structures. A truly optimal design will find the proper balance between weight reduction and aerodynamic performance. This work aims to show how a complete disregard for the aeroelastic effects in the name of weight reduction can lead to a wing design that shows no increase in efficiency or possibly a decrease in efficiency.

CHAPTER 2

TRANSONIC AERODYNAMICS

Background

Designing a transonic wing is a complicated process. Unlike wings designed for purely subsonic or supersonic flight, transonic wings must be able to work efficiently with a mixture of subsonic and supersonic flow. Ideally, for a clean-sheet design, the design team would select a wing geometry that develops optimal flow conditions across various flight conditions. The broader the range of flight conditions, the higher the overall efficiency and usefulness of the design. Here, "optimal flow" means flow with a well-defined transverse lift distribution to minimize the unfortunate but necessary lift-induced drag and a well-defined chordwise pressure distribution that minimizes the pressure drag associated with shockwaves. In essence, this becomes a problem of fitting a wing that generates a desired spanwise and chordwise pressure distribution.

The desired spanwise pressure distribution should create an elliptical spanwise lift distribution. In reality, a perfectly elliptical spanwise lift distribution is not achieved due to the presence of the fuselage, but as is shown, the elliptical lift distribution can be achieved over 80%-90% of the wingspan.

The desired chordwise pressure distribution must account for the critical Mach number (M_{cr}) and C_p^*. The critical Mach number and its corresponding critical pressure coefficient are the Mach number and pressure coefficient at which the flow accelerates from subsonic to supersonic. In theory, using standard analytical methods would allow

for the easy calculation of the pressure at a given wing airfoil section. From this, the designer can adjust the wing twist, camber, and thickness to keep the calculated pressure coefficient less than the critical pressure coefficient. However, it has been well documented that many of these common analytical aerodynamic analyses, including blade-element theory, thin-airfoil theory, and classical simple sweep theory, fail to properly account for the highly three-dimensional flow-field generated by a finite wing [8]. Thus, numerical tools are needed to determine the pressure distribution and develop the complex wing shapes needed to obtain the desired distribution.

Obert's Principles of Wing Design

A good transonic wing design minimizes the lift-induced drag by generating, as close as possible, an elliptical spanwise lift distribution while keeping the critical Mach number below the drag divergence Mach number (M_{DD}). Ideally, the optimal design would be shock-free at the design cruise point. This is often not possible, especially at higher transonic Mach numbers. However, this does not necessarily spell disaster for the optimal wing design. While it is often impossible to keep the wing completely shock-free, a practical design can be found if the wing's critical Mach number remains below the drag divergence Mach number. The drag divergence Mach number is the Mach number of a given wing airfoil section at which the drag begins to rise rapidly in proportion to increasing Mach number [9]. The pressure coefficient that correlates to the drag divergence Mach number is typically around 20% greater than the critical pressure coefficient, C_p^*. Thus, an effective transonic wing design can be found with weak and well-structured shockwaves.

In his book *Aerodynamic Design of Transport Aircraft*, Obert gives four characteristics that a wing should achieve [10].

1) An as high as possible lift-curve gradient
2) An as high as possible maximum lift coefficient
3) An as low as possible drag
4) An as high as possible angle-of-attack where flow separation occurs

These characteristics suggest that an effective wing design maximizes its lift capabilities while reducing all contributions to drag. These contributions to drag include lift-induced drag and drag associated with flow separation. The strong, adverse pressure gradient associated with a strong shockwave often leads to flow separation.

Therefore, given a design cruise speed and altitude, an effective transonic wing design generates the required amount of lift at as low an angle of attack as reasonably possible. The aerodynamic shape of this wing is such that when the whole wing is pitched to its required angle of attack, the wing develops pressure isobar patterns that integrate up to have an elliptical spanwise lift distribution that minimizes lift-induced drag. At the same time, these pressure isobar patterns keep the upper surface velocities low enough that strong shockwaves do not form; this avoids lift and drag divergence.

In his book, Obert provides insight into the aerodynamic characteristics that should be incorporated into an effective wing design. He recommends a design where the

pressure isobars are aligned with the leading-edge sweep. To achieve this isobar alignment, Obert suggests using the following design features [10]:

- Increasing the thickness-to-chord ratio near the wing/fuselage junction.
- Decreasing the positive camber or even applying negative camber to the root section.
- Increasing the incidence of the root section, via twist.

The process of applying these features and the resulting wing design is discussed later. For now, a continued discussion on transonic wing design.

Further Insight on Swept Wing Design

The use of leading-edge sweep is almost a requirement for transonic wing design. Without it, most, if not all, practical designs would go beyond the drag divergence Mach number. Thus, wing sweep is necessary, and now the question of how the critical pressure coefficient is affected by wing sweep is posed.

The idea of wing sweep predates WWII and was first proposed by Adolf Busemann in 1935 [11]. Realize that this is before the jet age, before there were even aircraft that were truly capable of transonic or supersonic flight. Despite this early realization of the benefits of wing sweep, Kirkman & Takahashi show that there was a significant amount of qualitative evidence that shows that wing sweep increases the critical Mach number but little solid quantitative evidence [11]. What makes matters

more troubling is that the few proposed critical pressure coefficient predicting equations vary widely in their accuracy and underlying theory.

To successfully design a transonic wing, it is vital to have a relatively simple method of determining the critical pressure coefficient without requiring expensive CFD simulations for every configuration, flight condition, and control perturbation. Fortunately, the work of Kirkman & Takahashi [11] analyzed the different proposed equations and found that Küchemann's equation [12], shown in Equation (2), accurately predicts the critical pressure coefficient of an infinite-span swept wing.

$$C_p^* = \frac{2}{\lambda M_\infty^2}\left\{\left(\frac{2}{\lambda+1}\right)^{\frac{\lambda}{\lambda-1}}\left(1+\frac{\lambda-1}{2}(M_\infty\cos(\Lambda))^2\right)^{\frac{\lambda}{\lambda-1}}-1\right\} \quad (2)$$

Küchemann derived this equation using thermodynamics, and it has been shown to accurately predict the critical pressure of an infinite-span swept wing [6]. That, however, is the caveat from solely relying on this equation.

It has been well documented that no real, finite-span wing behaves exactly like its two-dimensional infinite-span counterpart [11]. A finite-span wing has a highly three-dimensional flow field; the amount of three-dimensionality depends primarily on the aspect ratio and span of the wing. Nevertheless, as is shown later, Küchemann's equation is still a useful design tool when used correctly and provides an important design insight. If the flow normal to the leading edge is subsonic, a wing can be subcritical, even in transonic or supersonic flow. Furthermore, Küchemann suggests that it is not so much the flow normal to the leading edge that is important; instead, it is the flow normal to the pressure isobars that determines the critical condition of a flow. This insight is

reminiscent of Obert's recommendation about aligning the pressure isobars with the leading edge.

Further insight is provided by Neumark, who posits that a significant amount of the loss in theoretical performance of a swept wing is attributable to the highly three-dimensional flow field around the wing/fuselage junction [13]. Neumark agrees with Obert [10] and Küchemann [12] that the flow becomes critical when the component normal to the pressure isobar reaches Mach one. He notes that as the isobars cross the centerline of the wing, i.e., the fuselage, they unsweep. Further, wings with taper ratios of less than one see the sweep angle decrease as the flow proceeds across the chord from the leading to the trailing edge. Thus, there will necessarily be parts of the wing that have their pressure isobars perpendicular to the oncoming flow. The acceleration of the total velocity component over the top of the wing will likely subject it to critical conditions. This is undoubtedly the case at supersonic speeds since the oncoming flow is already critical. At higher transonic speeds, it is likely that critical conditions are also met. Neumark's point is that it is almost impossible to achieve subcritical flow over the entire wing/fuselage for most, if not all, transonic and supersonic wings.

Neumark further suggests that the critical Mach number is not a single value but a range of Mach numbers [13]. Specifically, each wing section has a lower and upper critical Mach number. The upper critical Mach number corresponds to the critical Mach number of the swept wing, while the lower critical Mach number corresponds to the critical Mach number of the wing as if it were unswept. Just as there are now two critical

Mach numbers, there are also two critical pressure coefficients. One corresponds to each of the critical Mach numbers.

The idea of a range of critical Mach numbers and pressure coefficients, bookended by the upper and lower critical Mach numbers, is further confirmed by Newby in work done at the RAE [14]. Newby suggests that a key point when designing a transonic wing is that the critical pressure coefficient is calculated to the local geometric sweep of the wing. This means that the critical pressure coefficient must be calculated across a grid of points that cover the wing surface. The critical pressure coefficient at each point is calculated using the sweep at that point; thus, the un-sweeping of a tapered wing is accounted for in the critical pressure coefficient.

CHAPTER 3

CONSTRUCTING THE MODEL

Basis of Design

The inspiration for this work came from the modern aircraft designs of the Boeing 787 and Airbus A350. Both aircraft use carbon-fiber composite material extensively throughout the design, including the wing. The extreme amount of flex seen in the Boeing 787 wing, see Figure (1), poses an interesting question. What is the effect of excessive static aeroelastic properties on the aerodynamic efficiency of a wing? The Boeing 787 is marketed as a "new-age" design to be significantly more fuel-efficient than previous designs.

One aspect that provides the Boeing 787 with increases in fuel efficiency and decreases in emissions is the use of modern high-bypass ratio engines. The Boeing 787 is powered by a pair of either Rolls-Royce Trent 1000 turbofans or General Electric GEnx turbofans, both giving a 15% - 20% reduction in fuel burn compared to previous generations of high-thrust turbofans [15] [16].

The other aspect that Boeing claims to help make the 787 more green and fuel-efficient is the extensive use of carbon-fiber composite materials. Boeing says the 787 comprises 50% carbon-fiber materials by weight [17]. Figures (4) and (5) show that most of the wing is constructed with carbon-fiber composites.

Figure 4. Carbon-Fiber Laminate used in Boeing 787 Wing [17]

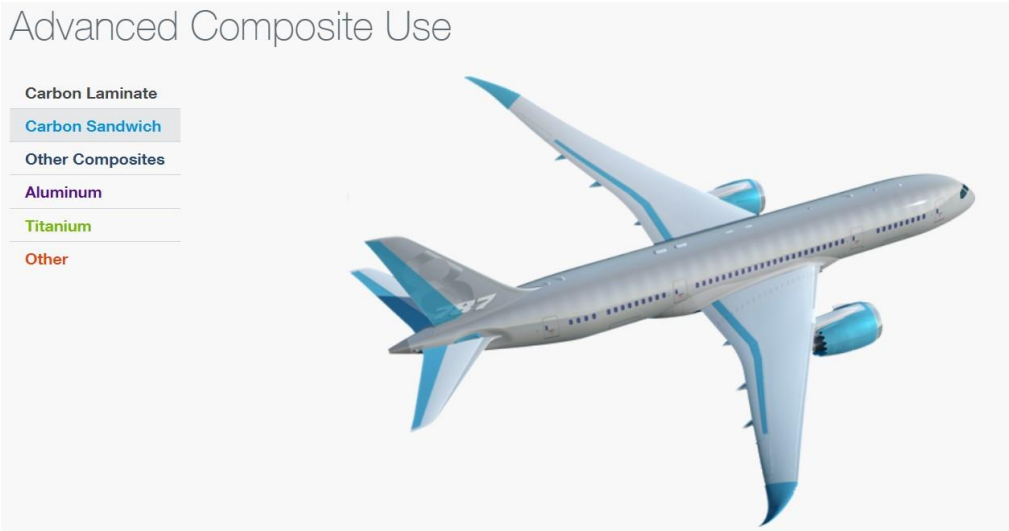

Figure 5. Carbon-Fiber Sandwich used in Boeing 787 Wing [17]

As has already been discussed, the extensive use of carbon-fiber composites should significantly reduce the structural weight of the Boeing 787 aircraft. This reduction in the structural weight should either reduce the operational weight of the aircraft or allow more of the operational weight to be used for increased payload. Either way reduces fuel consumption per person or lb of payload.

VORLAX

Since the Boeing 787 was the primary inspiration for this work, it was decided to create a model for a long-range wide-body airliner with a high aspect ratio wing. The goal is to have a simple model that can be used as an input into a potential flow vortex lattice (VLM) aerodynamic solver. The reasons for using a VLM solver over a compressible Euler or Navier-Stokes-based solver came from the simplicity and computational cost/time. This work is not meant to be an in-depth aeroelastic analysis of the model aircraft. Instead, it is intended to be a conceptual design-level analysis of the effects of static aeroelasticity on wing efficiency. Therefore, a need for many simulations to be run necessitated quick simulations.

The software chosen for this study was a combination of MATLAB and VORLAX. VORLAX is a steady potential flow VLM solver initially developed in 1977 by Luis Miranda et al. at Lockheed under contract for NASA [18]. Over the years, this code has been maintained and updated by Professor Takahashi. Recently, a former student of Professor Takahashi, Tyler Souders, implemented a number of performance improvements that have significantly improved the simulation speed of VORLAX [19]. Furthermore, the author has previously used VORLAX in other academic work and has found that it provides reliable aerodynamic data at the conceptual design level.

VORLAX is an incompressible potential flow solver, but Prandtl-Glauert compressibility corrections are applied for the pressure, forces, and moments [18]. This provides useful data at the conceptual design level. The one major drawback to a potential flow solver is its inviscid nature. Because of this, it cannot model the presence

of shockwaves. However, it can identify the points in the flow field that reach or exceed the critical pressure coefficient. Kirkman & Takahashi's [11] work found that Küchemann's [12] critical pressure coefficient equation accurately predicts the formation of a shockwave on a three-dimensional swept wing using the pressure coefficients calculated by VORLAX. Their work justifies using a potential flow solver combined with Küchemann's equation to predict the onset of shockwave formation. Remember that this work is not intended to be at the analysis or verification level of the model. Instead, it is oriented towards a conceptual design level or design trade studies.

The Model

The aircraft geometry is chosen to represent a long-range wide-body airliner with a high aspect ratio wing, reminiscent of the Boeing 787. The key model dimensions chosen are shown in Table (1).

S_{ref}	3700 ft^2
$\bar{c}$	18.5 ft
Span	200 ft
Aspect Ratio	10.8
Taper Ratio	0.25
Leading-Edge Sweep	35°
Dihedral Angle	5°
Fuselage Length	200 ft
Fuselage Width	20 ft

Table 1. Key Model Dimensions

In this work, two versions of the model are used. The first version is a flat-plate model of the aircraft, while the second version is a sandwich-panel model. The flat-plate model is used to calculate the spanwise lift distribution of the wing. The sandwich panel model is used to calculate the upper and lower surface pressure distributions. The dimensions of

both versions are identical. The flat-plate model is shown in Figure (6), while the sandwich panel model is shown in Figure (7).

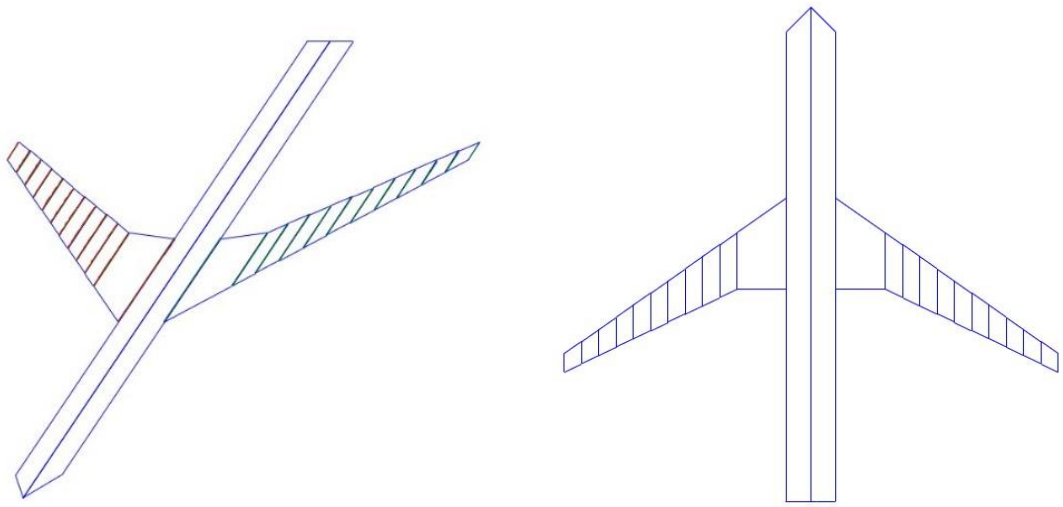

Figure 6. Flat-Plate Model in VORLAX

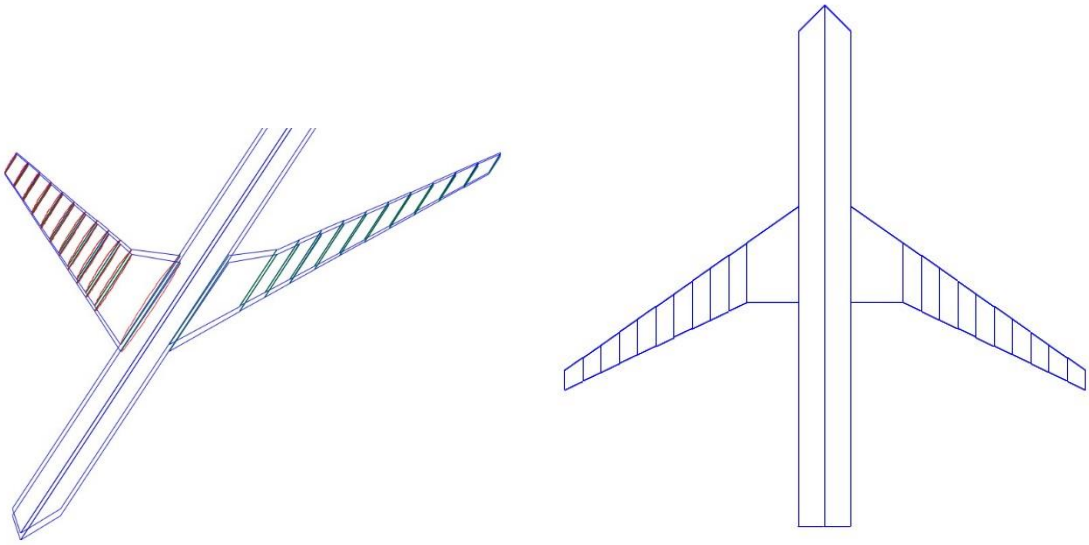

Figure 7. Sandwich Model in VORLAX

Figures (6) and (7) show that each wing is divided into eleven panels. The inboard panel includes a "Yehudi," common on most airliners. The remaining ten panels have an

equal span. The eleven panels give twelve control points at which the twist, camber, and thickness can be specified. VORLAX interpolates these values between the control points to ensure a smooth distribution.

When VORLAX runs a case with the flat-plate model, it simulates flow over both surfaces of the model. It then calculates the pressure difference between the two surfaces and returns that value. Therefore, there is a need for the sandwich panel model to be able to calculate the pressure distribution across the top and bottom surfaces rather than just the pressure differential. The sandwich panel model also offers slightly more accuracy in the pressure calculation, allowing for the implementation of the wing thickness. VORLAX recommends that the distance between the two surfaces is set to two-thirds of the thickness-to-chord length of the wing section [18]. When VORLAX runs a case with the sandwich panel model, only the flow on the two outside surfaces of each panel is simulated. The flow on the two inside surfaces is ignored, thus simulating wing thickness.

CHAPTER 4

ANALYZING BASIS EIGENFUNCTIONS

Generating Eigenfunctions

Donovan & Takahashi's work shows that the spanwise lift distribution can be decomposed into a set of twist perturbation response eigenfunctions [20].

$$\boldsymbol{D}f(twist) = \lambda f(twist) \tag{3}$$

Equation (3) shows the concept of an eigenfunction, where the eigenfunction f is a function of the wing twist that is being operated on by a linear operator $\boldsymbol{D}$. There exists an eigenvalue λ that when the eigenvalue multiplies the eigenfunction (an eigenfunction is an eigenvector), it scales the eigenfunction to the desired output. The eigenvalue acts as a tuning parameter for the eigenfunction. This decomposition of the lift into a set of eigenfunctions allows a wing designer to quickly optimize a twist distribution that generates an elliptical lift distribution.

To demonstrate how these eigenfunctions can be used to optimize the wing twist, a set of fourteen VORLAX simulations are run to generate the eigenfunctions for the model. The first simulation is run at an angle of attack (AoA) of two degrees and is used as the baseline. The AoA of two degrees was chosen because it is a reasonable value for the wing camber profile, which is discussed later. In general, any reasonable angle of attack can be used as the baseline. The baseline solution was run with zero twist across the span. The second simulation was run at an AoA of three degrees, with zero twist across the span. The difference between the first and second solutions gives the angle of

attack perturbation response eigenfunction. The remaining twelve simulations are run by varying the twist at each spanwise station. One at a time, the twist at each station is set to one degree. The difference between these solutions and the baseline solution gives the twist perturbation response eigenfunction for each spanwise station.

This eigenfunction analysis of the model aircraft was done at an altitude of 29,000 feet, a Mach number of 0.82, and a cruise weight of 500,000 lbm. These are the values chosen for the cruise design point for the model. The reasoning behind these values is discussed later.

Analyzing The Response Eigenfunctions

The non-optimized wing thickness and camber distributions used for this analysis are shown in Table (2).

Wingspan Control Point	Thickness to Chord Percentage	Camber Percentage
1	13.0%	-2.4%
2	12.5%	-1.2%
3	12.5%	0.0%
4	12.0%	1.2%
5	11.5%	2.4%
6	11.0%	2.4%
7	11.0%	2.4%
8	10.5%	3.0%
9	10.5%	3.0%
10	10.5%	3.6%
11	10.5%	3.6%
12	10.5%	3.6%

Table 2. Sample wing t/c and Camber Distribution.

In this table, control point one is at the side of body, with each succeeding point moving outwards along the span, with control point twelve at the wingtip. The resulting lift perturbation response of this wing is shown in Figure (8).

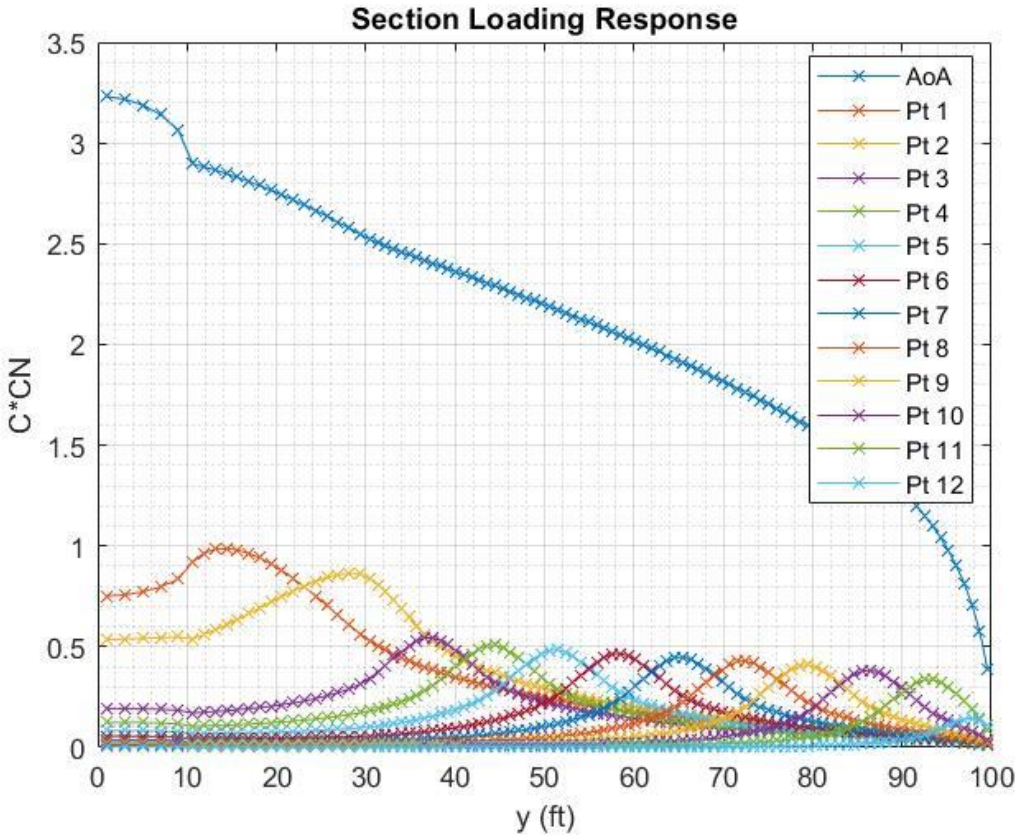

Figure 8. Example Lift Perturbation Response

From Figure (8), the angle of attack (AoA) has the most significant impact on the overall lift, which is to be expected. Since the Yehudi panel has a much larger area than the other panels, it has the most impact on the lift of any panel. This is seen from the perturbation response of control points one and two. As was found in the work of Donovan & Takahashi [20], the lift perturbation response of each control point spikes at the control

point's location, but it also affects the lift on the neighboring areas of the wing. There is a smearing of the lift effect of each control point across the wingspan.

The eigenfunctions shown in Figure (8) can be scaled to develop a desired spanwise lift distribution across the wing. Ignoring, for the moment, the chordwise pressure distribution, one can perform a constrained optimization of the lift response eigenvalues to develop an elliptical spanwise lift distribution. The eigenvalues that most closely develop an elliptical lift distribution were found using MATLAB's least-squares optimizer with an active-set algorithm [21]. These eigenvalues, the twist values of each spanwise control point, are shown in Figure (9), and the resulting lift distribution is shown in Figure (10).

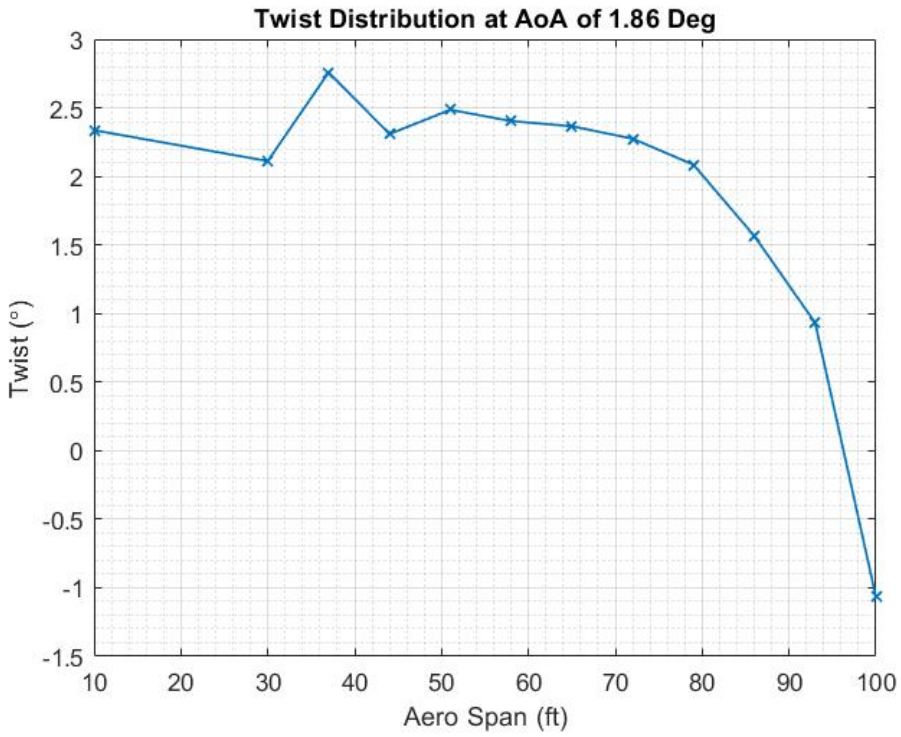

Figure 9. Optimized Lift Perturbation Eigenvalues

The optimized angle of attack is found to be at 1.86 degrees. This twist distribution has around 3.5 degrees of washout from side-of-body to wingtip. This is not surprising, as wing washout is generally required for elliptical loading.

There was an attempt to keep the twist distribution shown in Figure (9) to a realistic set of twist values that could be incorporated into the structure of an actual wing. This was done by constraining each control station such that it could not be more than ± 2 degrees from each immediately neighboring control point.

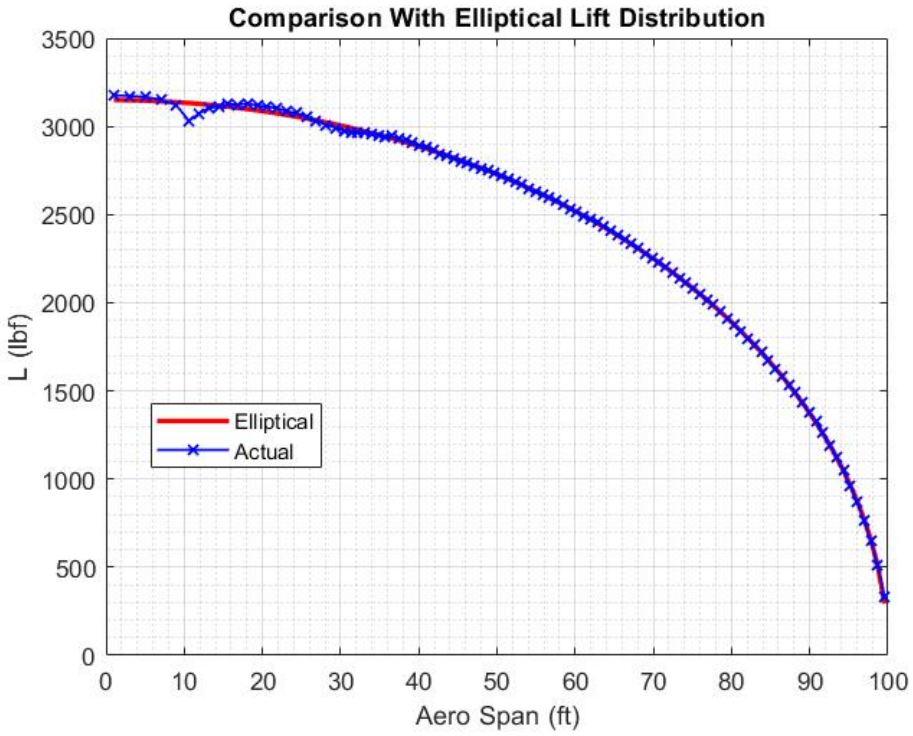

Figure 10. Twist Only Optimized Lift Distribution

This optimized twist distribution does indeed develop a mostly elliptical spanwise lift distribution. Some interference from the fuselage exists on the inboard portion of the

wing. Overall, this twist distribution does an excellent job of developing an elliptical lift distribution.

While this twist distribution works well at developing elliptical spanwise loading with the given wing thickness and camber, there was no attempt to optimize the twist concerning the upper and lower surface pressures. If this design generates substantial pressure drag from an ill-structured pressure distribution, the elliptical loading is of little importance.

A sandwich panel model with the same twist, camber, and thickness distributions is simulated. A large region of the wing, from approximately 50% to 90% of the semi-span, shows the presence of strong shockwaves.

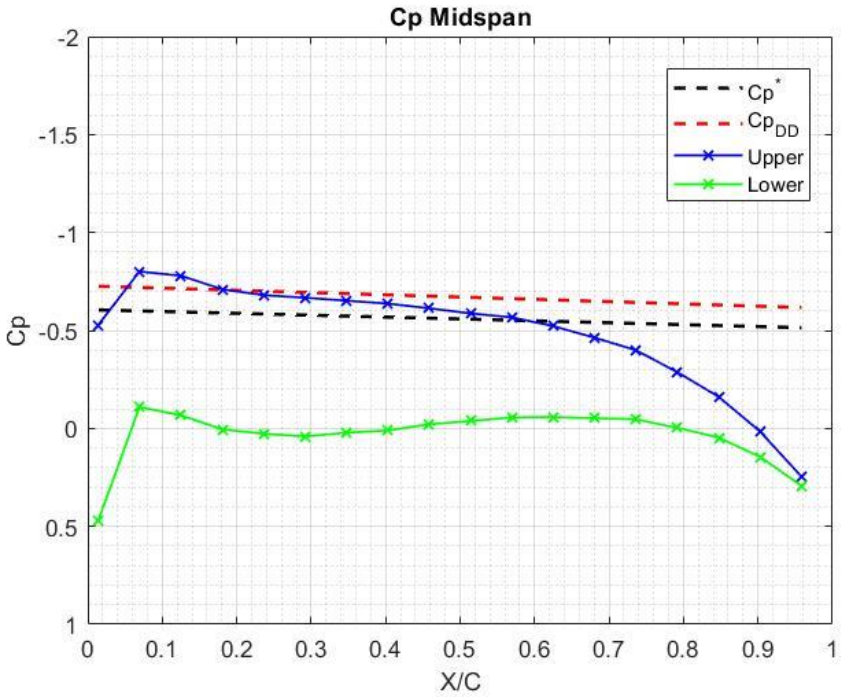

Figure 11. Midspan Cross-Sectional Pressure Distribution

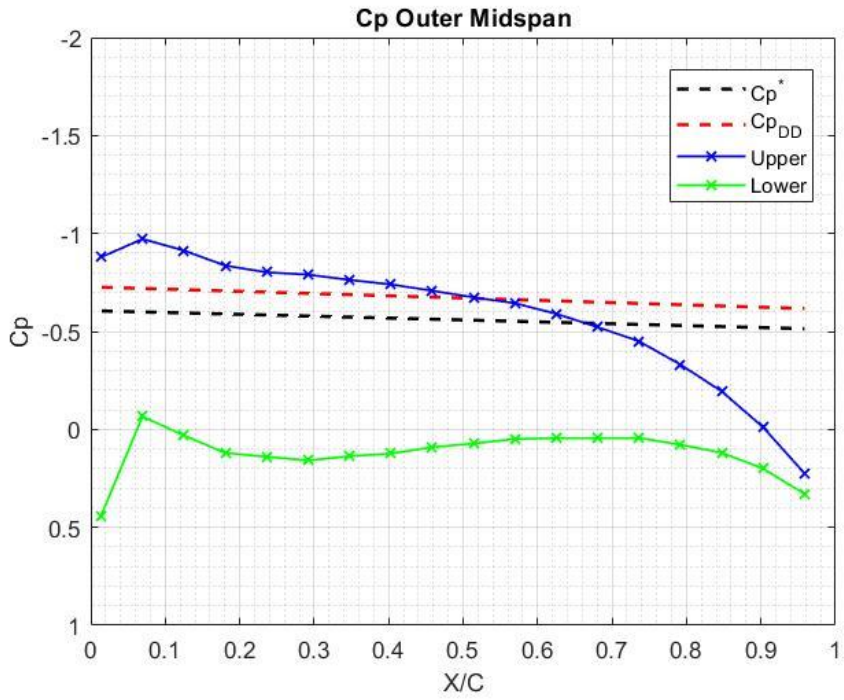

Figure 12. Outer Midspan Cross-Sectional Pressure Distribution

Figures (11) and (12) show cross-sectional pressure distributions at points on the wing that indicate the presence of strong shockwaves. The upper surface pressures exceeded the Küchemann predicted critical pressure, and the drag-divergence predicted pressure of 20% greater than the critical pressure. This indicates the presence of strong shockwaves and a significant amount of pressure drag. The critical flow regions of the wing are shown in Figure (13).

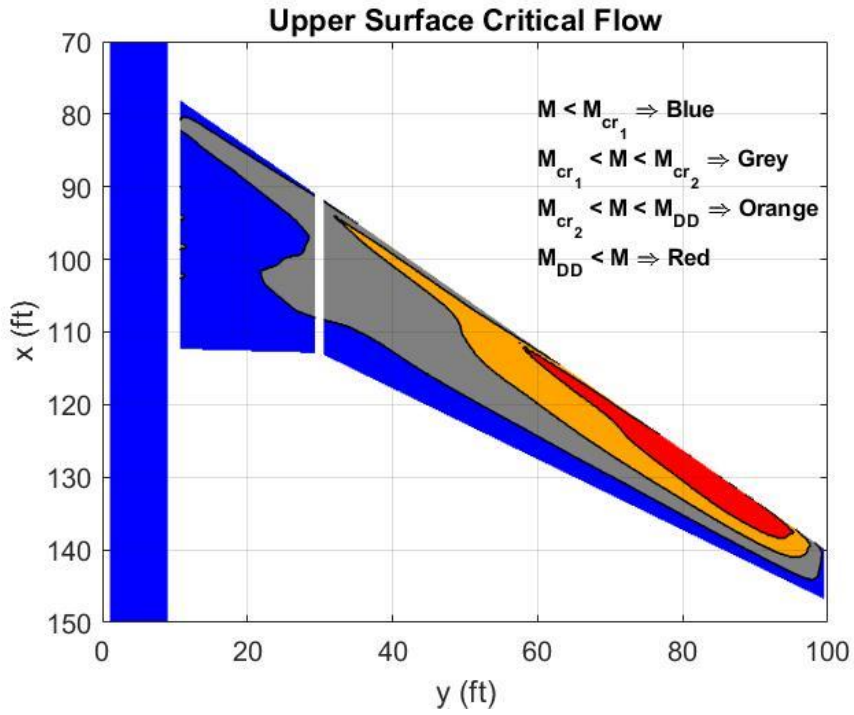

Figure 13. Upper Surface Critical Flow Regions

The regions in blue represent subcritical flow. The gray regions show pressure coefficients that would be critical at a zero-sweep angle (flow is passed the lower critical Mach number but below the upper critical Mach number). Orange regions show flow at or beyond the critical pressure coefficient, guaranteeing local supersonic flow, but the local C_p is below the drag divergence value. This indicates that the regions in orange have weak shockwaves. Finally, the red regions represent pressure coefficients that exceed the drag divergence value. A substantial portion of the wing has locally supersonic flow, and about half of that portion indicates strong shockwave formation and drag divergence.

As shown in Figure (13), strictly optimizing the twist of the wing to develop an elliptical spanwise lift distribution is not ideal. Any drag reduction gained by the elliptical loading is undoubtedly overshadowed by a large amount of drag incurred from the strong

shockwaves. An optimal transonic wing design must balance the desire to develop an elliptical spanwise loading and generate minimal pressure drag. There will also likely be more preference towards minimizing the pressure drag as it tends to be greater than the lift-induced drag.

CHAPTER 5

MODEL WING DESIGN

Defining Twist, Camber, and Thickness

As was shown in the previous chapter, the application of wing twist, camber, and thickness cannot be applied separately. Instead, each design feature must be looked at together, and a configuration developed that finds the proper balance between elliptical loading and wing surface pressures. An attempt was made to design an optimization tool to find this balance. However, this approach proved challenging to get solution convergence, and at the time, the sensitivity of the three design variables and their cross-coupling was not well understood or implemented in the tool. Since this work aims to look at the effects of static aeroelasticity and not transonic wing design, a manual approach was pursued to apply twist, camber, and thickness.

The NACA 0010-65 thickness profile was chosen as the base airfoil geometry [22]. The most significant difference between the standard NACA 0010 and the NACA 0010-65 airfoil is that the maximum thickness of 10% is shifted from the 30% chord point on the NACA 0010 to the 50% chord point on the NACA 0010-65. This was chosen to simplify the design process by reducing the leading-edge thickness. Furthermore, the NACA 0010-65 profile has less steep gradients from the minimum to maximum thickness locations, which helps to keep the upper surface velocities down. A comparison between these two airfoils is shown in Figure (14).

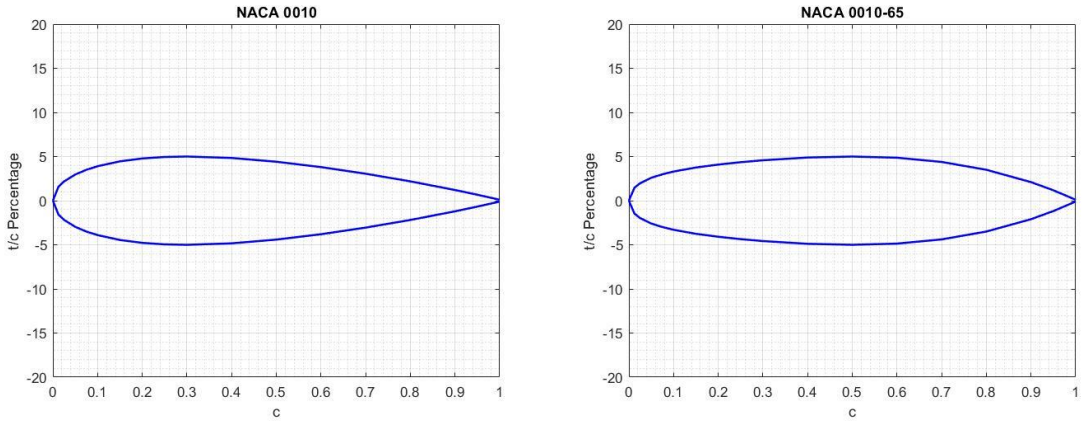

Figure 14. Comparison of Baseline Airfoil Geometry

An additional benefit to using the NACA 0010-65 as the baseline geometry is that it can be easily scaled for thickness. The geometry coordinates of the airfoil are normalized to one. Thus, to change the thickness to 12%, the y-coordinates need to be multiplied by 1.2.

In addition to the wing thickness, several camber profiles were examined. The NACA 62, 63, and 64 and the NACA 210, 220, 230, 240, and 250 mean camber lines were evaluated [22]. It was quickly determined that the NACA 64 camber line was the best for the given cruise lift coefficient (C_L) and angle of attack. The design C_L of the NACA 62 and 63 camber lines are much higher than the desired cruise C_L, thus generating excessive upper surface pressures, particularly near the leading edge. In contrast, the NACA 210 to 250 camber lines have design lift coefficients much smaller than the desired cruise C_L. This made it difficult to achieve the required lift. Furthermore, the angle of attack necessary to achieve the required lift was significantly higher than that of NACA 64. Thus, keeping in line with Obert's recommendation of keeping the angle of

attack as low as possible, the NACA 64 camber line was chosen [10]. The geometry of the NACA 64 camber line is shown in Figure (15).

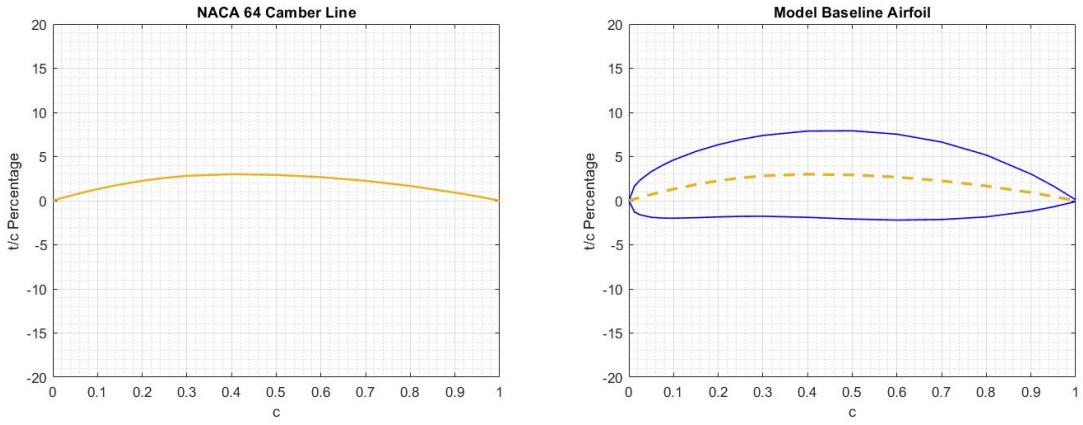

Figure 15. NACA 64 Camber Profile and Model Airfoil.[22] Camber line scaled to 50%.

Defining the twist, thickness, and camber distribution proved time-consuming. However, a manual approach was optimal with the given time and resources, and a design was settled upon. In potential future work, research into a useful optimization tool that can successfully balance the spanwise and chordwise loading should prove beneficial.

The twist, thickness, and camber distribution were found by manually iterating through a series of designs. After each iteration, the chordwise pressure distribution was analyzed at several spanwise stations along with the spanwise lift distribution. A MATLAB script was created that would update the VORLAX model, run the simulation, and extract and plot the results. The eventual design distributions were found using this script and are shown in Table (3). The design flight conditions are shown in Table (4).

Control Point/Semi-Span Location	Twist	t/c Percentage	Camber Percentage w.r.t. the chord length
1 (10 ft)	2.8°	13.0%	-1.8%
2 (30 ft)	2.15°	12.5%	-0.6%
3 (37 ft)	0.0°	12.5%	1.2%
4 (44 ft)	-0.4°	12.0%	1.5%
5 (51 ft)	-1.0°	11.5%	1.8%
6 (58 ft)	-0.75°	11.0%	1.8%
7 (65 ft)	-1.05°	11.0%	2.1%
8 (72 ft)	-1.4°	10.5%	2.4%
9 (79 ft)	-2.3°	10.5%	2.7%
10 (86 ft)	-2.6°	10.5%	2.7%
11 (93 ft)	-3.8°	10.5%	2.7%
12 (100 ft)	-5.0°	10.5%	2.7%

Table 3. Model Wing Twist, Thickness, and Camber distribution.

Maximum Takeoff Weight	550,000 lbm.
Design Flight Weight	500,000 lbm.
Design Flight Mach Number (Lower Critical Mach Number)	0.77
Analysis and Drag Divergence Mach Number (Upper Critical Mach Number)	0.82
Design Altitude at Design Flight Weight	29,000 ft.
Design C_L	0.436
Cp* (Upper Critical Mach Number)	-0.606
Cp* (Lower Critical Mach Number)	-0.379
Drag Divergence Cp at L.E. Sweep	-0.73
Drag Divergence Cp at Zero Sweep	-0.45

Table 4. Design Flight Conditions.

The design twist and thickness distributions are shown in Figures (16) and (17).

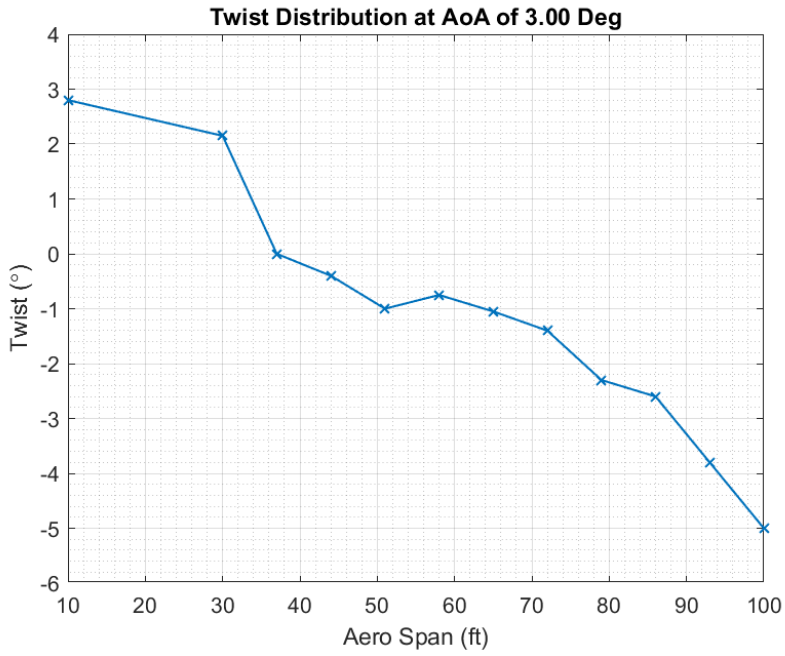

Figure 16. Design Wing Twist Distribution.

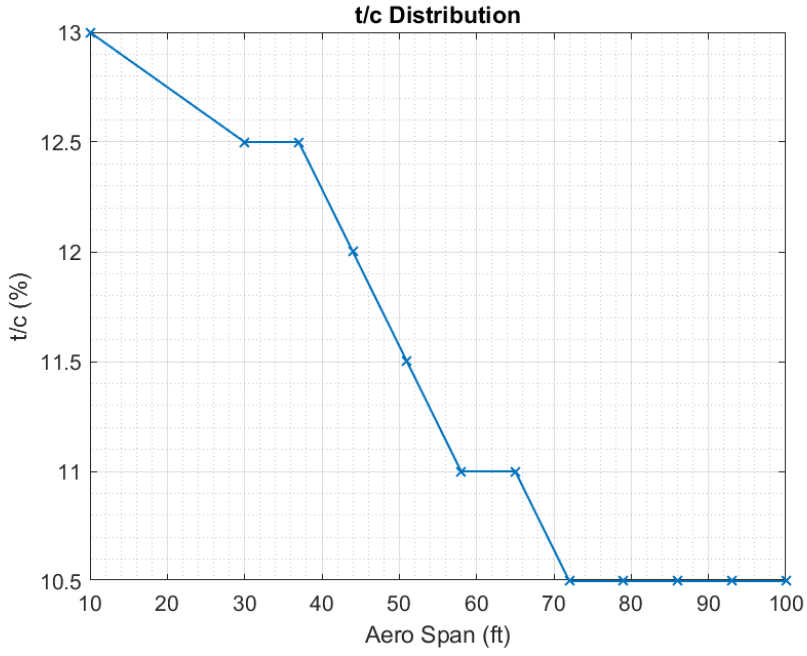

Figure 17. Design Wing Thickness Distribution.

A design angle of attack of three degrees was found to work well for the given design and flight conditions. Figure (16) shows that the wing has eight degrees of washout from the side of body to the wingtip. This large amount of washout is a byproduct of the high aspect ratio and long wingspan. It could prove significant when the wing is subjected to substantial bending deformations. The wing's chordwise profile at several control points is shown in Figures (18-20).

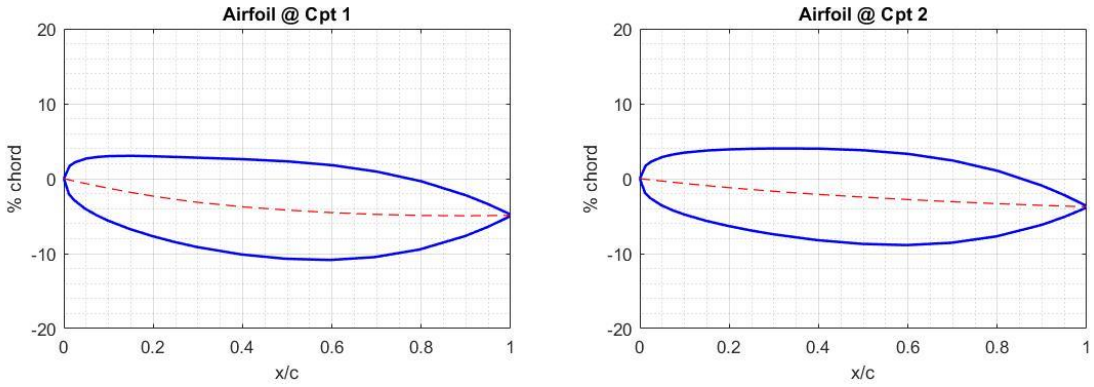

Figures 18. Chordwise Profile of Control Points 1 and 2.

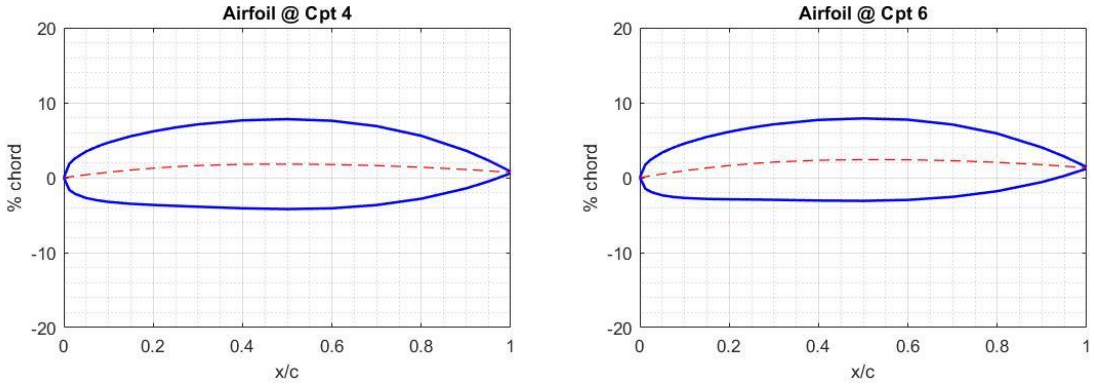

Figures 19. Chordwise Profile of Control Points 4 and 6.

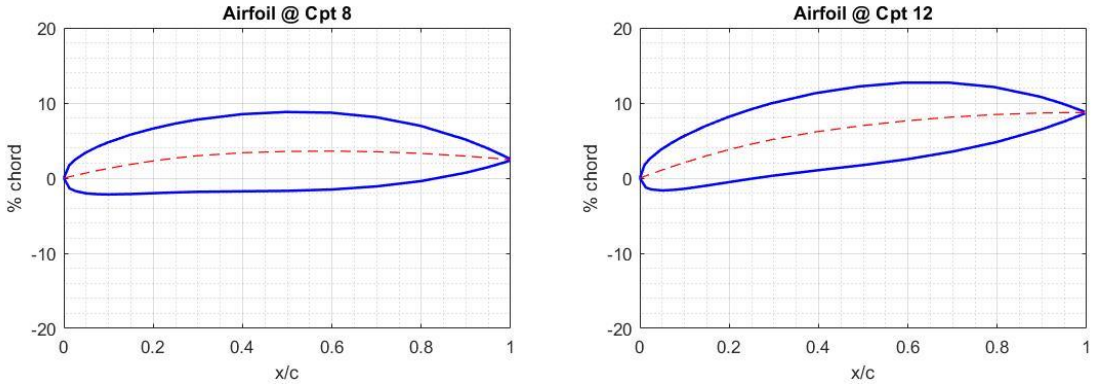

Figure 20. Chordwise Profile of Control Points 8 and 12.

Figures (18 – 20) include the airfoils rotated at their respective twist values. These figures further demonstrate the washout from the side of body to the wingtip. Furthermore, as suggested by Obert, the airfoils at control points one and two have negative camber and positive twist. This was done to help align the pressure isobars with the wing's leading edge.

The spanwise loading of the design configuration is shown in Figure (21). As expected, the loading is not perfectly elliptical. There is interference from the fuselage that distorts the wing loading on the inboard portion of the wing. Nevertheless, the wing still achieves a spanwise elliptical loading distribution over nearly 90% of the wingspan. Figures (22) and (23) show the upper surface pressure distribution and critical flow conditions, respectively. The design configuration is not shock free. However, it appears to have a weak shock as it only exceeds the critical pressure coefficient but remains below the expected drag-divergence critical pressure. The maximum upper surface pressure coefficient is shown in Table (5).

Analysis Mach Number	Maximum Cp	Critical Cp	Drag Divergence Cp
0.82	-0.709	-0.61	-0.732

Table 5. Comparison of Measured Cp

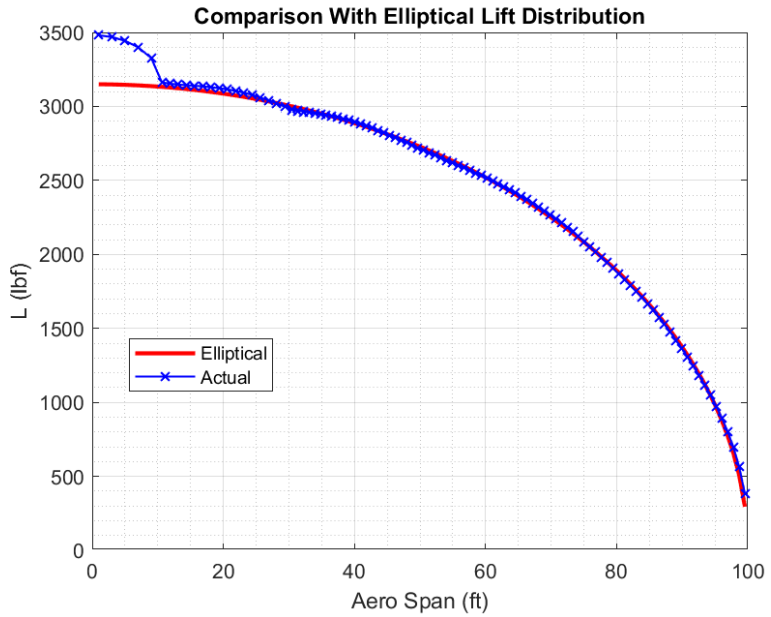

Figure 21. Spanwise Lift Distribution of Wing.

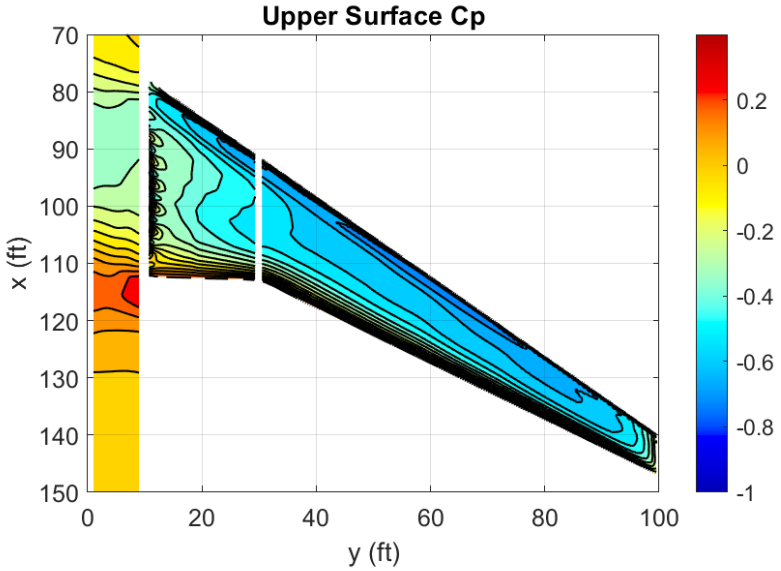

Figure 22. Upper Surface Pressure Distribution of Wing

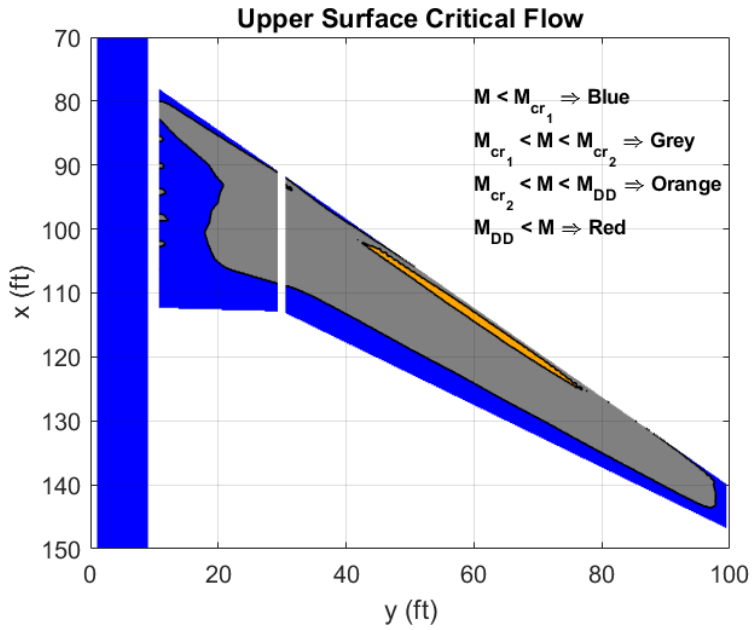

Figure 23. Upper Surface Critical Flow Conditions.

The process of designing this wing followed an inverse approach. In other words, the desired cruise shape was identified. From this desired cruise shape, the aeroelasticity of each wing was accounted for by subtracting the aeroelastic response from the desired shape. This gave the required jig shape that, when the aeroelastic response was added, the desired wing shape would be the outcome. As the main emphasis here was the aerodynamics and the effect of the aeroelasticity on the aerodynamics, this approach was chosen over taking a more straightforward, albeit potentially more complicated approach. This alternative approach would be to design the wing to optimize its structural characteristics. The resulting aerodynamics of this approach would then be tailored to optimize its efficiency by using active aeroelastic tailoring via wing control surfaces. This is similar to the design approach of the Boeing 787. In reality, a compromise

between the two would likely be found. For this work, the aerodynamics are the focus; thus, the first approach was followed.

CHAPTER 6

AEROELASTIC MODEL

Defining The Research Space

This work aims to understand the effects of static elastic deformation of the wing on aerodynamic performance. The wing model was analyzed using different material strengths to study these effects. The primary motivation behind using composite materials, particularly carbon fiber, is their high tensile strength-to-weight ratio. This allows aircraft manufacturers to save weight by using lighter materials and having to use less of these materials. Thus, materials with four different tensile yield strengths were analyzed. These tensile yield strengths are 46-ksi, 69-ksi, 105-ksi, and 180-ksi. The first two values represent traditional aerospace aluminum alloys, such as 6061 aluminum [23]. The last two values represent the tensile yield strength that one would expect from a high-strength carbon-fiber composite laminate [24].

Simplicity for the sake of computational cost drove the decision to model the half-wing as a 1-D beam-element model [7]. This decision neglects 2-D and 3-D structural effects, but this work aimed to look at wing bending. A one-dimensional model where the integrated load of each wing section acts on the elements of the 1-D model should account for the up and down bending of the wing.

The 1-D beam-element structural model comprises 101 nodes from root to tip. The structural model is aligned with the leading edge sweep of the wing. This reference frame is referred to as the aero-reference frame and is demonstrated in Figure (24).

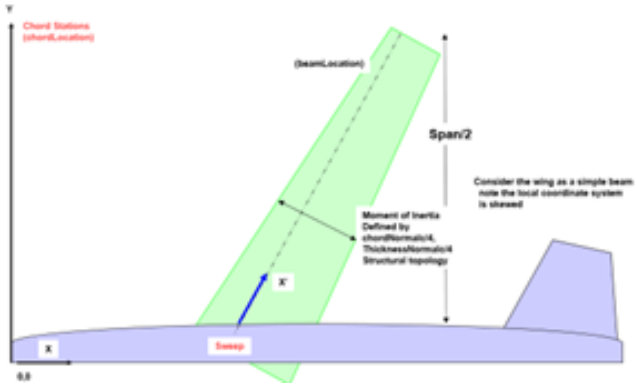

Figure 24. Aero-Reference Frame.

Each node on the structural model is subject to an aerodynamic and inertial load. The inertial load includes the structural weight of the wing, the weight of the fuel, and the engine weight. The inertial loads were determined using an empirically driven weight estimation tool developed by Professor Takahashi and used in our undergraduate senior design. This tool is based on empirical models developed by Torenbeek and as found in Niu's structural design book [7]. The weight estimation tool accepts a multitude of inputs ranging from the design Mach number, material strength, wing and tail sizes, and propulsion data. Using this data in the empirical models presented in Niu, the tool provides a detailed breakdown of the loaded and unloaded weight of the aircraft [25]. The inputs were identical except for the material strength for each of the four models analyzed. Using the key model dimensions in Table (1), the flight conditions in Table (4), and some general propulsion data, the key inertial weights of each model are calculated and shown in Table (6).

Model Material Strength	Ft_y = 46-ksi	Ft_y = 69-ksi	Ft_y = 105-ksi	Ft_y = 180-ksi
Design Cruise Weight	500,000 lbm.			
Aerodynamic Load	250,000 lbf.			
Wing Structural Weight	40,000 lbm.	37,500 lbm.	35,000 lbm.	32,500 lbm.
Fuel Weight	85,000 lbm.	87,500 lbm.	90,000 lbm.	92,500 lbm.
Engine Weight	19,000 lbm.			

Table 6. Key Aircraft/Wing Inertial Loads.

A few crucial assumptions were made in the development of these inertial loads. First, as can be seen in Table (6), the design cruise weight remains constant across all four models. With higher-strength materials, the structural weight of the wing and the aircraft decrease. This will either lead to a reduced cruise weight or an increase in the payload capacity. Here, the latter was chosen, and used the increased payload as additional fuel. This choice was made so there was no need to have four sets of twist, camber, and thickness distributions, one set for each model. If the design cruise weight were allowed to decrease, a new "optimal" distribution set would technically be needed. Keeping the design cruise weight the same means that the design cruise Mach number and altitude remain the same, and therefore our "optimal" wing twist, camber, and thickness distributions remain the same.

The second important assumption regarding the inertial loads is that the wings and fuselage of the aircraft develop all the required lift. In reality, the horizontal tail may provide some lift, but the wing develops the majority. The wing and fuselage are assumed

to provide all the lift to keep the model simple. The third important assumption is that all the fuel is carried in the wings. This is not an entirely incorrect assumption, as most aircraft have a "wet" wing, meaning that the wing stores fuel. Some aircraft have additional fuel stores in the fuselage of the aircraft. However, for ease of bookkeeping the fuel weight, it is assumed that all the fuel is stored in the wings. The inertial loads of the 46-ksi model are shown in Figure (25).

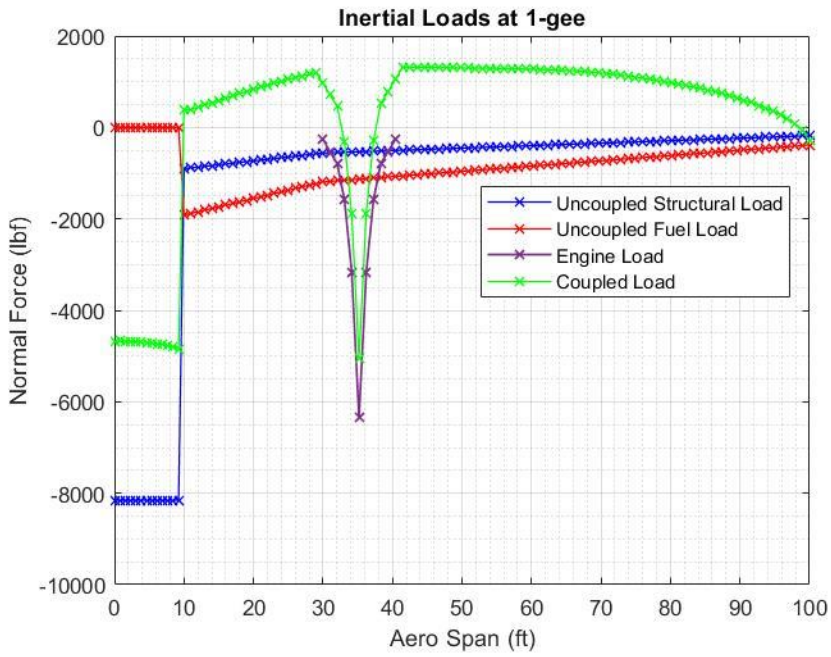

Figure 25. Inertial Loads of the 46-ksi Model.

Using the bilateral symmetry of the aircraft, only one of the wings and half of the fuselage are used in the structural model. The inertial loads in Table (6) are loads for just one wing. From Figure (25), the structural weight of the wing and fuel weight are distributed across the 101 nodes that make up the wing. These loads are distributed as a function of the wing chord length at each node. One also sees a structural load applied to

the fuselage. This load is half the design cruise weight minus the structural, fuel, and engine weight. Finally, the engine weight is distributed across eleven nodes at about one-third of the semi-span. The eleven nodes were found to provide the best balance of capturing the effect of the engine weight and keeping the model simple.

Defining Wing Structure

The structural properties of each model are designed around a series of different expected loading cases. These cases include cruise flight loads at the design cruise weight, MTOW, and certified load factors in both positive (nZ_{max}) and negative (nZ_{min}) gee forces. The nZ_{max} and nZ_{min} load factors are based on FAA certification criteria outlined in 14 CFR § 25.337 [26]. The relevant positive and negative load factors outlined in the CFR for this aircraft are +2.5 gees and -1.0 gees, respectively.

For each material strength, a factor of safety (*FOS*) of 1.5 is prescribed in 14 CFR § 25.303 [27]. This factor of safety can be accounted for by derating the material strength by the required *FOS*. Thus, our four material strengths become,

Defined Tensile Strength, F_{ty}	**Derated Tensile Strength, *FOS* = 1.5**
46-ksi	30.667-ksi
69-ksi	46-ksi
105-ksi	70-ksi
180-ksi	120-ksi

Table 7. Derated Tensile Strengths of Each Model

A fundamental assumption made with the structural model is that it is comprised of a single material type. Furthermore, the assumption of isotropic materials is made so that there are uniform material properties throughout the wing. While this is not true in

reality, particularly in composite materials [4], it is a necessary assumption to keep from having to use a 2-D or 3-D finite-element model.

Assuming uniform and isotropic material properties throughout the wing structure, the elastic modulus, *E*, is assumed to be constant. Therefore, the structural rigidity, *EI*, is determined by the area moment of inertia of the wing. The analysis of the wing bending is now decoupled from the modulus of elasticity. The differences between the four models are the area moment of inertia and the applied inertial loads.

A wing's torque box can be considered its structural skeleton. In its most general form, the torque box consists of three major components. These components are the ribs, spars, and covers. The ribs are chordwise components spaced out along the wingspan. They typically incorporate the airfoil shape at a given section and can be used to divide the torque box into multiple sections across the span. The spars and covers are represented in Figure (26).

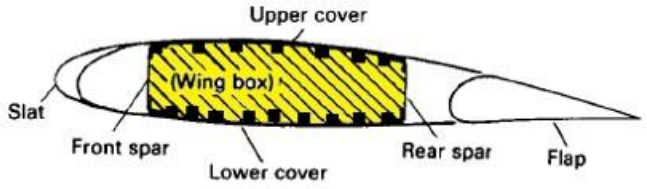

Figure 26. Sketch of Wing Torque Box Structure. [7]

In the spanwise direction, the front and rear spars bookend the torque box while the upper and lower covers closeout the rectangular-like structure. Figure (27) shows the resolution of the wing bending moment into forces along the upper and lower wing surfaces.

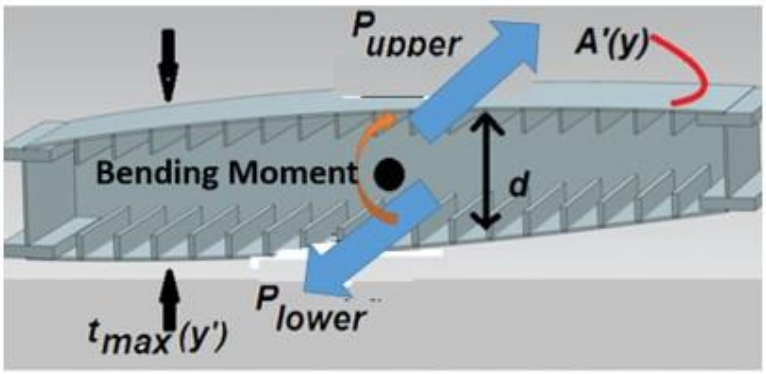

Figure 27. Resolving of the Wing Bending Moment into Forces. [7]

The front and rear spars are the two I-beam structures in Figure (27). The upper and lower skin has a thickness *t(y)*. Often there are stiffeners along the upper and lower surfaces. The spar caps (the horizontal portions of the I-beam), the upper and lower wing covers, and the stiffeners must resist the transverse bending of the wing. Since the transverse wing bending moment is of interest, the wing torque box can be modeled as a hollow rectangle.

The transverse bending moment, *M(y)*, can be defined using a force couple that consists of equal and opposite forces, *P(y)*, that act at a distance, *d(y)*, from the center of the wing torque box. This resolving of the transverse bending moment into a force couple is shown in Equation (4).

$$\boldsymbol{M}(y) = \boldsymbol{P}(y)\, \boldsymbol{d}(y) \tag{4}$$

A NACA 4-digit airfoil form has the front and rear spars at the 15% and 65% chord locations, respectively. Over the area between the two spars, there is an average distance between the upper and lower wing covers of approximately 70% of the maximum wing

thickness at a given location. Thus, Equation (4) can be solved for the force, *P(y)*, and expressed as a function of the wing thickness.

$$\boldsymbol{P}(y) = \frac{\boldsymbol{M}(y)}{\boldsymbol{d}(y)} \longrightarrow \boldsymbol{P}(y) = \frac{\boldsymbol{M}(y)}{0.7\ \boldsymbol{t}(y)} \tag{5}$$

The positive and negative force couple is dropped by realizing that under positive *nZ* loading cases, the wing's upper surface is under compression and the lower surface under tension. Conversely, in negative *nZ* cases, the opposite is true. Regardless, the magnitude of the force is the same. For a given material strength, the tensile strength limited cross-sectional area of the upper and lower wing covers is proportional to the magnitude of the applied force.

$$\boldsymbol{A}(y) \geq \frac{\boldsymbol{P}(y)}{\boldsymbol{F}_{ty}} \tag{6}$$

Where F_{ty} is the derated material tensile strength from Table (7).

Recall Equation (1), which showed the area moment of inertia. It is the area moment of inertia of the wing torque box that plays a critical role in the resistance to transverse bending. Equation (1) can be reexpressed as a function of the wingspan using the geometric properties of the wing. This is shown in Equation (7).

$$\boldsymbol{I}(y) = \frac{0.5\ \boldsymbol{c}(y)\left(0.7\ \frac{\boldsymbol{t}}{\boldsymbol{c}}(y)\boldsymbol{c}(y)\right)^3 - \left[\left(0.5\ \boldsymbol{c}(y) - 2\ \boldsymbol{t}(y)\right)\left(0.7\ \frac{\boldsymbol{t}}{\boldsymbol{c}}(y)\boldsymbol{c}(y) - 2\ \boldsymbol{t}(y)\right)^3\right]}{12} \tag{7}$$

Where ***c(y)*** is the spanwise chord length, $\frac{\boldsymbol{t}}{\boldsymbol{c}}$ (y) is the spanwise wing thickness to chord ratio, and ***t(y)*** is the upper and lower wing cover thickness. The upper and lower wing cover thickness can be defined as,

$$\boldsymbol{t}(y) = \frac{\boldsymbol{A}(y)}{0.5\,\boldsymbol{c}(y)} \tag{8}$$

The distance between the front and rear spar on NACA 4-digit style airfoil is approximately 50% of the chord length, which is why there is a factor of ½ in Equation (8).

Using Equations (6) and (7), the area moment of inertia as a function of both span location and derated material strength is defined. Since the elastic modulus is assumed to be constant between the four material strengths, the structural rigidity, *EI*, is driven by the area moment of inertia, which is a function of material strength.

Euler-Bernoulli Beam Equation

In addition to analyzing the effects of static aeroelasticity on aircraft performance, the limit to which one can assume linear aeroelasticity was studied. Thus, assuming linear aeroelasticity, the 1-D beam-element model of the wing can be analyzed using the classical 4th-order Euler-Bernoulli beam equation shown in Equation (9).

$$\frac{d^4 w(y)}{dy^4} = -\frac{P(y)}{E\,I(y)} \tag{9}$$

Where *w(y)* is the bending displacement, *P(y)* is the total applied load, *E* is Young's Modulus (assumed to be constant), and *I(y)* is the area-moment-of-inertia. Recall that the beam-element model of the wing, along with aerodynamic and inertial loads, are calculated in the aero-reference frame shown in Figure (24). In the aero-reference frame, the spanwise stations along the wing vary in both x and y. To solve the Euler-Bernoulli equation in the aero-reference frame, Equation (9) would have to be reexpressed as a function of both *x* and *y*. A coordinate transformation is performed to avoid this and

simplify the integration process. This new reference frame is referred to as the structural reference frame and is parallel to the leading-edge of the wing. Thus, the spanwise variations in *w*, *P*, and *I* are only a function of one dimension. The coordinate transformation is performed on the grid points and the applied loads and is shown in Equations (10) and (11).

$$y_{struc} = \frac{y_{aero}}{\cos \Lambda_{LE}} \tag{10}$$

$$P_{struc} = P_{aero} * \cos \Lambda_{LE} \tag{11}$$

This coordinate transformation simplifies the solution by allowing the wing to be treated as if it is subjected to pure bending.

A series of four consecutive integrations are performed to solve Equation (9). The result of each integration is shown in Equations (12 – 15).

$$\frac{d^3w(y)}{dy^3} = -\frac{V(y)}{E\,I(y)} \tag{12}$$

$$\frac{d^2w(y)}{dy^2} = -\frac{M(y)}{E\,I(y)} \tag{13}$$

$$\frac{dw(y)}{dy} = \theta \tag{14}$$

$$w(y) \tag{15}$$

Where *V(y)* is the shear force, *M(y)* is the bending moment, and θ is the slope of the wing deflection. *E* and *I*(y) are only introduced into the integral during the third integration to ensure proper bookkeeping. The aeroelastic twist and dihedral are found by projecting the slope of the wing deflection, θ, back into the aero-reference frame. The projection of θ is performed using Equations (16) and (17).

$$\Phi(y) = \tan^{-1}(\theta) * \cos \Lambda_{LE} \quad (16)$$

$$\Psi(y) = -\tan^{-1}(\theta) * \sin \Lambda_{LE} \quad (17)$$

Φ(y) is the aeroelastic dihedral, and *Ψ(y)* is the aeroelastic twist. An example of the solution process for the 46-ksi model is shown in Figures (28 – 31).

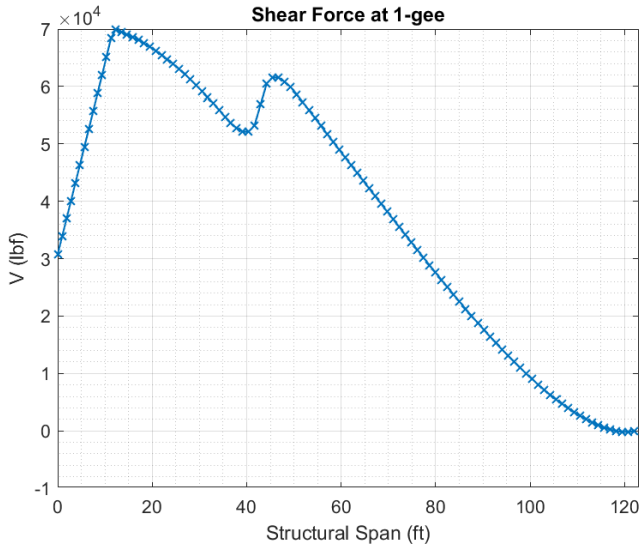

Figure 28. Wing Shear Force at 1-gee for 46-ksi Wing.

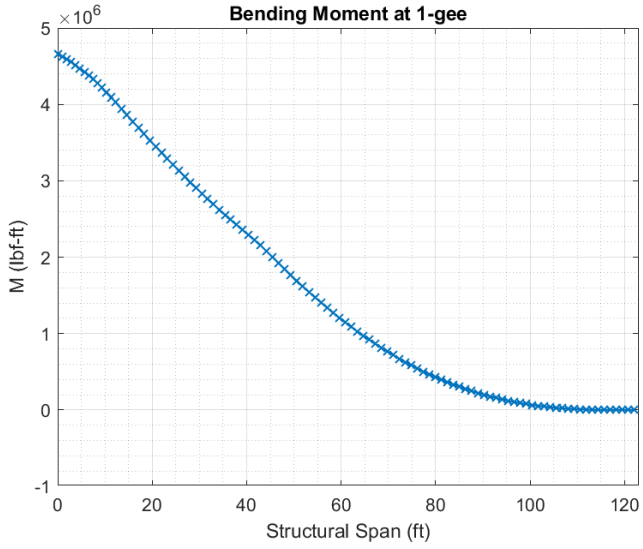

Figure 29. Wing Bending Moment at 1-gee for 46-ksi Wing.

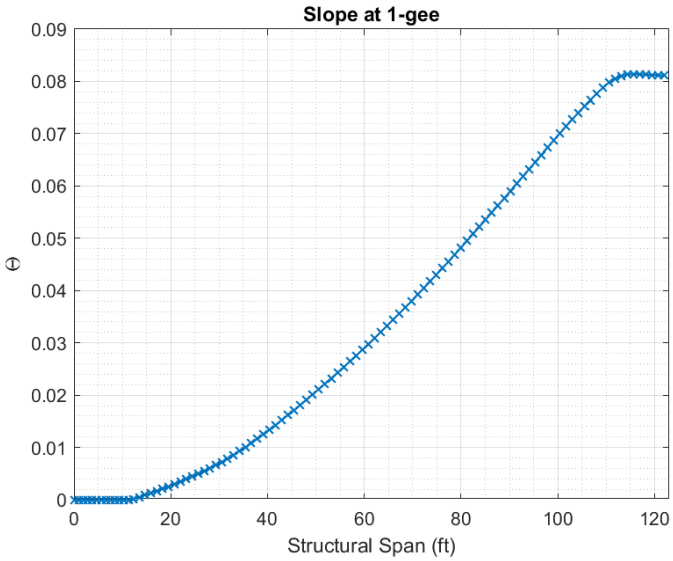

Figure 30. Wing Deflection Slope at 1-gee for 46-ksi Wing.

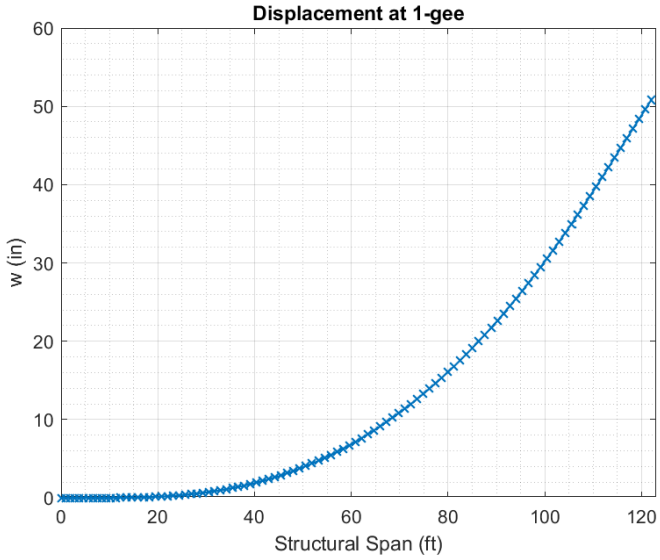

Figure 31. Wing Deflection at 1-gee for 46-ksi Wing.

The resulting aeroelastic twist and dihedral from this solution are shown in Figures (32) and (33), respectively.

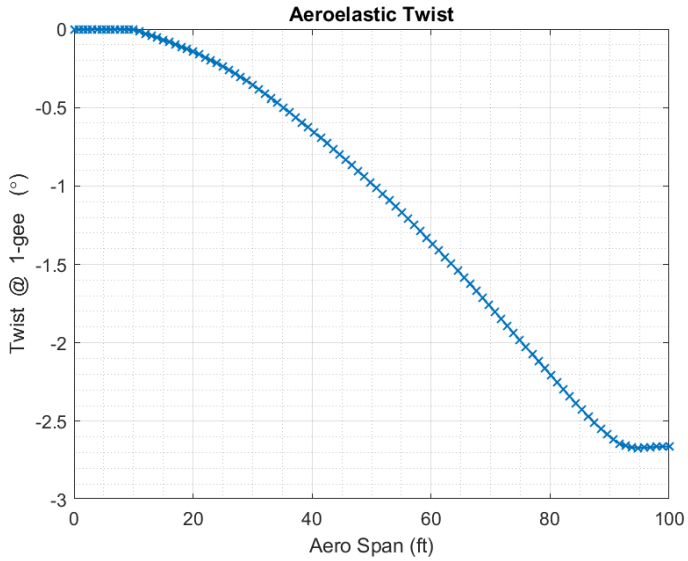

Figure 32. Aeroelastic Twist at 1-gee for 46-ksi Wing.

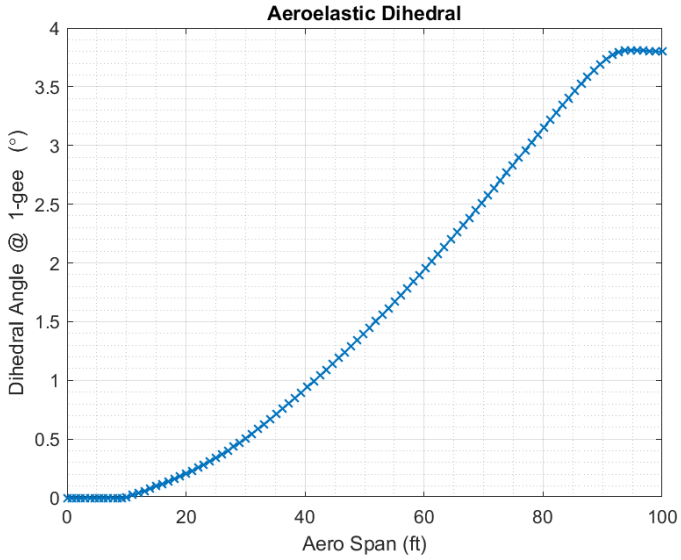

Figure 33. Aeroelastic Dihedral at 1-gee for 46-ksi Wing.

Aeroelastic Solver

With the aerodynamic and structural models defined, it is time to create a solver that iteratively solves the Euler-Bernoulli beam equation. This solver is created in MATLAB and accepts the aerodynamic load calculated using VORLAX. Solving the

aeroelastic bending of the wing is separated into two processes. The first process involves solving for the 1-gee aeroelasticity, as demonstrated in Figures (28 – 33). The purpose of solving for the 1-gee aeroelasticity is to determine the required jig twist that provides the design twist, camber, and dihedral at the design cruise condition. The second process solves the effects of nZ_{max}, nZ_{min}, and constant C_L fuel burn on the aeroelasticity.

Both processes implement a similar iterative-based solution algorithm with a few key differences. Both processes use varying relaxation factors to help with the solution convergence. It was found that the more rigid wing models, comprised of the 46-ksi and 69-ksi material, had quicker solution convergence than the less rigid models with the 105-ksi and 180-ksi material. Nevertheless, all four wing models required an evolving under-relaxation factor to varying degrees.

The iterative algorithm for both processes consists of the following steps. First, the input files for VORLAX are written, and then VORLAX is called to calculate the aerodynamic load. Next, the aerodynamic load is coupled to the inertial load, and then the coupled load is transformed from the aero-reference frame to the structural reference frame. Next, the series of four integrations are carried out to solve the Euler-Bernoulli beam equation. The bending slope and displacement are calculated from the third and fourth integrations. The bending slope, θ, is then projected back into the aero-reference frame using Equations (16) and (17). As previously discussed, these projections of θ are the aeroelastic increment of the wing twist and dihedral. The wing twist and dihedral are updated in the VORLAX input, and the next iteration begins.

The wing twist and dihedral are updated using a weighted average of the aeroelastic increments added to the jig values with the current wing twist and dihedral values. The weight used in the averaging process is dependent on the relaxation factor. If no relaxation factor is used, then a simple 1:1 average is used. When there is an over-relaxation factor, the average is weighted in favor of the new iteration values. If there is an under-relaxation factor, the average is weighted in favor of the previous iteration. As previously stated, all the models used some amount of under-relaxation.

Solving for the 1-gee aeroelasticity determines each model's required wing jig shape. Thus, the aerodynamic and inertial loads are held constant. Because the aerodynamic and inertial loads are constant, the solution is found in one set of iterations. The solver iterates until the changes in the wing twist, dihedral, and deflection drop below the predetermined stopping criteria. The stopping criteria are compared against the norm (2-norm) of the changes in twist, dihedral, and deflection.

The second process can be divided into two separate cases. The first case involves solving for the aeroelastic effects of either nZ_{max} or nZ_{min}. The second case solves the aeroelastic effects of a constant C_L fuel burn. The solution processes for both cases are shown in Figure (35). In both cases, the norm of the aeroelastic increments in twist, dihedral, and deflection are used as stopping criteria between each set of iterations. It was found that the sum of the residual changes in these variables of 0.001 provided a good balance of achieving solution convergence and maintaining a good amount of accuracy.

The first case uses multiple sets of iterations where the angle of attack can vary between each iteration. The first set of iterations begins with a load factor of 1-gee. Once

the set of iterations converges, the load factor is updated by ±0.01-gees, and the next set of iterations begins. This process continues until nZ_{max} or nZ_{min} is reached.

The number of iterations required to reach the desired load factors varied significantly between the different models. The more rigid 46-ksi and 69-ksi wings averaged around 10 iterations per step when moving from 1-gee to nZ_{max} and around 15 iterations from 1-gee to nZ_{min}. The 105-ksi wing averaged slightly more iterations at around 15 and 20, respectively. The most significant difference is found with the 180-ksi wing. When moving from 1-gee to nZ_{max} this wing averaged around 30 iterations per step and around 35 iterations per step when moving from 1-gee to nZ_{min}. Part of the cause for this large discrepancy between the models can be attributed to possible numerical instability/convergence issues with the aeroelastic solver. With that said, the significant flexibility of the 180-ksi wing certainly played a role in the required number of iterations. The solver had difficulty getting the solution to converge, even with heavy under-relaxation.

The constant C_L fuel burn simulation is also separated into multiple sets of iterations. The first set is at 100% fuel load. In these simulations, the angle of attack varies between each iteration, while the dynamic pressure, via increased altitude, can change between sets of iterations. Once a set of iterations converges, the fuel load is reduced by 10%. The reduction of the fuel-load changes both the inertial load and the required aerodynamic load since the weight of the aircraft decreases. The altitude is increased in factors of 500 ft to hold C_L constant. The reduction in fuel load alters the inertial load beginning at the wingtip and working to the root. Thus, the initial 10% fuel

reduction begins at the wing tip node and removes the fuel load at each subsequent node until 10% of the initial fuel load is removed. With each additional fuel reduction, the fuel load is removed, beginning at the outermost node with a non-zero fuel load, and the process repeats. Once the inertial load is updated and the altitude is adjusted, the next set of iterations begins. This process continues until 1-gee loading with zero fuel is reached.

The choice to use a gravity-fed fuel model in the wing was made early in the process. In retrospect, a more uniform approach to fuel unloading would have been more realistic and possibly led to changes in the results.

The main reason for going with the gravity-fed model is that it eliminates the possibility of implementing some optimized fuel unloading strategy. This not only would have been a more complicated approach, but it also would have introduced more variables into the results. All four wing models follow the same fuel unloading with the gravity-fed approach.

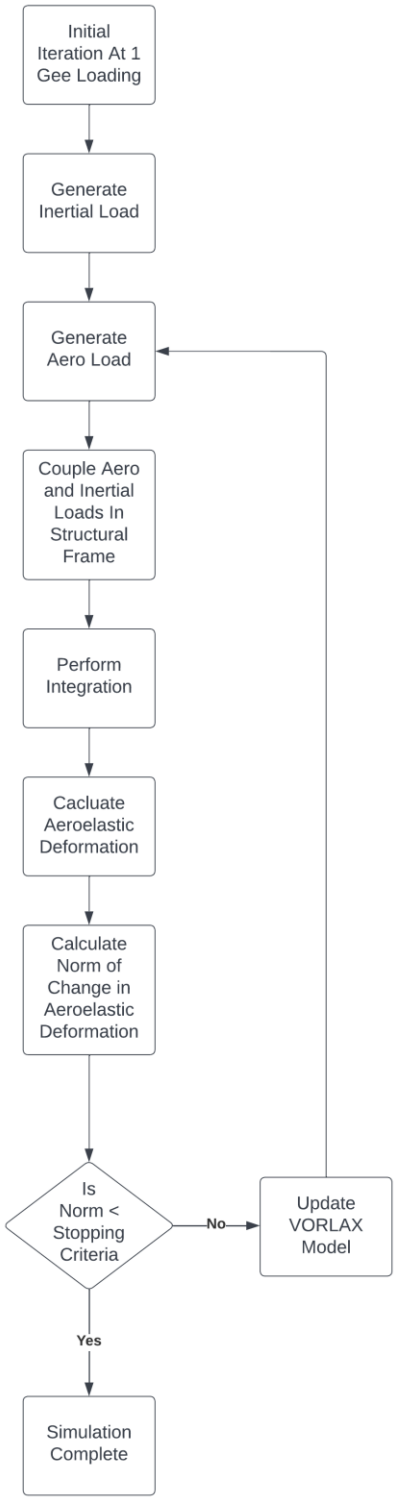

Figure 34. 1-gee Aeroelasticity Solution Procedure.

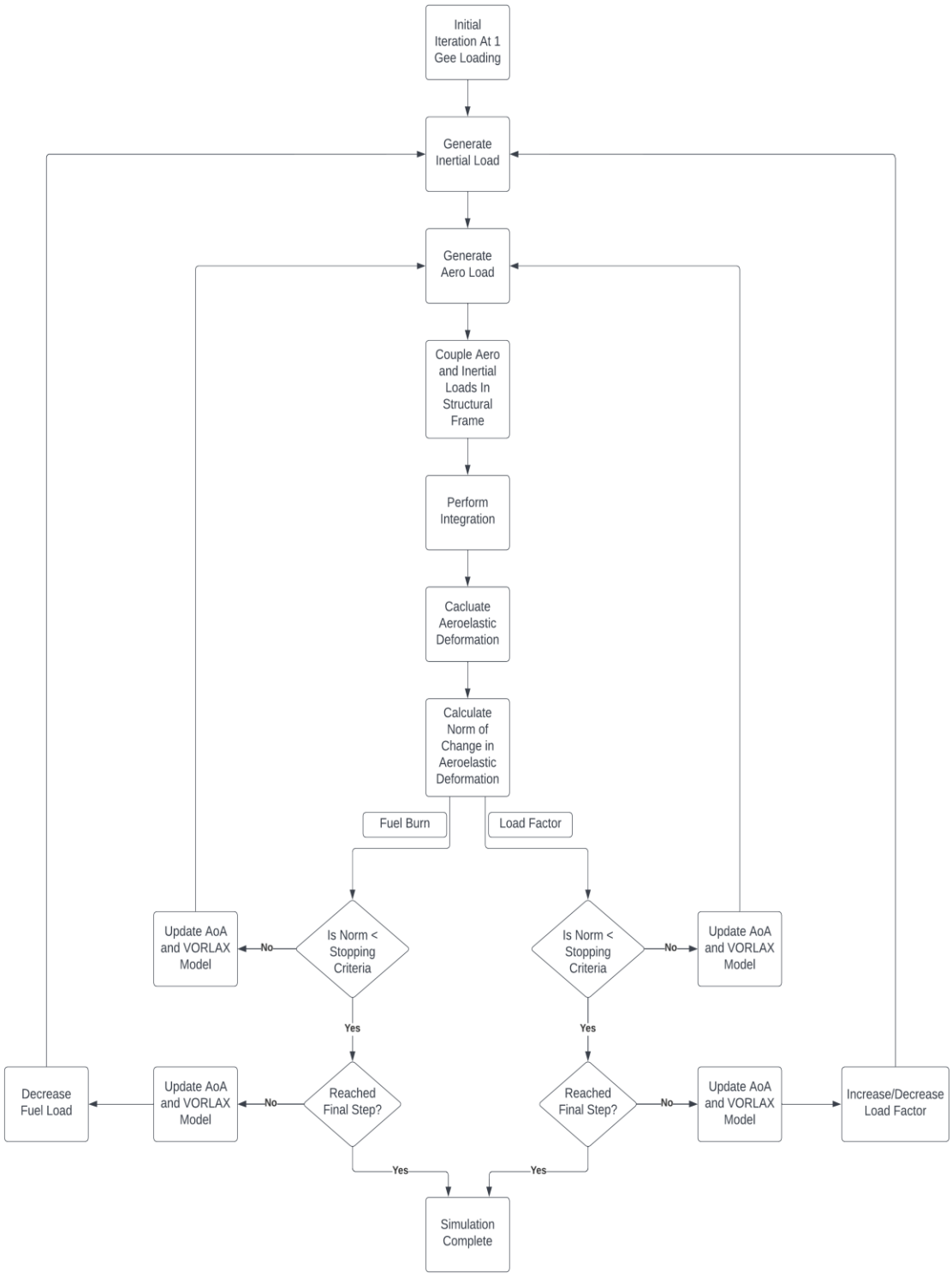

Figure 35. Load Factor and Constant C_L Fuel Burn Solution Procedure.

CHAPTER 7

RESULTS

1-gee Aeroelastic Effects

The first step in analyzing the four models/materials is to run a baseline 1-gee aeroelasticity simulation. As previously mentioned, this simulation aims to determine the jig shape of the wing. Since the wing experiences some amount of aeroelastic bending, the aeroelastic changes in twist and dihedral must be determined. It is accounted for in the shape of the jig. The jig is the design twist and dihedral with the aeroelastic increase in twist and dihedral subtracted off. In other words, it is the neutral wing shape that, when aeroelasticity is accounted for, the wing reaches its design twist and dihedral at 1-gee cruise conditions. The aeroelastic twist and dihedral for each of the four models are shown in Figures (36 – 43).

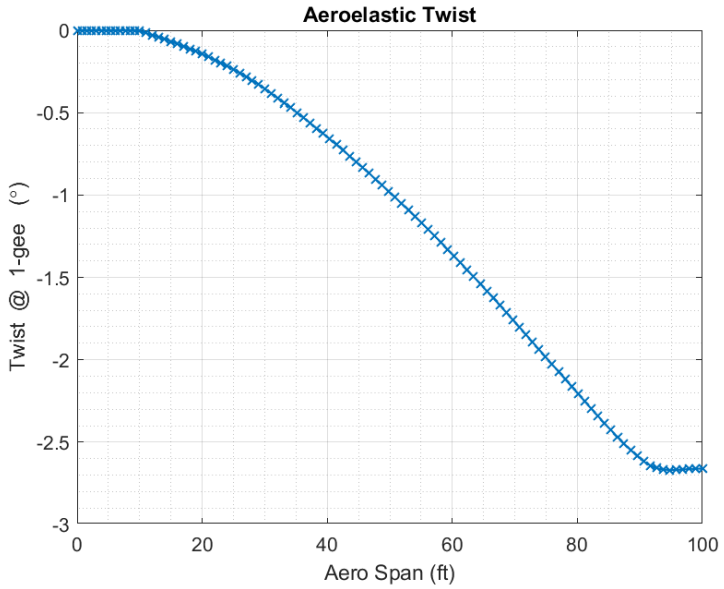

Figure 36. Aeroelastic Twist for 46-ksi Wing.

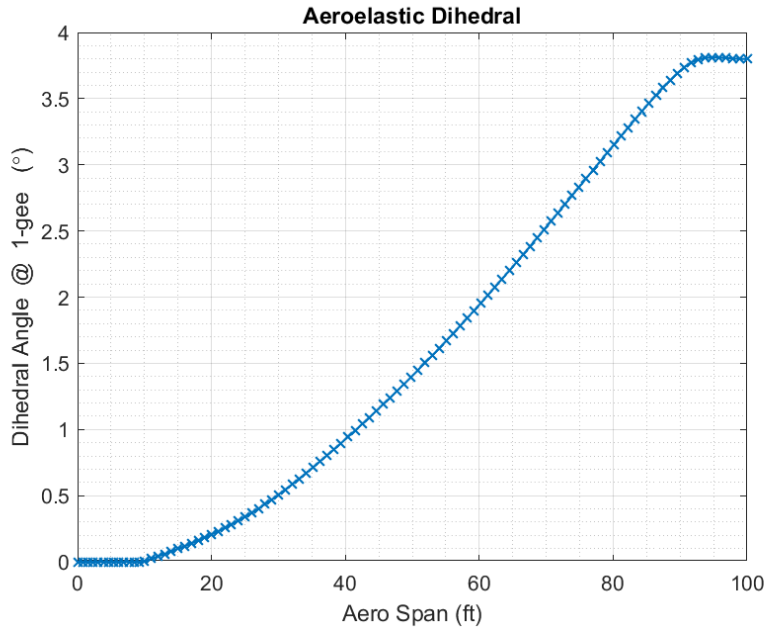

Figure 37. Aeroelastic Dihedral for 46-ksi Wing

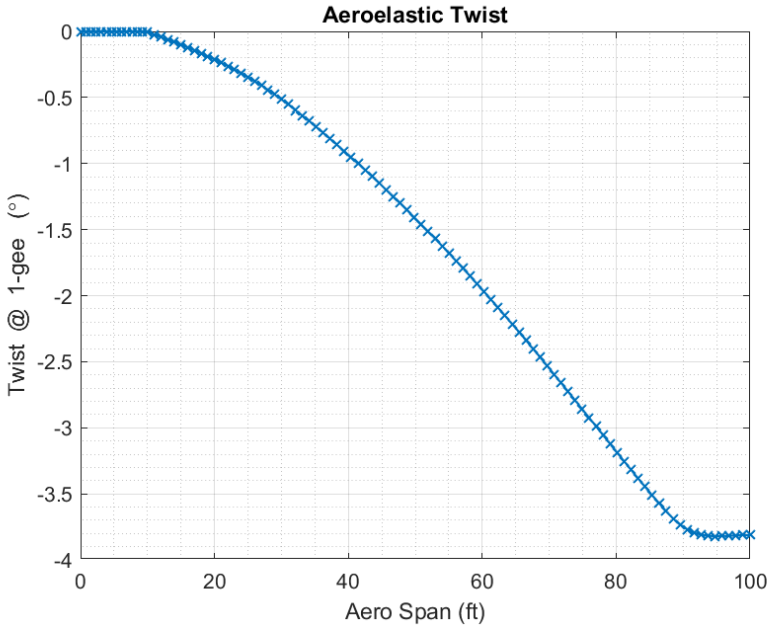

Figure 38. Aeroelastic Twist for 69-ksi Wing.

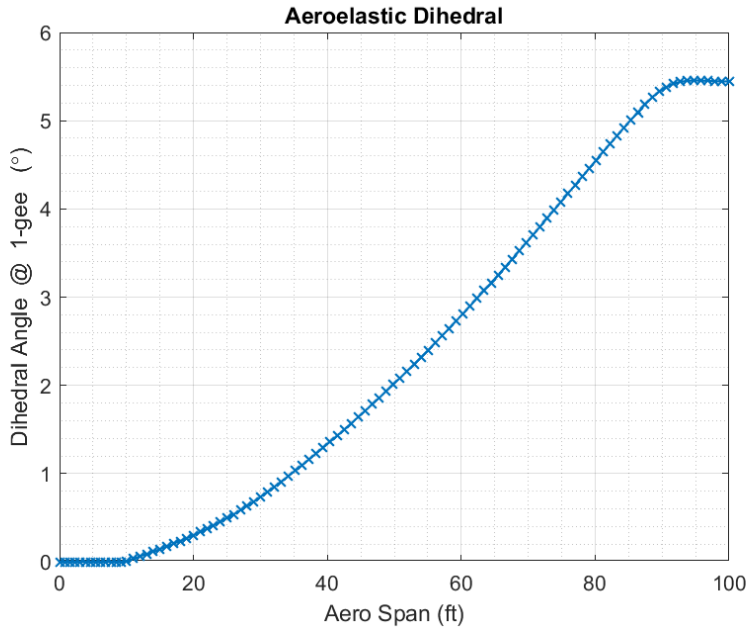

Figure 39. Aeroelastic Dihedral for 69-ksi Wing.

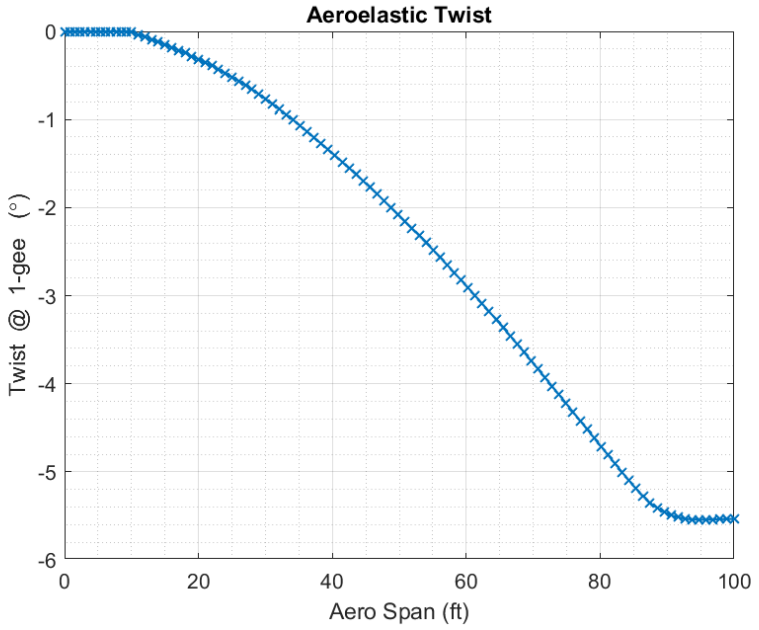

Figure 40. Aeroelastic Twist for 105-ksi Wing.

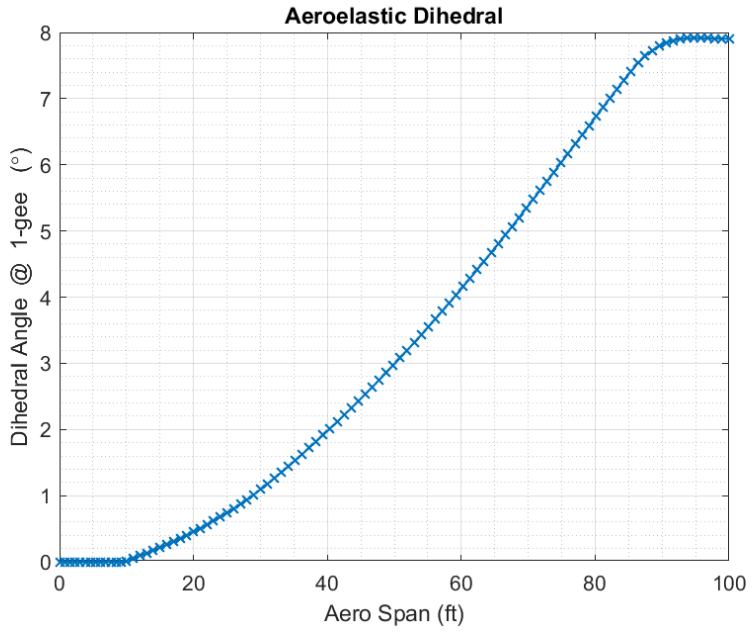

Figure 41. Aeroelastic Dihedral for 105-ksi Wing.

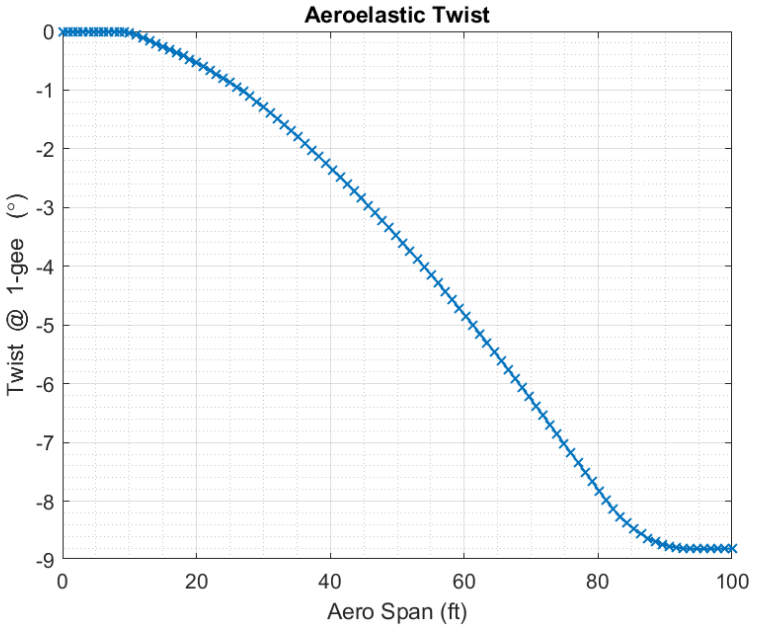

Figure 42. Aeroelastic Twist for 180-ksi Wing.

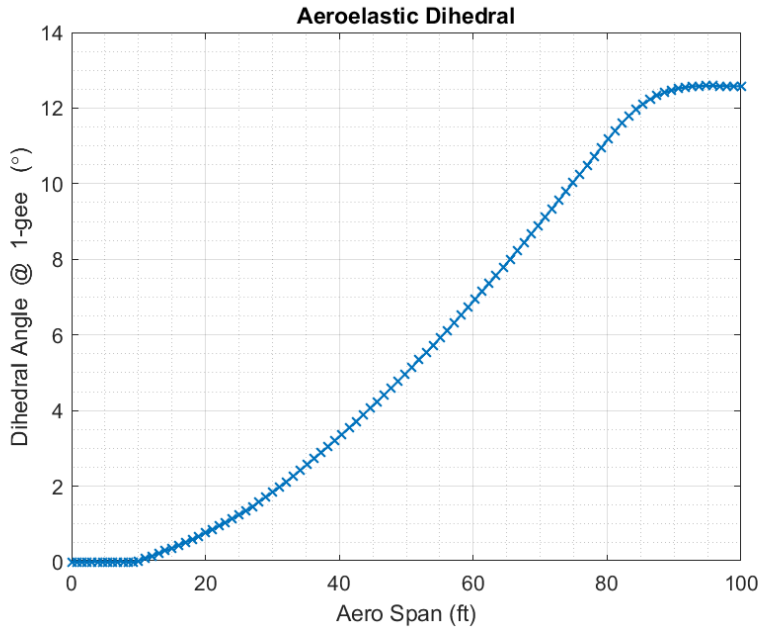

Figure 43. Aeroelastic Dihedral for 180-ksi Wing.

The aeroelastic twist on the 46-ksi wing is approximately -2.7° at the wingtip. This amount of aeroelastic twist is considerable. Recall from Figure (16) that the design twist features about eight degrees of washout from the side of body to the wingtip. An aeroelastic twist increment of -2.7° is an additional 37.5% of wing twist. The aeroelastic increment of the wing twist and dihedral angle for each wing is listed in Table (8).

Wing Model	Design Wing Washout	Aeroelastic Twist Increment	Percent Increase in Twist	Design Wing Dihedral	Aeroelastic Dihedral Increment	Percent Increase in Dihedral
46-ksi	8°	-2.7°	37.5%	5°	3.8°	76%
69-ksi		-3.8°	47.5%		5.4°	108%
105-ksi		-5.6°	70%		8°	160%
180-ksi		-8.8°	110%		12.5°	250%

Table 8. 1-gee Aeroelastic Wing Twist and Dihedral angle.

As the material strength increases, the aeroelastic twist increases. Comparable results are found with the aeroelastic dihedral increment. In fact, the percent increase in the wing dihedral angle is more significant than that of the wing twist. This work looks at aircraft performance; thus, the wing twist is of greater interest. However, the wing dihedral angle change could be quite detrimental to lateral handling characteristics.

The 1-gee aeroelastic increments of the wing twist and dihedral angle shown in the table and figures above lead to the jig shapes (neutral wing shape) shown in Figures (44 – 51).

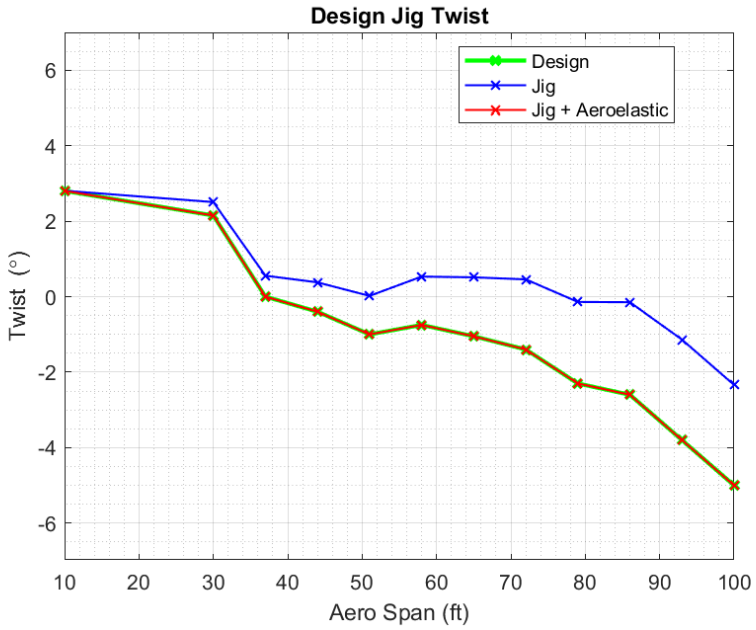

Figure 44. Jig Twist for 46-ksi Wing.

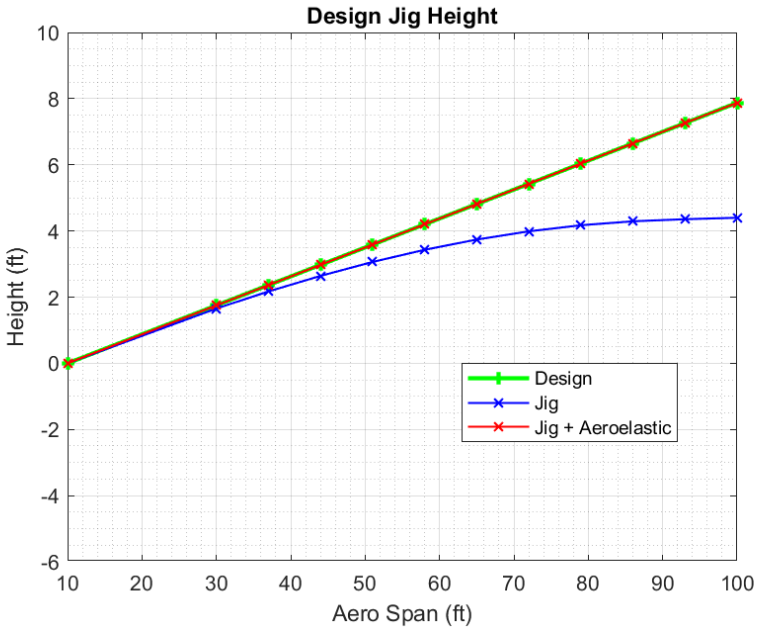

Figure 45. Relative Jig Height for 46-ksi Wing.

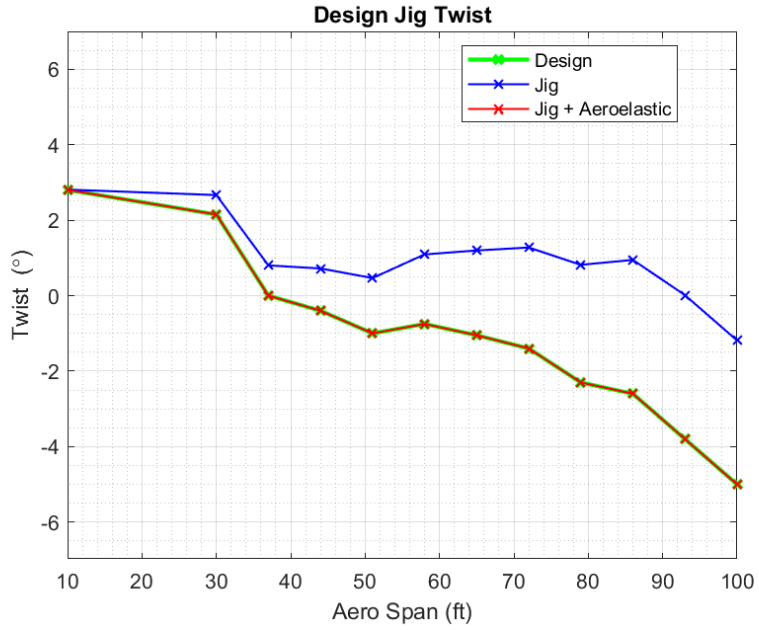

Figure 46. Jig Twist for 69-ksi Wing.

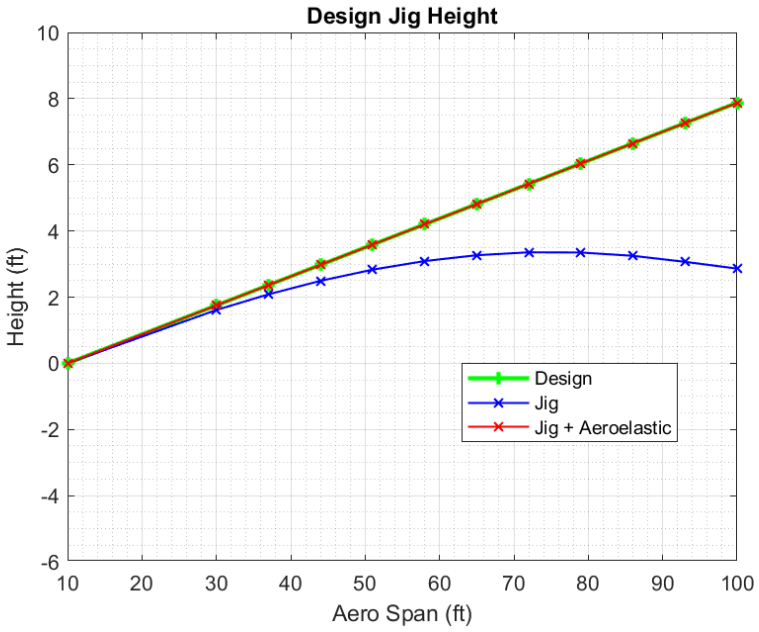

Figure 47. Relative Jig Height for 69-ksi Wing.

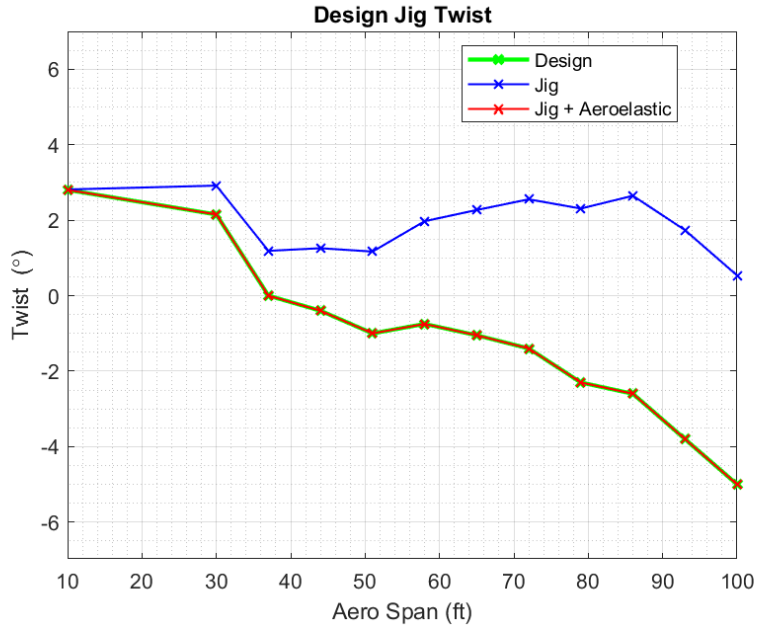

Figure 48. Jig Twist for 105-ksi Wing.

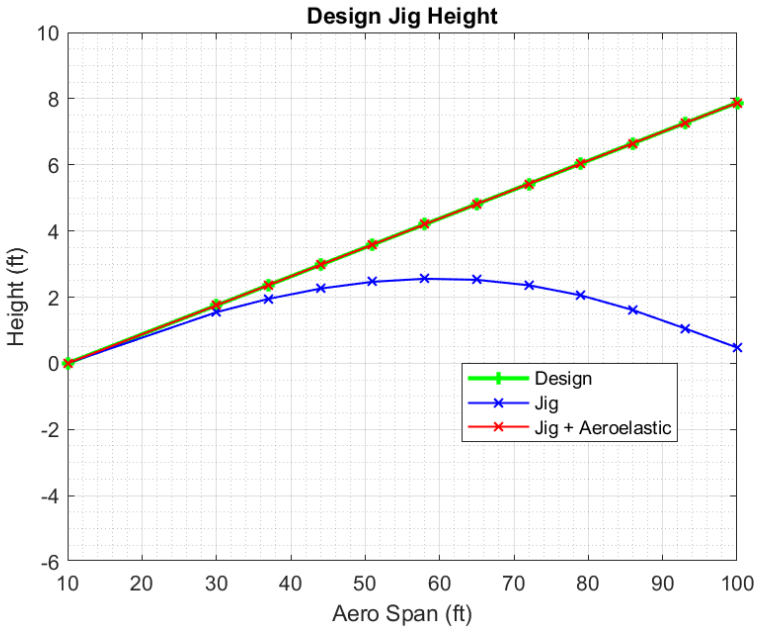

Figure 49. Relative Jig Height for 105-ksi Wing.

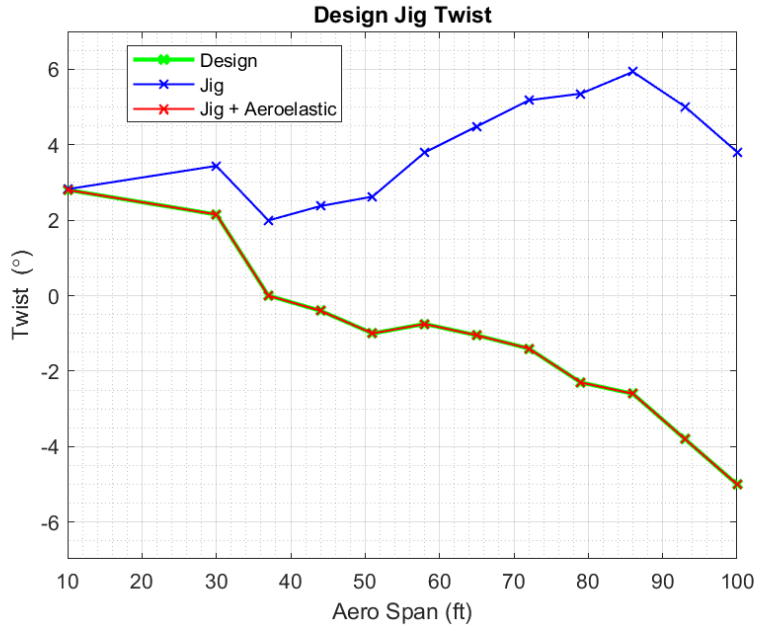

Figure 50. Jig Twist for 180-ksi Wing.

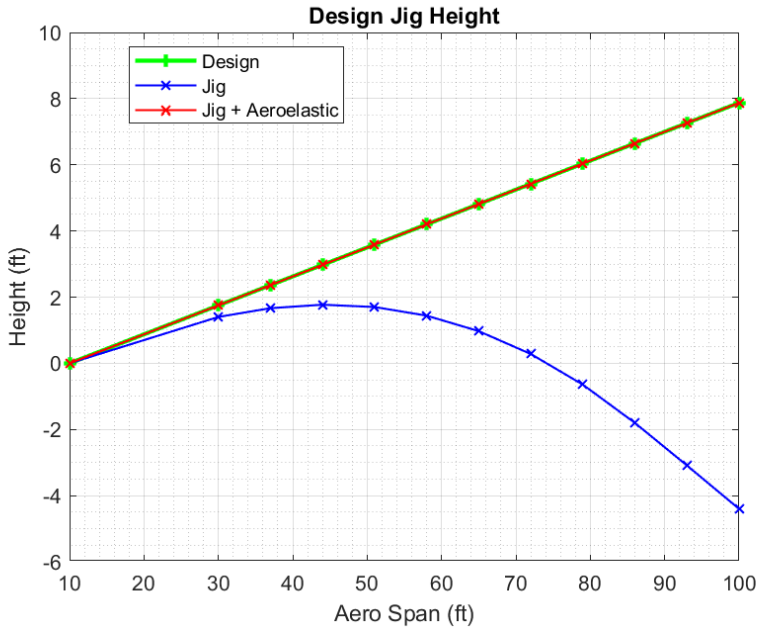

Figure 51. Relative Jig Height for 180-ksi Wing.

The 1-gee aeroelastic effects on the required jig shape are profound, even for the more rigid wings. The jig shape for the 46-ksi wing manages to resemble the in-flight design shape, albeit with lower magnitude twist and dihedral values. The amount of difference increases moving outboard along the wing. This behavior is not surprising since the wing is a beam with one end fixed to the fuselage.

As the material strength increases, the required jig shape resembles the design shape less and less. This is even the case for the 69-ksi wing. The jig for the 69-ksi wing begins to show a noticeable bow on the outer ¾ of the semi-span. The jig twist on most of the outer half of the 69-ksi wing is no longer negative, as was the case on the 46-ksi wing and the design twist distribution.

The differences between the jig and design shape continue to increase as one looks at the 105-ksi wing. Now, no part of the jig has a negative twist value. Furthermore,

the bow in the jig shape becomes even more pronounced on the 105-ksi wing, and the relative jig height at the wing tip is nearly the same as the wing at the side of body. Thus, the outboard half of the wing has a significant negative dihedral, or anhedral, angle.

As is to be expected, the 180-ksi wing shows the most significant differences between the design and jig shape. It should be noted and is shown later that it is believed that the amount of flexibility of the 180-ksi wing may exceed the limit at which linear bending can be assumed. Nevertheless, the results are profound. The jig twist is not only positive across the entire span but features wash-in compared to the desired washout. Further, over half of the jig is experiencing a negative dihedral angle, and the relative height of the wingtip is over four feet below the height of the wing at the side of body.

The jig shape allows the wing to obtain the in-flight design shape, so the significant differences between the jig shape and the design shape are not necessarily detrimental to aircraft performance. However, there are some potentially severe structural issues with a wing with such a high amount of flexibility. The most apparent structural concerns are cracking, especially with composites, delamination, and joint failure.

Aeroelastic Effects of nZ_{max}

In 14 CFR § 25.337, the positive limit load factor, nZ_{max}, is based on the maximum takeoff weight (*MTOW*) [26]. Thus, all four models/materials are exposed to a coupled aerodynamic and inertial load that is 2.5 times that of the coupled load at *MTOW*. The design cruise weight of each model is 500,000 lbm. Each model has an *MTOW* of 550,000 lbm. During the design process, it was assumed that the additional

50,000 lbm. was for either additional fuel or fuel spent before the design cruise point. Therefore, the aerodynamic and inertial loads in Table (6) are updated to the values shown in Table (9).

Model Material Strength	Ft_y = 46-ksi	Ft_y = 69-ksi	Ft_y = 105-ksi	Ft_y = 180-ksi
***MTOW* x nZ_{max}**	1,375,000 lbm.			
Aero-load x nZ_{max}	687,500 lbf.			
Structural Weight x nZ_{max}	100,000 lbm.	93,750 lbm.	87,500 lbm.	81,250 lbm.
Fuel Weight x nZ_{max}	275,000 lbm.	281,250 lbm.	287,500 lbm.	293,750 lbm.
Engine Weight x nZ_{max}	47,500 lbm.			

Table 9. Key Aircraft/Wing Inertial Loads at MTOW x nZ_{max}.

The aeroelastic effects of the nZ_{max} limit load on the wing twist distribution for each model are shown in Figures (52 – 55).

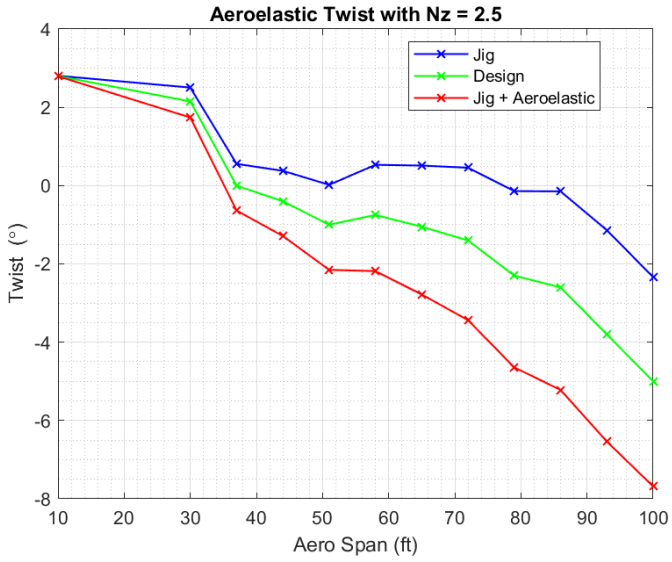

Figure 52. Wing Twist at nZ_{max} for 46-ksi Wing.

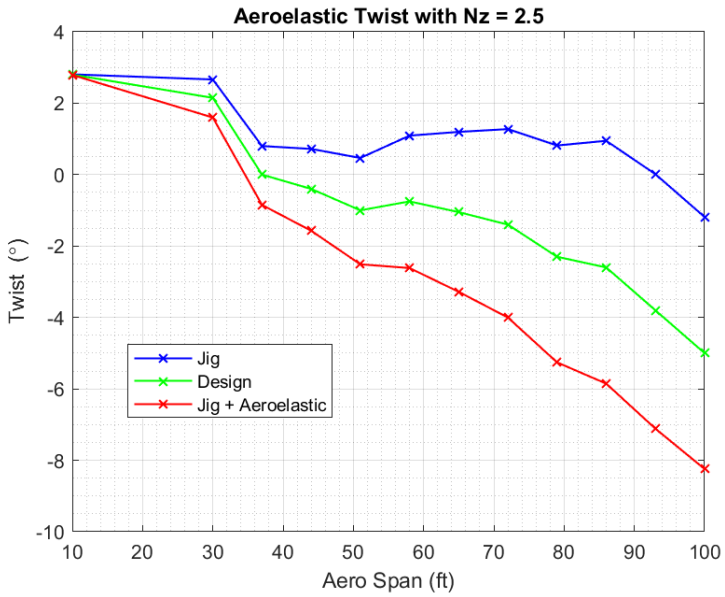

Figure 53. Wing Twist at nZ_{max} for 69-ksi Wing.

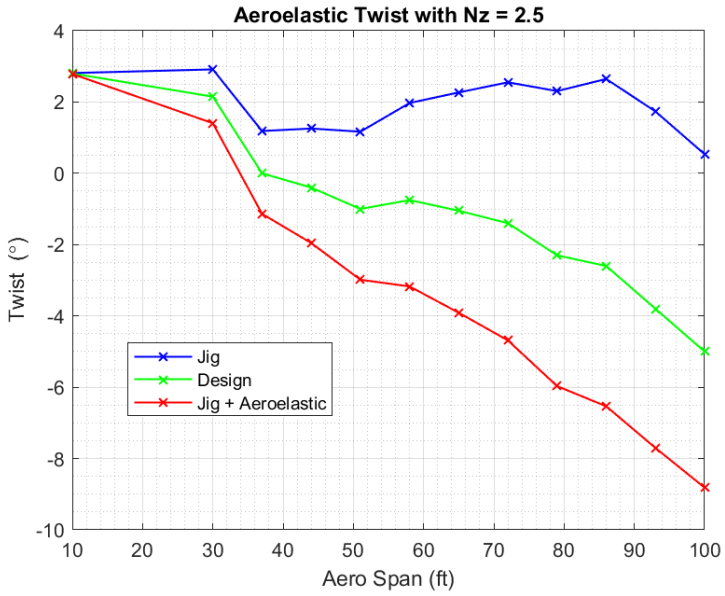

Figure 54. Wing Twist at nZ_{max} for 105-ksi Wing.

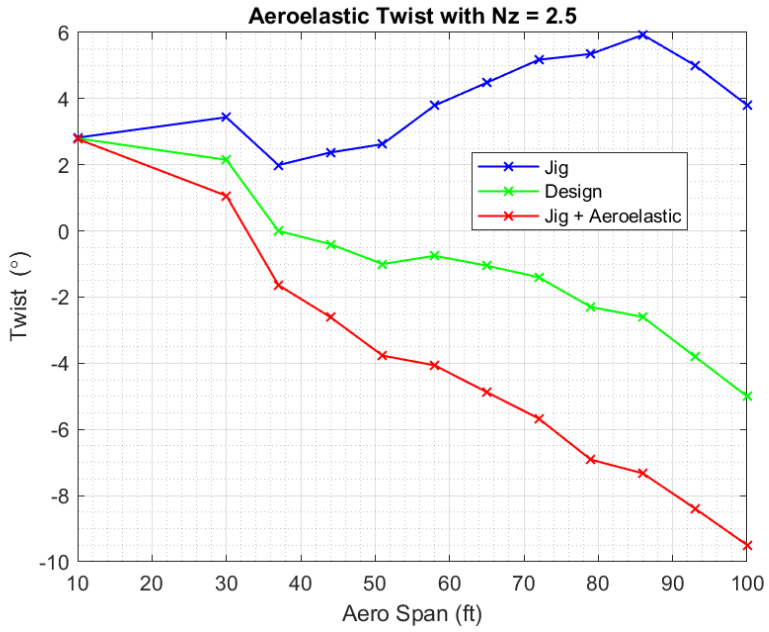

Figure 55. Wing Twist at nZ_{max} for 180-ksi Wing.

As the material strength increases and the wing becomes more flexible, the resulting wing twist diverges further from the design twist. In all four cases, the resulting wing twist distribution is more negative than the design, which is to be expected. As the wing bends upwards, the projection of that deflection into the aero-reference frame appears as a decrease in the wing twist. The change in the wing washout for each model is shown in Table (10).

Wing Model	Design Washout	Wing Washout at nZ_{max}	Percent Increase in Washout
46-ksi	8°	10.5°	31.25%
69-ksi		11.25°	40.625%
105-ksi		12°	50%
180-ksi		12.5°	56.25%

Table 10. Wing Washout at nZ_{max}.

The increased washout for each wing is due to the increase in wing bending. The aeroelastic wing deflection for each wing at nZ_{max} is shown in Figures (56 – 59).

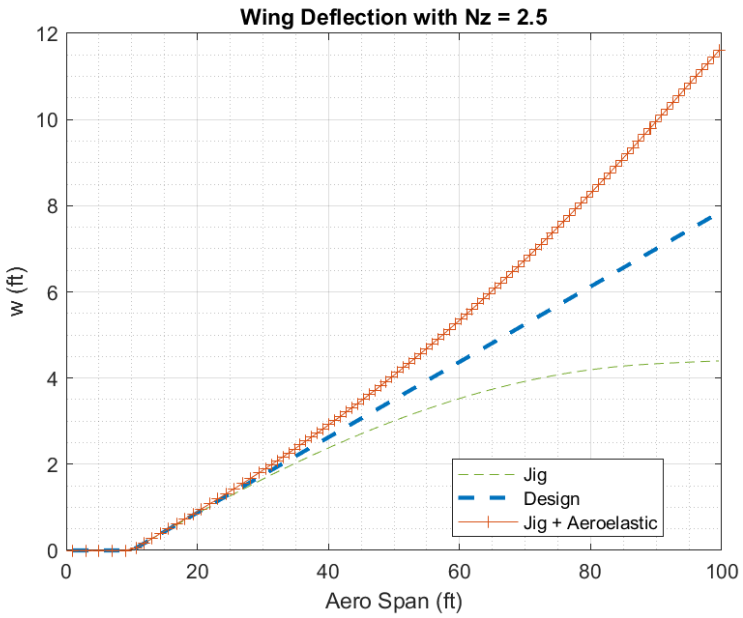

Figure 56. Wing Deflection at nZ_{max} for 46-ksi Wing.

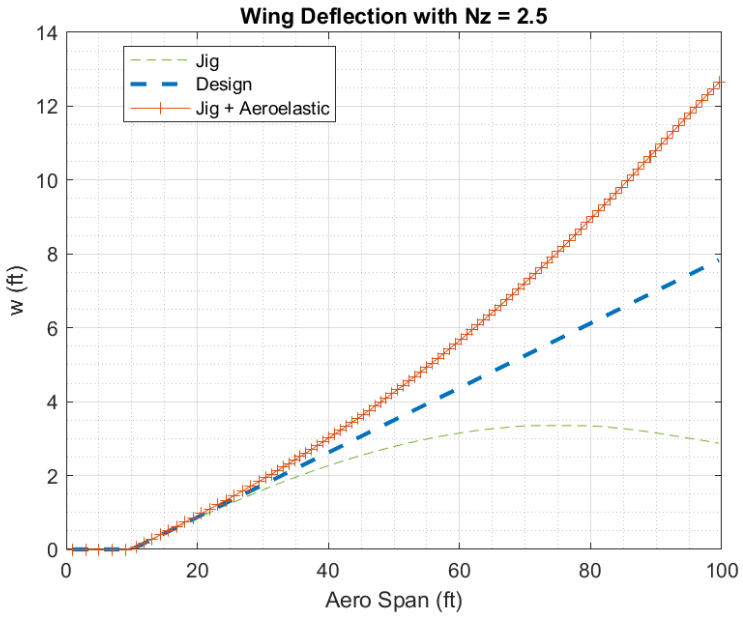

Figure 57. Wing Deflection at nZ_{max} for 69-ksi Wing.

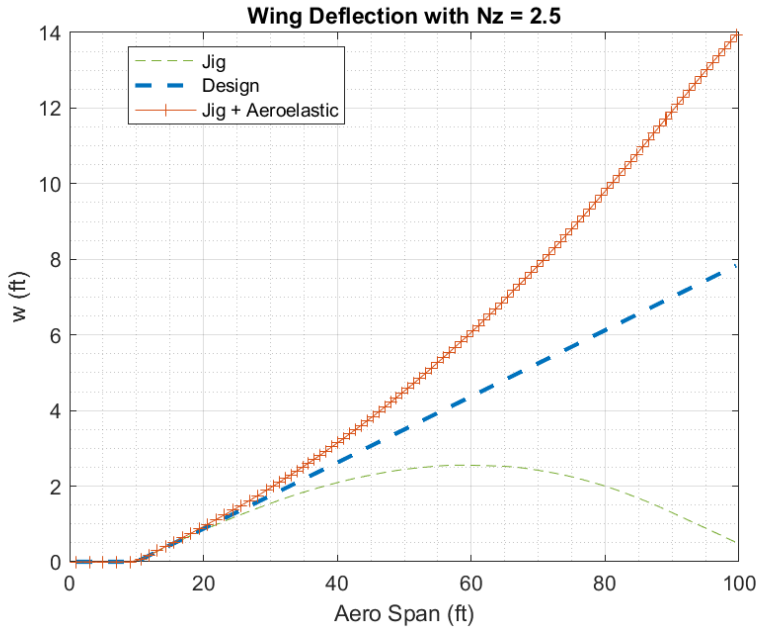

Figure 58. Wing Deflection at nZ_{max} for 105-ksi Wing.

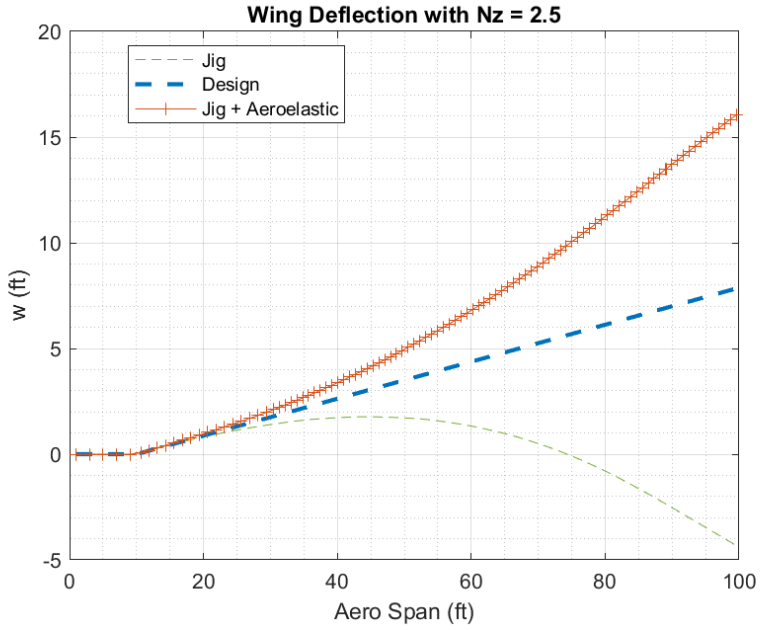

Figure 59. Wing Deflection at nZ_{max} for 180-ksi Wing.

From these figures, one can see that the wingtip deflection at nZ_{max} ranges from 11.5 feet for the 46-ksi wing to 16 feet for the 180-ksi wing. The design wingtip deflection at cruise is 7.85 feet.

The changes in the wing twist and deflection significantly impact the wing's spanwise lift distribution and pressure distribution. The spanwise lift distribution at nZ_{max} for each wing is shown in Figures (60 – 63).

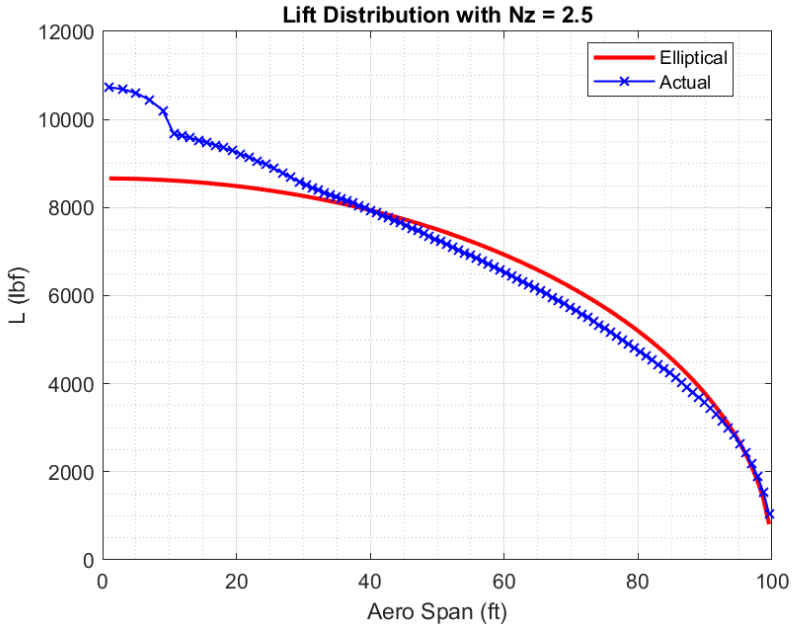

Figure 60. Spanwise Lift Distribution at nZ_{max} for 46-ksi Wing.

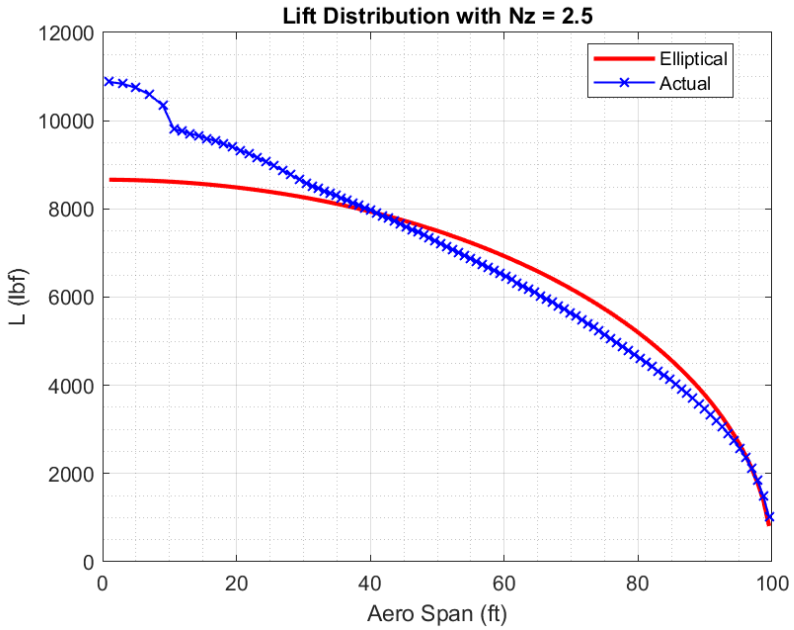

Figure 61. Spanwise Lift Distribution at nZ_{max} for 69-ksi Wing.

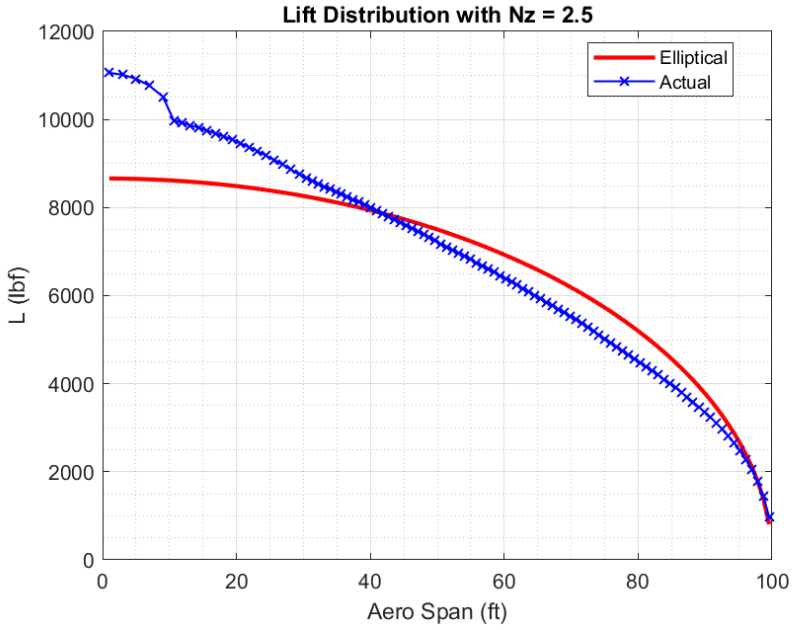

Figure 62. Spanwise Lift Distribution at nZ_{max} for 105-ksi Wing.

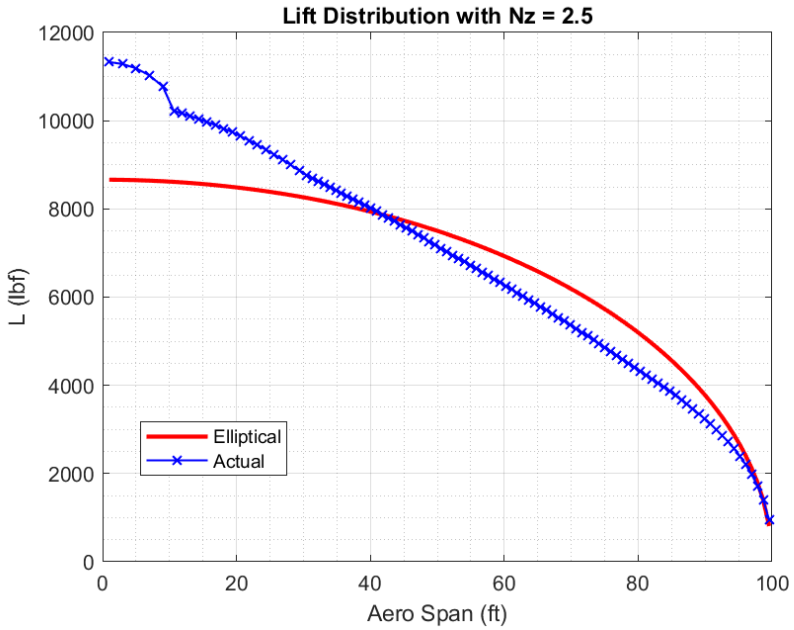

Figure 63. Spanwise Lift Distribution at nZ_{max} for 180-ksi Wing.

The spanwise lift distribution becomes less elliptical as the material strength increases. The 105-ksi and 180-ksi wings, particularly, have a very triangular-shaped spanwise lift distribution. This certainly increases the lift-induced drag. The upper surface critical flow conditions for each wing at nZ_{max} are shown in Figures (64 – 67).

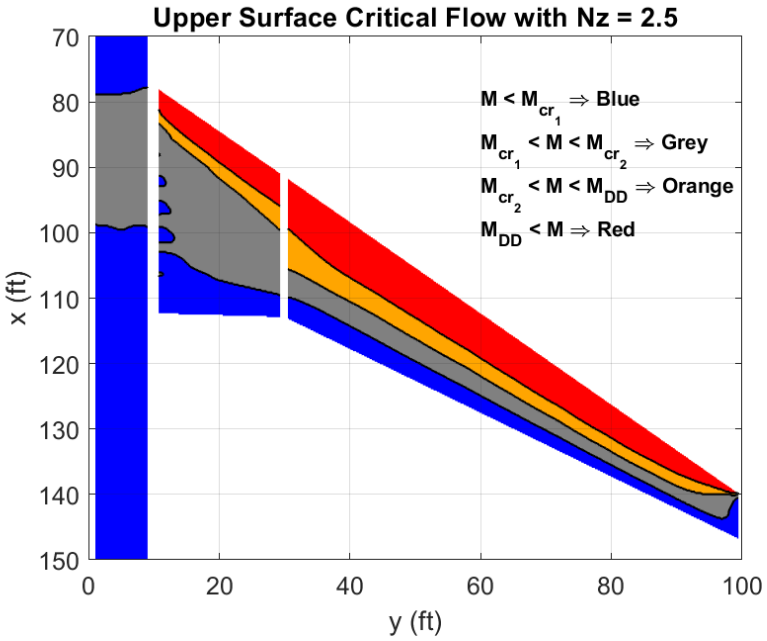

Figure 64. Upper Surface Critical Flow at nZ_{max} for 46-ksi Wing.

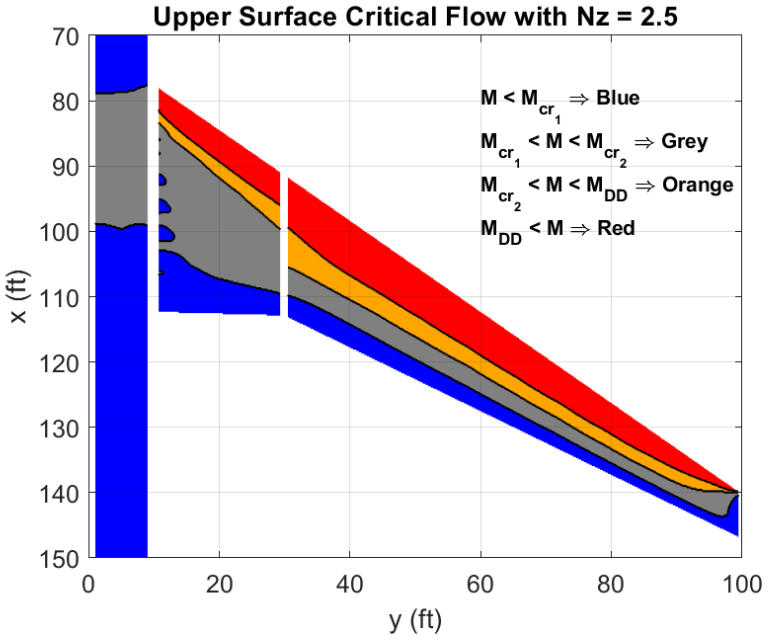

Figure 65. Upper Surface Critical Flow at nZ_{max} for 69-ksi Wing.

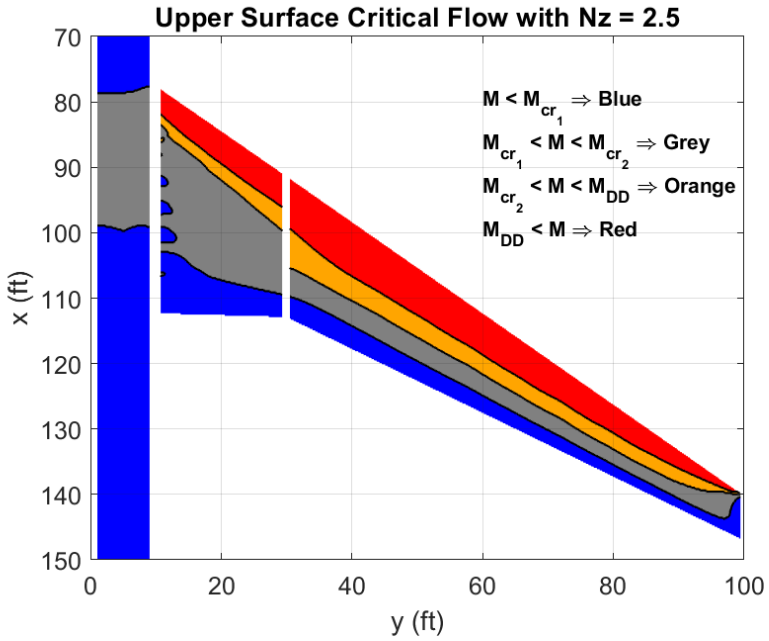

Figure 66. Upper Surface Critical Flow at nZ_{max} for 105-ksi Wing.

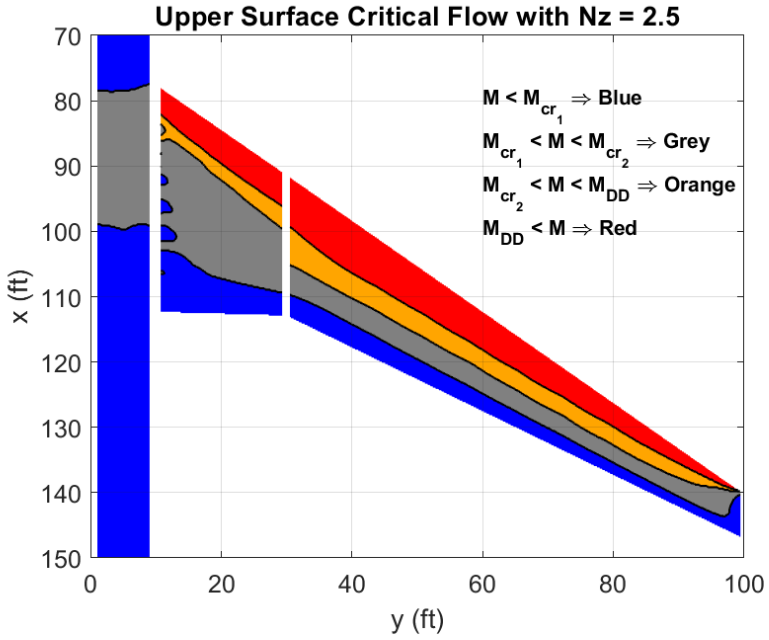

Figure 67. Upper Surface Critical Flow at nZ_{max} for 180-ksi Wing.

Recall that the red regions indicate flow exceeding $M_{DD,}$ and the orange regions indicate flow exceeding M_{cr}. The significant regions of red suggest that all four wings have strong shockwaves. This is not that surprising, given the flight conditions at nZ_{max}.

Aeroelastic Effects of nZ_{min}

As with nZ_{max}, 14 CFR § 25.337 specifies that the negative limit maneuver load of nZ_{min} be applied to the aircraft at its *MTOW* [26]. Thus, the coupled aerodynamic and inertial loads are the negative of the coupled load at *MTOW* to correspond to the prescribed nZ_{min} of -1.0. The applied loads for each model are shown in Table (11).

Model Material Strength	**Ft_y = 46-ksi**	**Ft_y = 69-ksi**	**Ft_y = 105-ksi**	**Ft_y = 180-ksi**
***MTOW* x nZ_{min}**	-550,000 lbm.			
Aero-load x nZ_{min}	-275,000 lbf.			
Structural Weight x nZ_{min}	-40,000 lbm.	-37,500 lbm.	-35,000 lbm.	-32,500 lbm.
Fuel Weight x nZ_{min}	-110,000 lbm.	-112,500 lbm.	-115,000 lbm.	-117,500 lbm.
Engine Weight x nZ_{min}	19,000 lbm.			

Table 11. Key Aircraft/Wing Inertial Loads at MTOW x nZ_{min}.

The effects of the nZ_{min} load factor on the wing twist are shown in Figures (68 – 71).

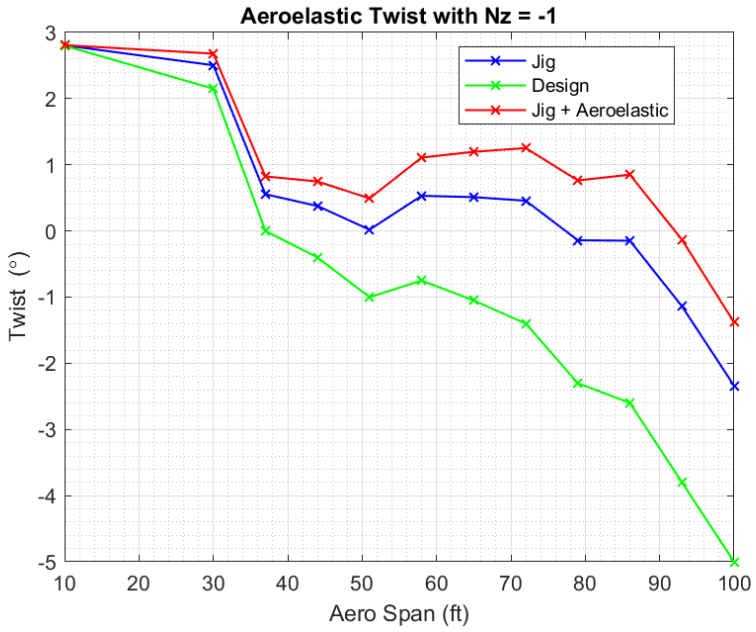

Figure 68. Wing Twist at nZ_{min} for 46-ksi Wing.

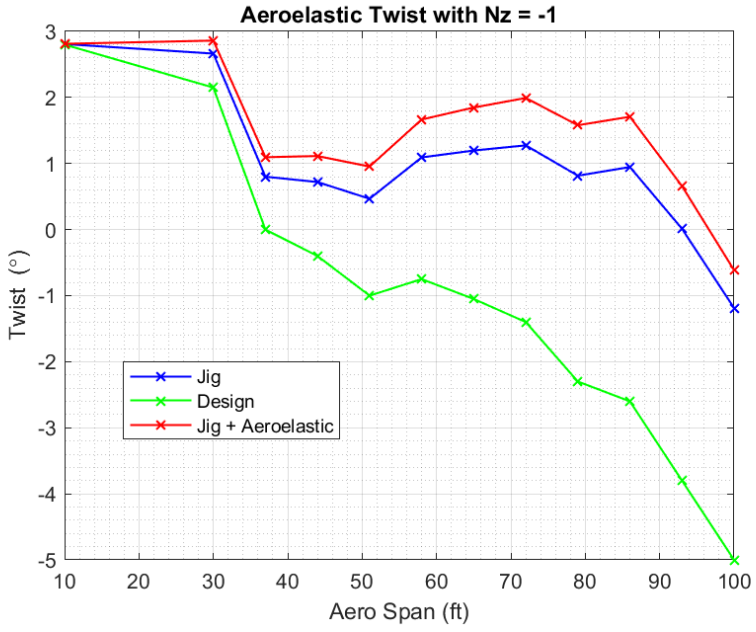

Figure 69. Wing Twist at nZ_{min} for 69-ksi Wing.

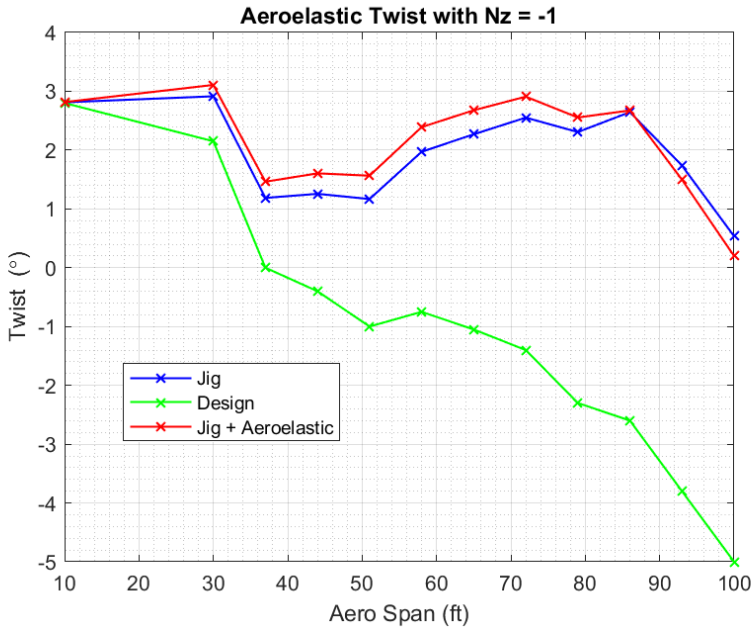

Figure 70. Wing Twist at nZ_{min} for 105-ksi Wing.

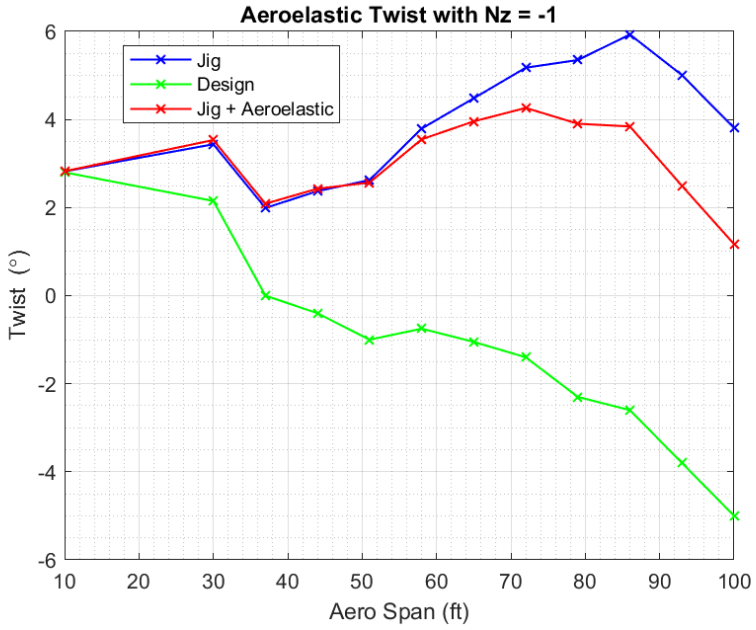

Figure 71. Wing Twist at nZ_{min} for 180-ksi Wing.

The coupled load at nZ_{min} is inverted; thus, the wing is bending down instead of upwards. The downward bending projected into the aero-reference frame appears as

wash-in of the wing twist. This is the behavior seen on the 46-ksi and 69-ksi wings. The jig plus aeroelastic twist is more positive or less negative across the wingspan when compared to the neutral jig shape or the design twist. The behavior of the 105-ksi and 180-ksi wings is one of the first indications that suggested the potential for non-linear bending. Both wings show an increase in the wing washout on the outboard, 10% and 50% of the wing, respectively. The expected result is a wing with less washout.

Examining this further, the wing deflection at nZ_{min} for each wing is shown in Figures (72 – 75).

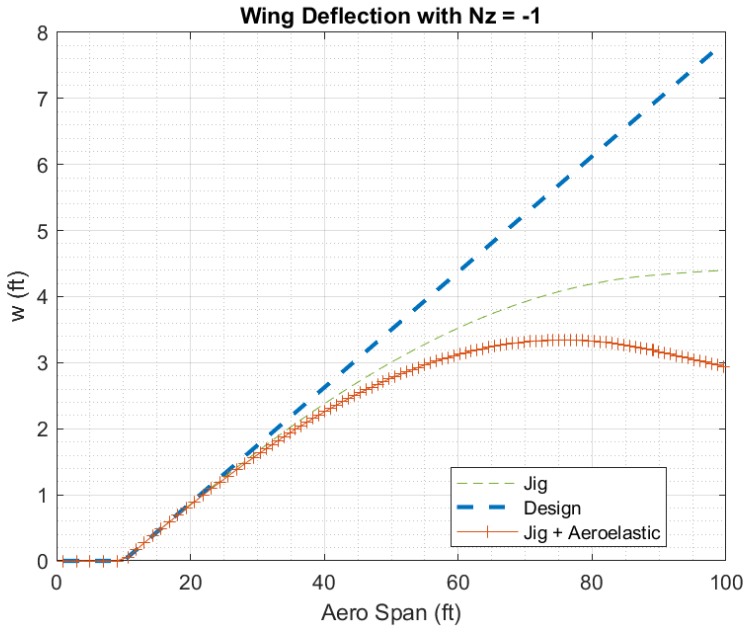

Figure 72. Wing Deflection at nZ_{min} for 46-ksi Wing.

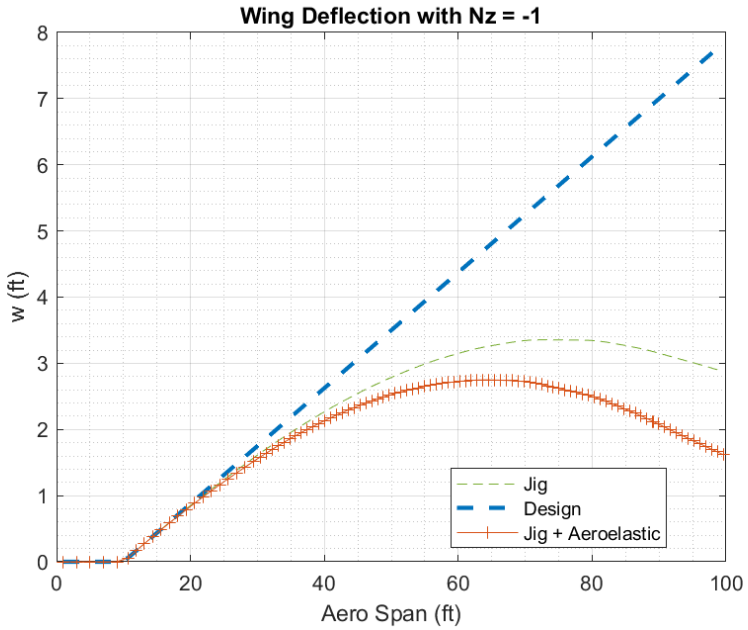

Figure 73. Wing Deflection at nZ_{min} for 69-ksi Wing.

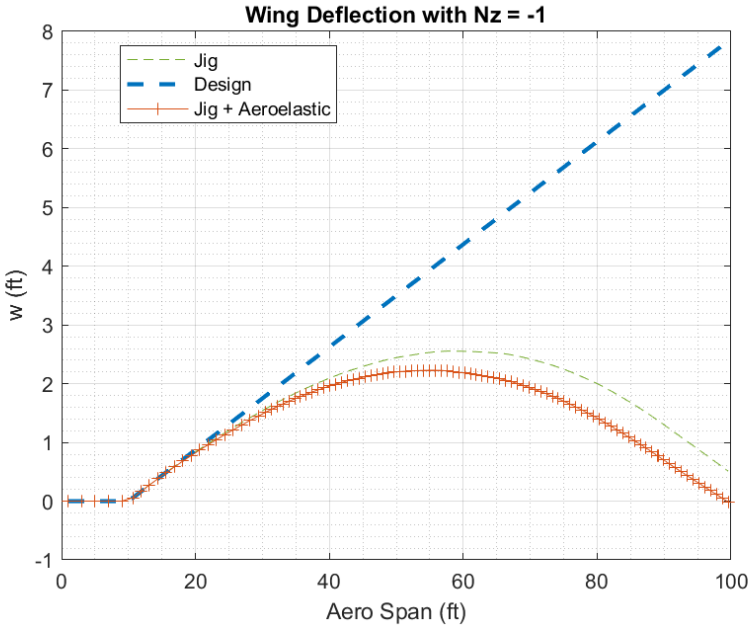

Figure 74. Wing Deflection at nZ_{min} for 105-ksi Wing.

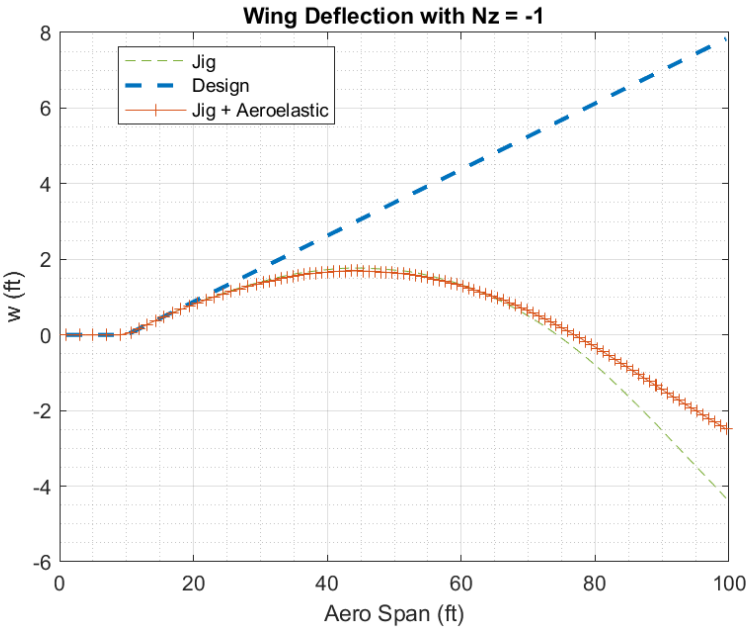

Figure 75. Wing Deflection at nZ_{min} for 180-ksi Wing.

The behavior of the 180-ksi wing in Figure (75) is unexpected. The wing should be deflected downwards from the neutral jig shape. Instead, it is bending upwards on the outboard portion of the wing. One of the primary assumptions of linear elasticity is that the deformations are small. The author believes this assumption of small deformations is not valid in the case of the 180-ksi wing and possibly the 105-ksi wing. Therefore, linear elasticity cannot be applied.

If it is indeed the case that the large deflections at nZ_{min} and nZ_{max} are no longer within the linear regime, it does not entirely negate the use of linear elasticity. These are the extremes of the expected maneuvering load factors. Most aircraft experience much smaller load factors, slightly above and below 1-gee, during ascent and descent, respectively. The deformations at these load factors are much less. Furthermore, the expected deformations with the change in fuel load are also less. If the theoretical

efficiency gained by using the lighter weight and more flexible wings is offset by the degradation of the aerodynamic performance, the loss will occur during typical ascent, cruise with fuel burn, and descent load factors and their associated wing deflection. Therefore, the analysis switches to the changing inertial load associated with a constant C_L fuel burn.

Aeroelastic Effects of Constant C_L Fuel Burn

The constant C_L fuel burn was simulated in 10% increments. At each step, 10% of the total fuel load would be removed, beginning at the wingtip, and working towards the side of body. When the fuel is removed, the altitude of the next step is adjusted in 500-foot increments to keep the C_L constant. The wing twist of each model at 80%, 60%, 40%, and 20% fuel loads are shown in Figures (76 – 79).

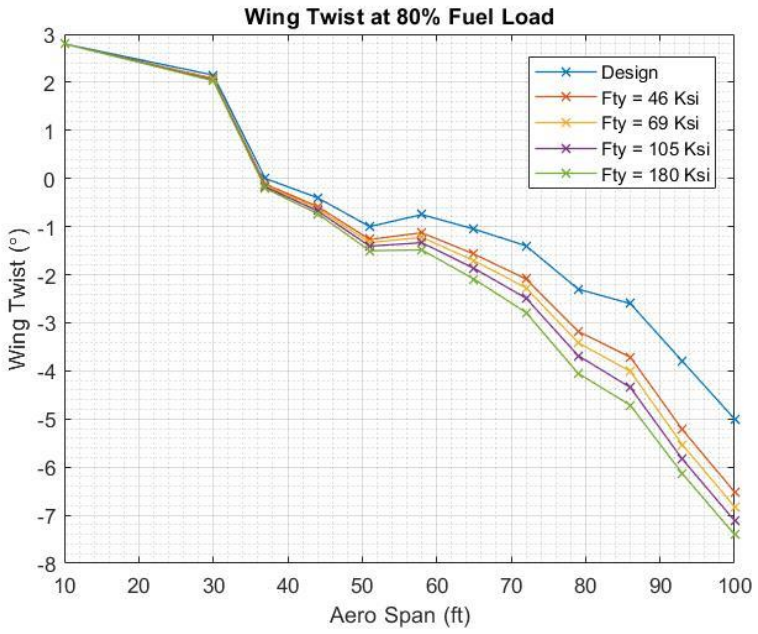

Figure 76. Wing Twist at 80% Fuel Load.

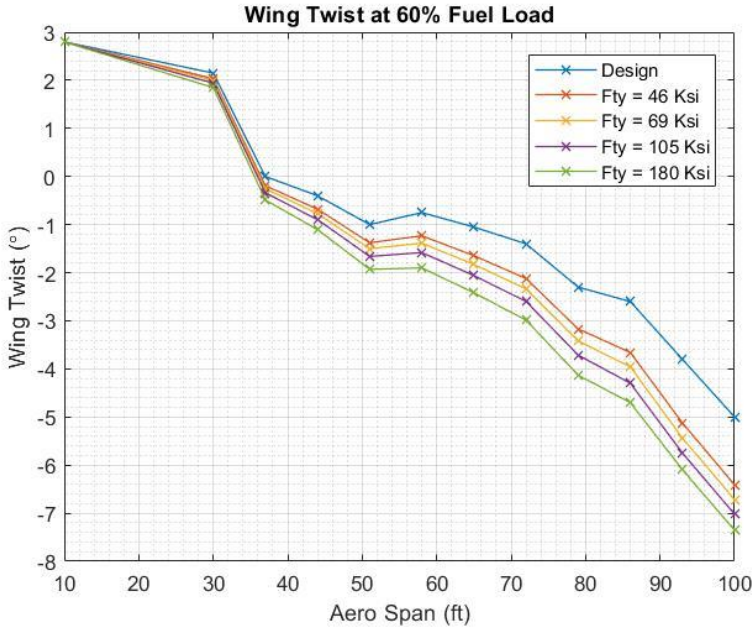

Figure 77. Wing Twist at 60% Fuel Load.

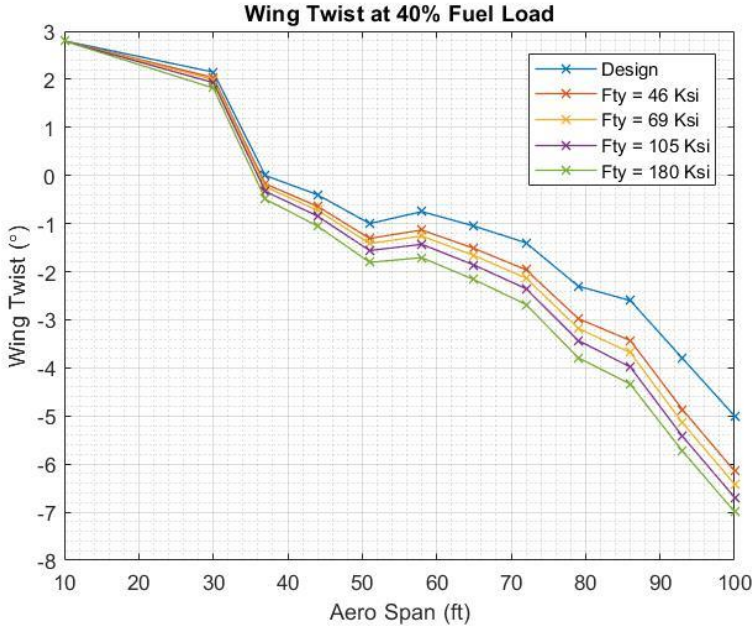

Figure 78. Wing Twist at 40% Fuel Load.

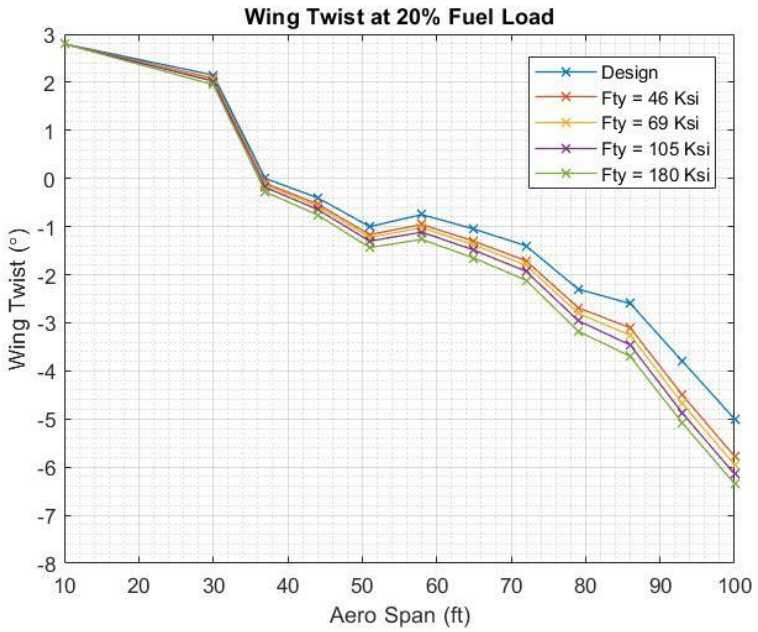

Figure 79. Wing Twist at 20% Fuel Load.

There are some interesting results to take away from these figures. The first is that the departure of the wing twist from the design twist is more significant at higher fuel loads. There is a substantial increase in the wing washout at the 80% fuel load. This increase in the wing washout is not just at the wingtip where the fuel load is removed. The not-insubstantial decrease in the wing twist can be seen over the entire outboard half of the wingspan. The next thing to notice is that this increase in the wing washout becomes even more significant at the 60% fuel load. Despite the reduced aerodynamic load, a consequence of the reduced overall weight, the loss in inertial relief from the fuel weight is causing the wing to deflect more than desired. The wing deflection of the 46-ksi and 180-ksi wings is shown in Figures (80 – 83).

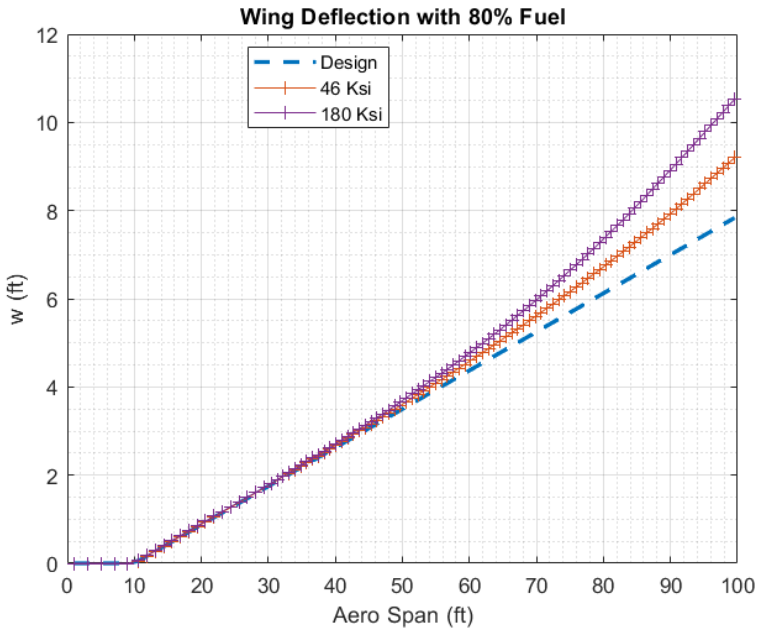

Figure 80. Wing Deflection at 80% Fuel Load for 46-ksi and 180-ksi Wings.

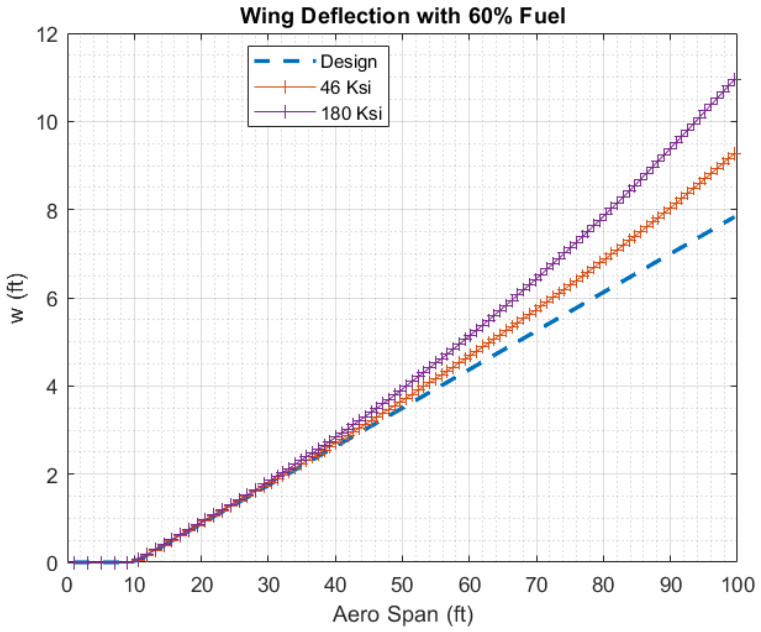

Figure 81. Wing Deflection at 60% Fuel Load for 46-ksi and 180-ksi Wings.

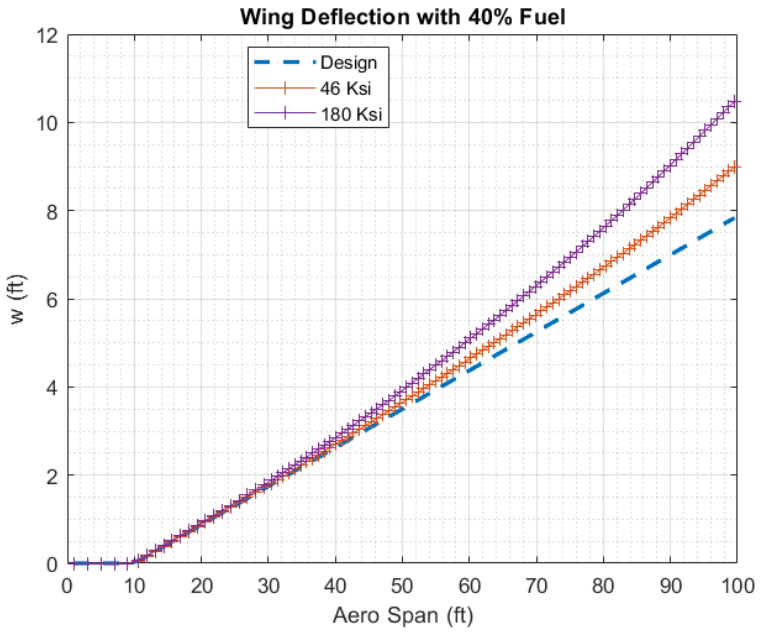

Figure 82. Wing Deflection at 40% Fuel Load for 46-ksi and 180-ksi Wings.

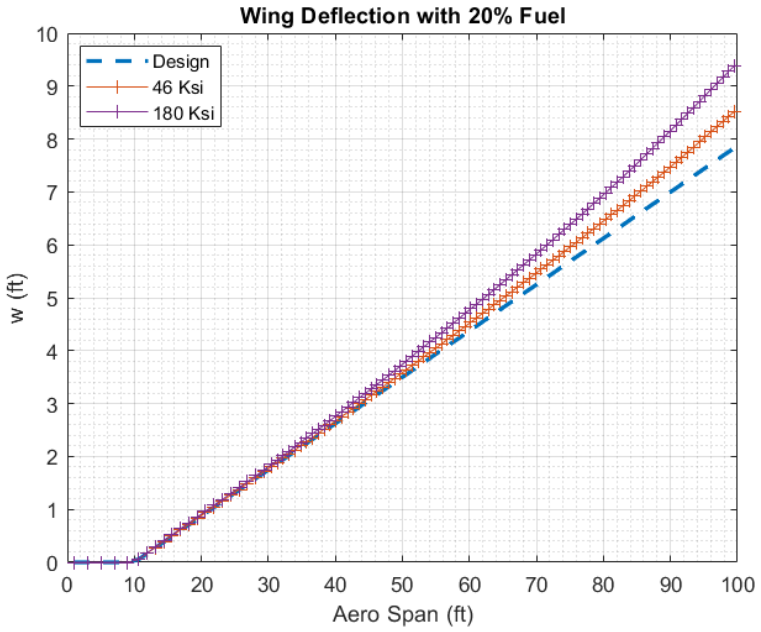

Figure 83. Wing Deflection at 20% Fuel Load for 46-ksi and 180-ksi Wings.

At the 80% fuel load, the wingtip for the 46-ksi wing is deflected almost 1.5 feet above the design point, whereas the wingtip for the 180-ksi wing is deflected about 2.5 feet.

This can be explained by the fact that the 20% loss in the fuel load is more significant for the 180-ksi wing than for the 46-ksi wing because the initial fuel load is greater for the 180-ksi wing. Add to the fact that the flexural rigidity, *EI*, of the 180-ksi wing is lower than the 46-ksi wing and thus is more susceptible to wing bending. When one looks at the 60% fuel load, the wingtip deflection has marginally increased on the 46-ksi wing. However, the wingtip deflection on the 180-ksi wing has increased by approximately 6 inches.

As the fuel load continues to decrease, the wing deflection begins to decrease. There is a decrease in the departure of the wing twist from the design values that is a consequence of the decreased wing deflection. This suggests that at around the 50% fuel load, the decrease in aerodynamic load begins to catch up with the loss in the inertial relief provided by the fuel weight. The change in the wing twist as a function of the fuel load at four spanwise locations is shown in Figures (84 – 87).

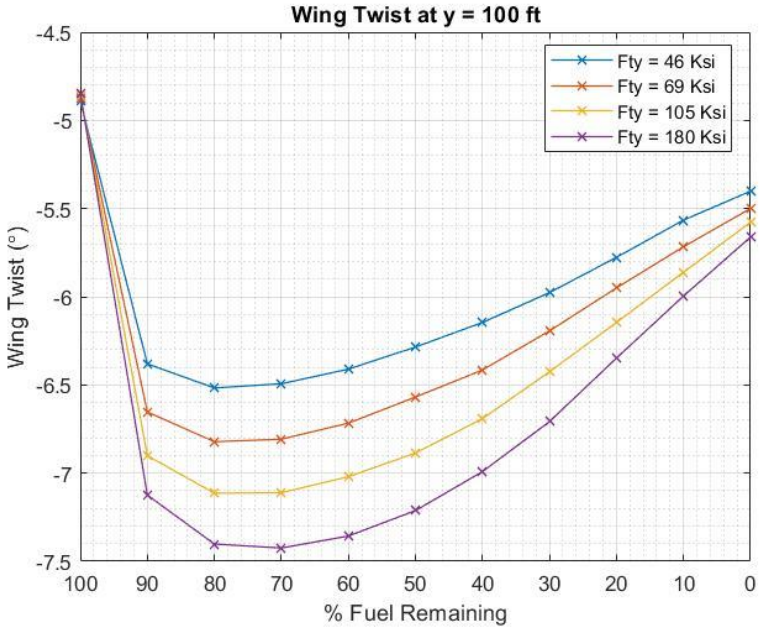

Figure 84. Wing Twist as a Function of the Fuel Load at the Wingtip.

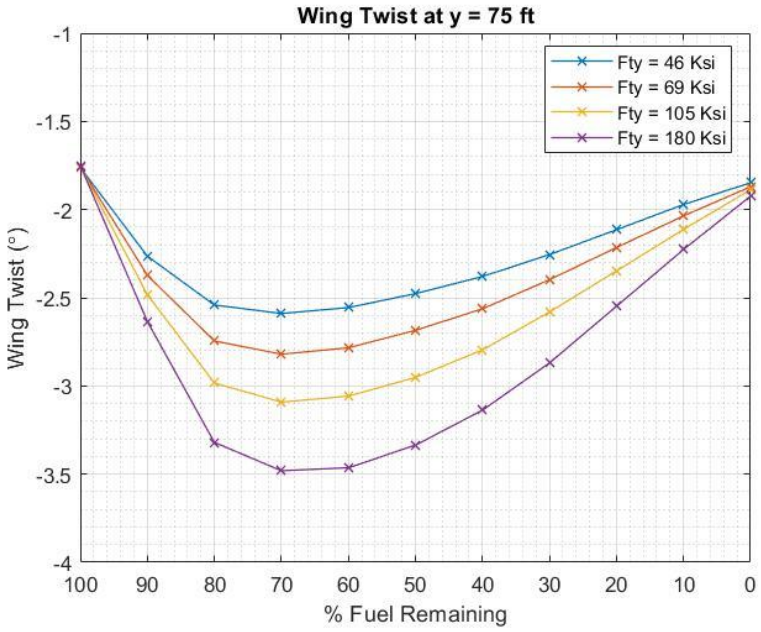

Figure 85. Wing Twist as a Function of the Fuel Load at the ¾ Semi-Span.

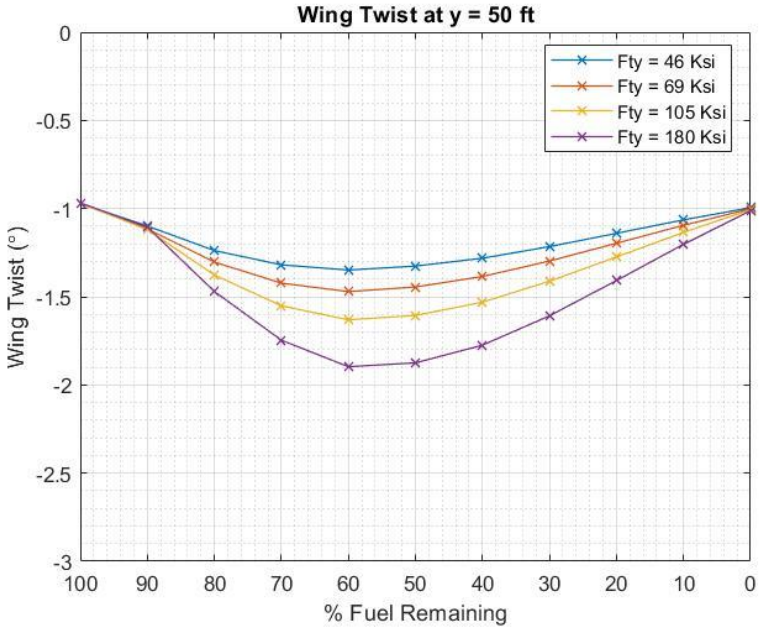

Figure 86. Wing Twist as a Function of the Fuel Load at the ½ Semi-Span.

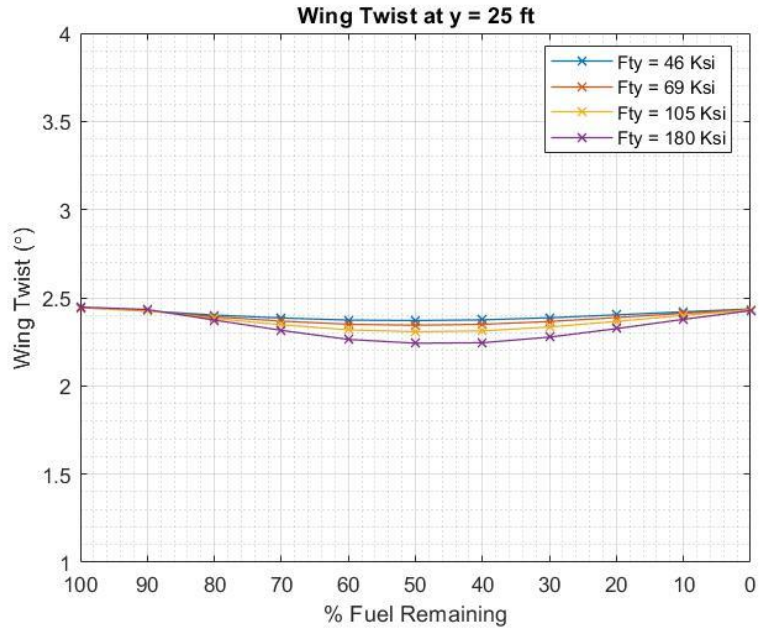

Figure 87. Wing Twist as a Function of the Fuel Load at the ¼ Semi-Span.

These figures further suggest that initially, the loss in inertial relief from the fuel load has more of an impact on the wing twist than the decrease in the overall aircraft weight. As

the fuel load continues to decrease, the lower aerodynamic load from the reduced aircraft weight begins to compensate for the loss in inertial relief. The fuel load where this begins to be felt depends on the location on the wing. At the wingtip and ¾ semi-span locations, the initial increase in the wing twist begins to subside at the 80% and 70% fuel loads, respectively. Moving inboard, this behavior does not begin until the 60% fuel load at the ½ semi-span location and the 50% fuel load at the ¼ semi-span location.

Since the fuel is first removed at the wingtips, the most significant changes in the wing twist occur at the wingtip and decrease as one moves inboard along the wing. Further, by the time the wing twist begins to depart from the design values on the inboard portions of the wing, the decreased aircraft weight has caught up to the decreased inertial relief. Thus, the overall magnitude of the wing twist departure is dampened. One can start to understand how these results might change had the fuel been unloaded from the inboard part of the wing and then moved outwards. In this case, one would likely not see the magnitude of the wingtip deflection shown in Figures (80 – 83).

Furthermore, as you move inboard on the wing, the torque box becomes larger, and the sectional aerodynamic load increases. Consequently, the area moment of inertia, I, and the flexural rigidity, EI, increase as one moves inboard along the wing. Therefore, it is likely that the increased flexural rigidity will help the inboard portion of the wing compensate for the loss of the inertial loading of the fuel than is the case near the wingtip. Overall, it is likely that there would be less change in both the wing twist and wing deflection. Still, the more rigid wing will show less change in the twist and deflection.

The impetus behind this work is to determine if there is a degradation in the aircraft's aerodynamics. It is then necessary to look at the spanwise lift distribution and the pressure distribution at various fuel loadings. For brevity, the 46-ksi and 180-ksi wings are examined. The spanwise lift distribution of the 46-ksi and 180-ksi wings at several fuel loads is shown in Figures (88 – 91).

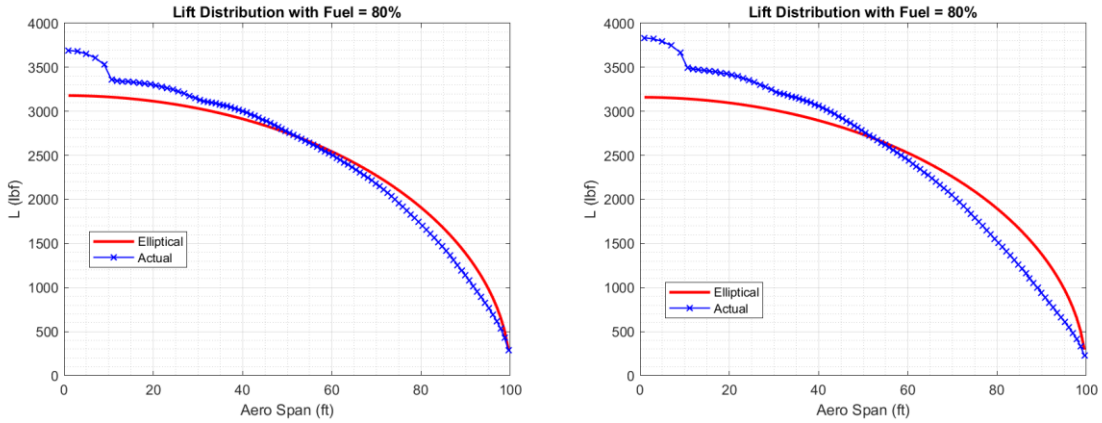

Figure 88. a) Spanwise Lift Distribution of 46-ksi Wing. b) Spanwise Lift Distribution of 180-ksi Wing.

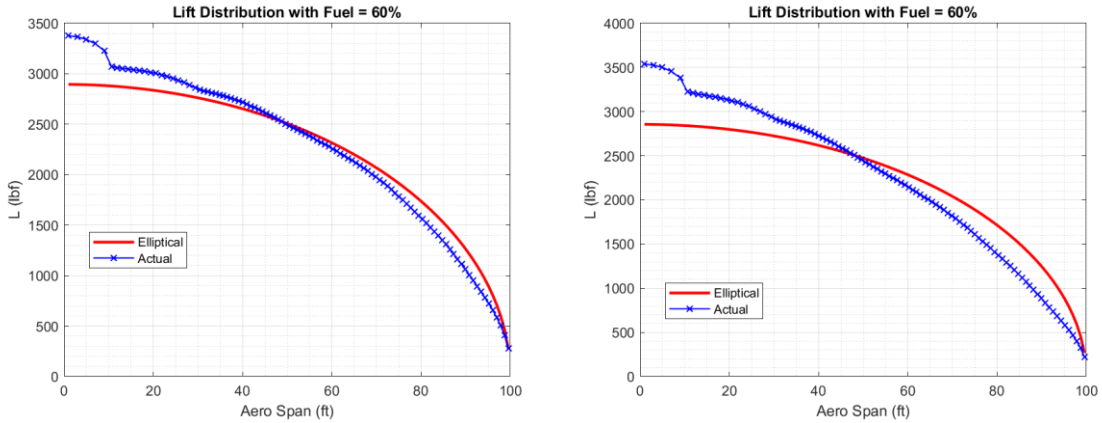

Figure 89. a) Spanwise Lift Distribution of 46-ksi Wing. b) Spanwise Lift Distribution of 180-ksi Wing.

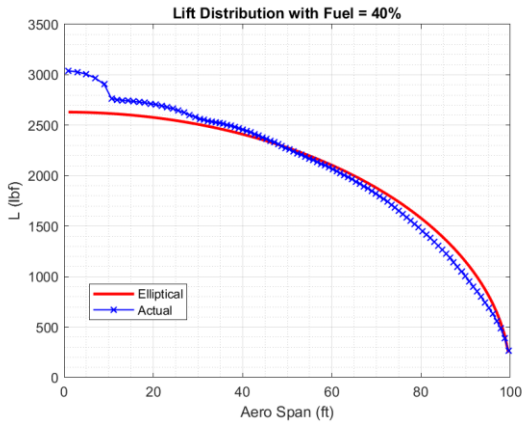

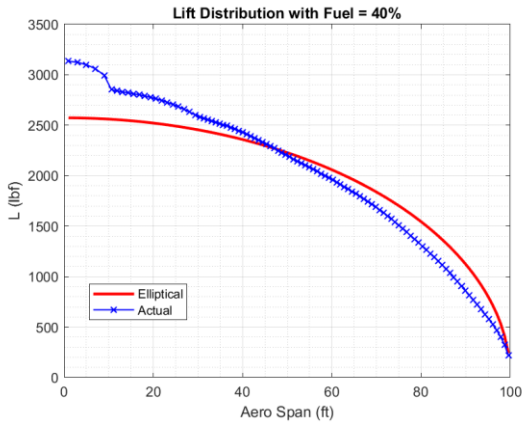

Figure 90. a) Spanwise Lift Distribution of 46-ksi Wing. b) Spanwise Lift Distribution of 180-ksi Wing.

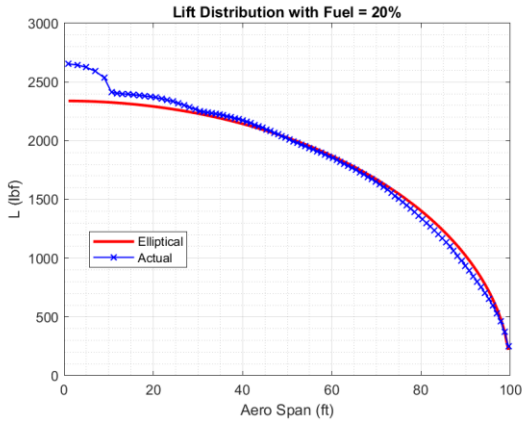

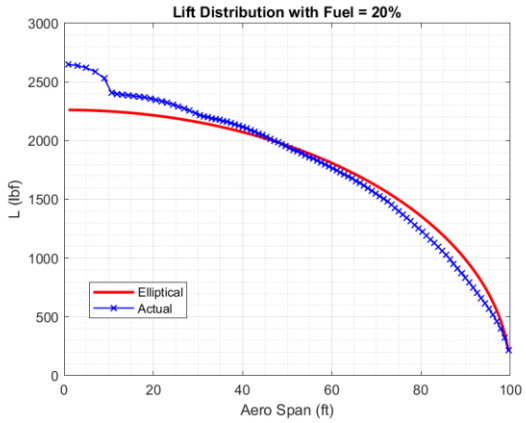

Figure 91. a) Spanwise Lift Distribution of 46-ksi Wing. b) Spanwise Lift Distribution of 180-ksi Wing.

The 46-ksi wing sees less degradation in the elliptical spanwise lift distribution than the 180-ksi wing. This is the case at the higher fuel loadings as well as the lower fuel loadings. In fact, by the 20% fuel load, the 46-ksi wing has almost recovered its elliptical lift distribution.

The lift-induced drag calculated by VORLAX for each wing at several fuel loadings is shown in Table (12).

Wing Model	Fuel Load = 100%	Fuel Load = 80%	Fuel Load = 60%	Fuel Load = 40%	Fuel Load = 20%
46-ksi	0.0214	0.0226	0.0234	0.0231	0.0228
69-ksi	0.0214	0.0229	0.0236	0.0240	0.0224
105-ksi	0.0214	0.0232	0.0239	0.0241	0.0232
180-ksi	0.0214	0.0236	0.0243	0.0243	0.0230

Table 12. Lift-Induced Drag (CD_i) at Several Fuel Loads.

The CD_i values in Table (12) show that the more flexible wings suffer more in terms of an increase in the lift-induced drag count as the fuel load decreases. The increase in the lift-induced drag is small, approximately 10 counts, when comparing the 46-ksi wing to the 180-ksi wing. However, when the main goal is to minimize the drag as much as possible, Table (12) shows that the more rigid wings minimize the lift-induced drag more than the more flexible wings. There is a bit of a discrepancy in the data at the 20% fuel load. The reason for this is not apparent. Nevertheless, the more rigid 46-ksi and 69-ksi wings exhibit less lift-induced drag over most of the fuel loading range.

When analyzing the lift-induced drag results shown above, one must realize that these values are found during a constant C_L fuel burn. The C_L is held constant by decreasing the dynamic pressure (q), which is done by increasing the altitude. If the lift-induced drag values are dimensionalized to account for the change in dynamic pressure, we get the values shown in Table (13).

Wing Model	Fuel Load = 100%	Fuel Load = 80%	Fuel Load = 60%	Fuel Load = 40%	Fuel Load = 20%
46-ksi	27,402 lbf.	26,471 lbf.	24,465 lbf.	22,014 lbf.	19,306 lbf.
69-ksi	27,402 lbf.	26,822 lbf.	24,674 lbf.	22,342 lbf.	18,968 lbf.
105-ksi	27,402 lbf.	27,173 lbf.	24,988 lbf.	22,435 lbf.	19,180 lbf.
180-ksi	27,402 lbf.	27,642 lbf.	25,406 lbf.	22,621 lbf.	19,015 lbf.

Table 13. Dimensional Lift-Induced Drag at Several Fuel Loads.

The results in Table (13) show the same conclusions drawn from the results in Table (12). The more rigid wings are better at minimizing the lift-induced drag over a range of fuel loads. The differences in the lift-induced drag, be it the drag coefficient or the drag force, are small when considering the size of the model aircraft. Yet, in this age of ultra-efficiency, every amount of drag that can be reduced should be considered.

The effect of the change in the wing twist on the lift-induced drag is not so straightforward. One must isolate the effect of the wing twist on CD_i from the reduction that occurs by the simple fact that the overall weight is decreasing and, therefore, the lift is decreasing. Furthermore, when one factors in that the lift and dimensionalized fuel loads are not the same for each of these models and thus the results shown here become a bit muddled. A more thorough analysis that keeps the total weight, and thus the total lift, consistent between the models is needed to gain further insight into what is shown in these tables. What is known is that an elliptical spanwise lift distribution minimizes the lift-induced drag at a given set of flight conditions. It is evident from Figures (88 – 91) that the more rigid 46-ksi wing better maintains the elliptical lift distribution compared to the more flexible 180-ksi wing.

In addition to lift-induced drag, the pressure drag associated with any formation or propagation of shockwaves will significantly impact the wings' aerodynamic performance. Recall Figures (80 – 83) showed the wing deflection of the 46-ksi and 180-ksi wings as several fuel loadings. Each wing showed a significant departure from the design wing deflection. This should, in turn, significantly impact the wing pressure distribution. Again, for brevity, the upper surface critical flow conditions for the 46-ksi and 180-ksi wings at several fuel loadings are shown in Figures (92 – 95).

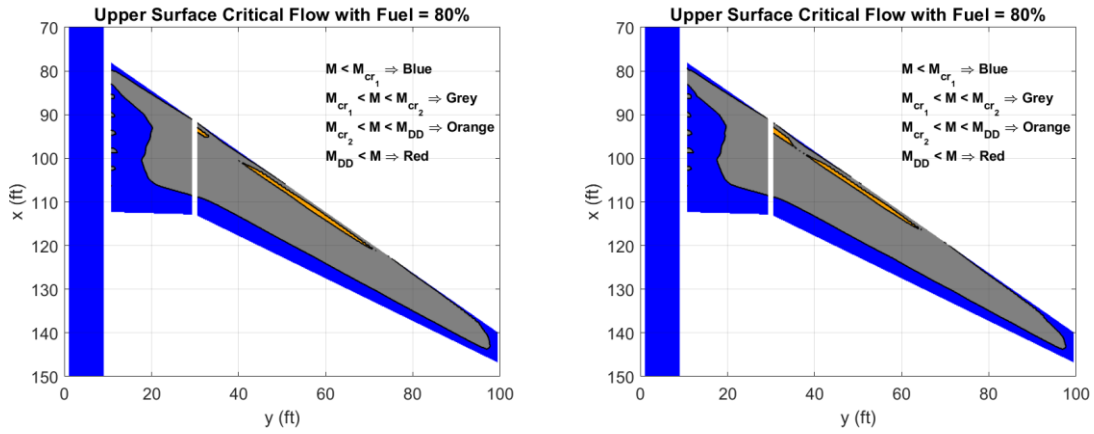

Figure 92. a) Upper Surface Critical Flow of 46-ksi Wing. b) Upper Surface Critical Flow of 180-ksi Wing.

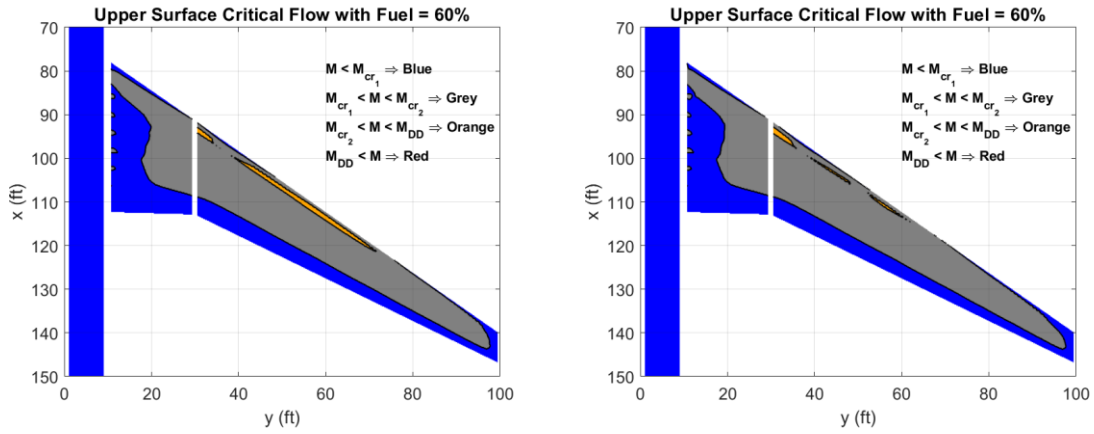

Figure 93. a) Upper Surface Critical Flow of 46-ksi Wing. b) Upper Surface Critical Flow of 180-ksi Wing.

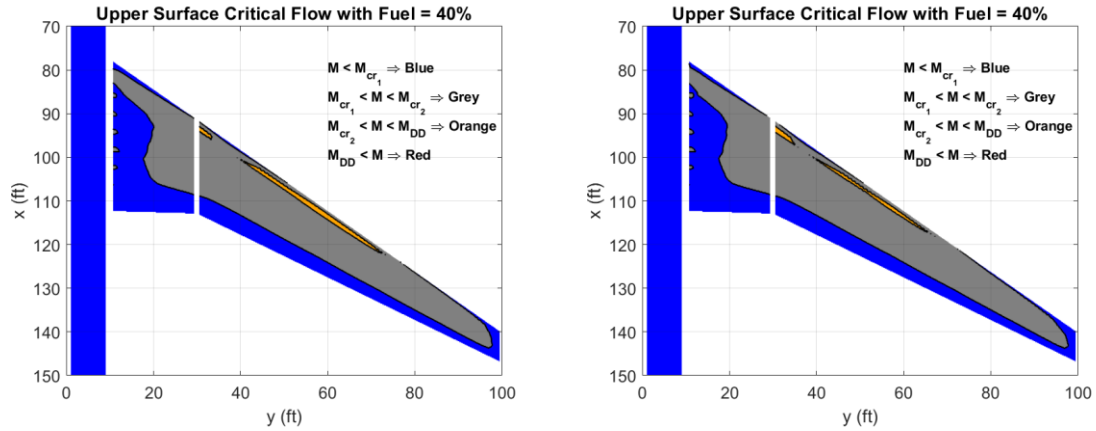

Figure 94. a) Upper Surface Critical Flow of 46-ksi Wing. b) Upper Surface Critical Flow of 180-ksi wing.

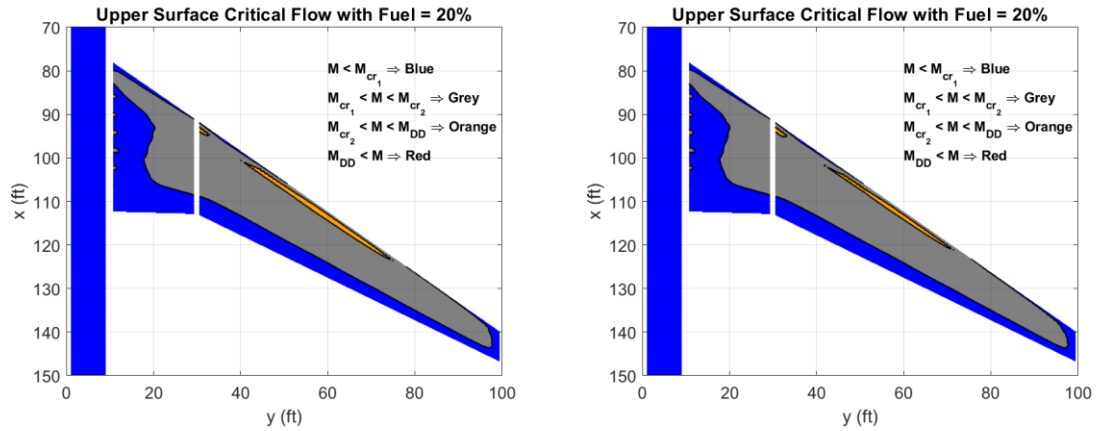

Figure 95. a) Upper Surface Critical Flow of 46-ksi Wing. b) Upper Surface Critical Flow of 180-ksi Wing.

Figures (92 – 95) yield some interesting results. The small portion of critical flow appears to be slightly larger for the 46-ksi wing. As the fuel load is decreased, the critical flow region of the 46-ksi wing remains relatively constant. On the other hand, the critical flow region(s) of the 180-ksi wing initially decreases with the decreased fuel load. The region(s) of critical flow eventually return as the fuel load decreases.

Nevertheless, this result is surprising. The upper surface pressure contours for the 46-ksi and 180-ksi wings are shown in Figures (96 – 99).

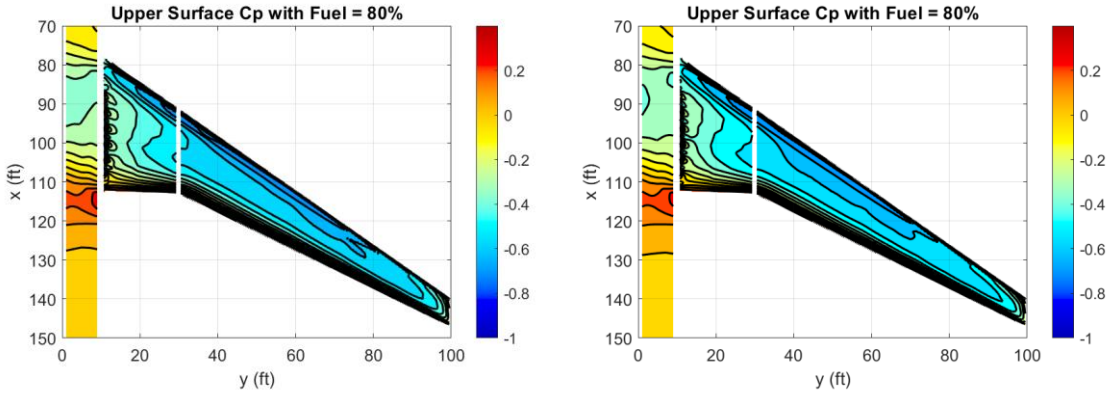

Figure 96. a) Upper Surface Pressure of 46-ksi Wing. *b) Upper Surface Pressure of 180-ksi Wing.*

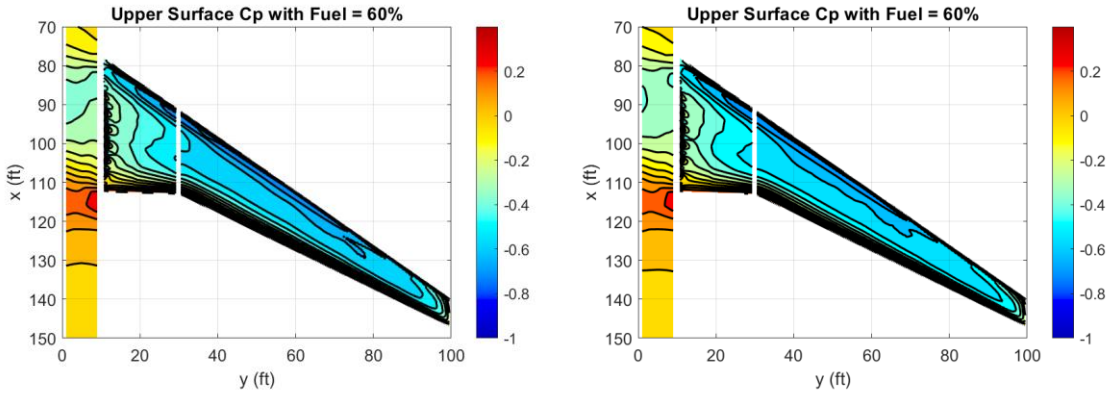

Figure 97. a) Upper Surface Pressure of 46-ksi Wing. *b) Upper Surface Pressure of 180-ksi Wing.*

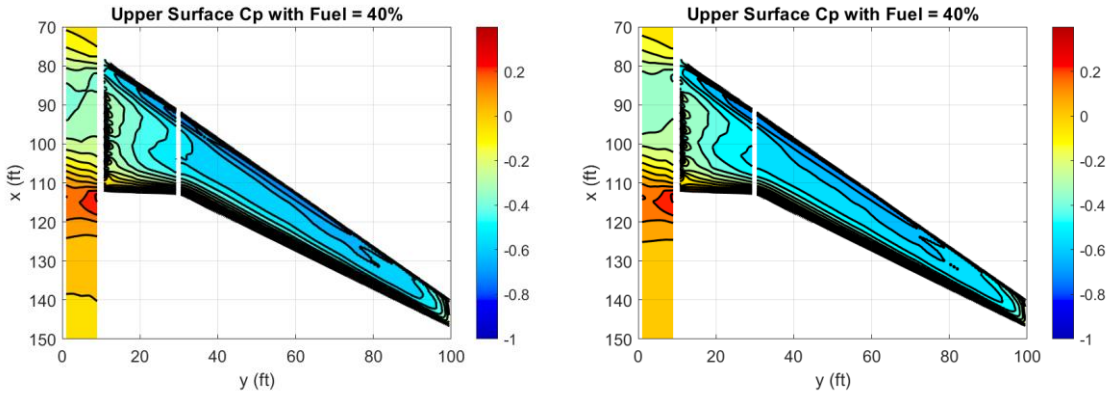

Figure 98. a) Upper Surface Pressure of 46-ksi Wing. *b) Upper Surface Pressure of 180-ksi Wing.*

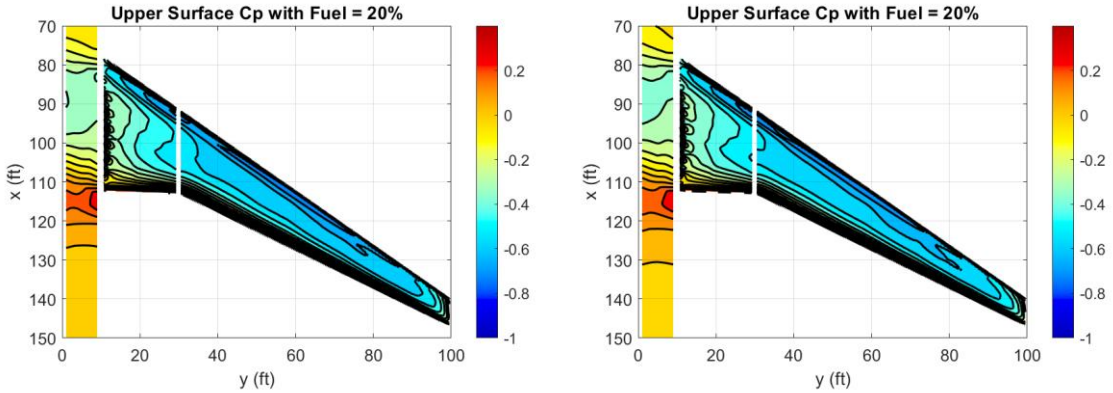

Figure 99. a) Upper Surface Pressure of 46-ksi Wing. b) Upper Surface Pressure of 180-ksi Wing.

It is minor, but the leading-edge of the 180-ksi wing does appear to be a slightly lighter shade of blue in the pressure isobar plots. This would indicate slightly lower leading-edge pressures, which correlates to the critical flow conditions shown in Figures (92 – 95). Finally, the maximum upper surface C_P for each wing at several fuel loadings is shown in Table (14).

Wing Model		100% Fuel	80% Fuel	60% Fuel	40% Fuel	20% Fuel
46-ksi	C_p	-0.726	-0.718	-0.721	-0.722	-0.730
	M_{cr}	0.776	0.779	0.778	0.778	0.775
69-ksi	C_p	-0.726	-0.715	-0.715	-0.726	-0.722
	M_{cr}	0.776	0.780	0.780	0.776	0.778
105-ksi	C_p	-0.726	-0.711	-0.705	-0.717	-0.726
	M_{cr}	0.776	0.782	0.784	0.780	0.776
180-ksi	C_p	-0.726	-0.707	-0.708	-0.704	-0.714
	M_{cr}	0.776	0.783	0.783	0.784	0.781

Table 14. Maximum Upper Surface C_P and M_{cr} for Each Model.

Table (14) shows that the maximum upper surface pressure decreases with the decrease in the fuel load for all the wings. This is not surprising since the aerodynamic load

decreases along with the dynamic pressure. What is unexpected is that the more flexible wings experience more favorable changes in the maximum upper surface pressure and critical Mach number. This may be due to the decreased wing twist that comes from the increased wing deflection. The decreased twist lowers the lift capability and, therefore, the pressure. Nevertheless, it is still unexpected.

It should be noted that these are only the maximum values. This study cannot measure any drag-related penalties from the critical pressure. It still may be the case that the more rigid 46-ksi and 69-ksi wings exhibit less pressure drag. This is something that should be explored.

CHAPTER 8

CONCLUSION

This work aims to determine what, if any, are the effects of a wing's static aeroelastic properties on an aircraft's aerodynamic performance. The inspiration to answer this question came from the aeroelastic properties of the Boeing 787 aircraft, which has an extreme amount of wing bending [1]. The extreme amount of flexibility seen in this aircraft was intentional and a consequence of the extensive use of carbon-fiber composite material in the construction of its wing [1][17]. Boeing uses active trailing edge control surfaces to change the aeroelastic response of the wing at different operating conditions and, therefore, can optimize the efficiency.

In theory, the extensive use of composite materials should show a reduction in structural weight, increasing fuel efficiency. This theoretical decrease in structural weight is based on traditional structural sizing techniques that focus almost exclusively on material tensile yield strength. Tensile yield strength is one of composite materials' big strengths. Other work has shown that the low compressive and shear strengths of composites may lead to an overly optimistic estimate of weight reduction [5]. Nevertheless, the effects of the thinner structural components, a direct consequence of a tensile yield strength-driven design, are studied. The results found are not exactly what was expected.

First, the extreme flexibility of the structurally thinner 105-ksi and 180-ksi wings required a more substantial amount of tuning to create a jig shape that could reproduce the design shape for cruise. However, a jig shape is found. At the design flight

conditions, all four material strength wings showed identical performance, as expected. The most noticeable differences occur at the limit maneuvering load cases of nZ_{max} and nZ_{min}. In these cases, all four wings showed significant drag divergence. On the other hand, the spanwise lift distribution of the stiffer 46-ksi and 69-ksi wings did show better adherence to an elliptical loading. This should help the more rigid wings maintain lower lift-induced drag at identical flight conditions.

When examining the nZ_{min} limit load, an unexpected behavior occurred with the more flexible 180-ksi wing. Instead of showing a downwards wing deflection, the wing was deflecting upwards. This, along with some behavior observed near a zero-gee loading, causes the author to suspect that there may be some non-linear behavior. Recall that linear elasticity is assumed, and one of the central assumptions of linear elasticity is small deformations. In some loading cases, it is suspected that the 180-ksi wing and possibly the 105-ksi wing are beyond the linear regime.

The most interesting result of this work is what is found when analyzing the aeroelastic effects of a decreasing fuel load. The weight of fuel, spread out along the wing, acts as a relief factor from the applied aerodynamic load. It helps to dampen the aeroelastic effects. The loss of this inertial relief is evident, particularly for the more flexible wings, at higher fuel loadings. However, it was found that as the fuel load continued to decrease, the reduced aerodynamic load began to catch up with the loss in inertial relief.

As expected, the elliptical lift distribution is better achieved over the range of fuel loads by the more rigid 46-ksi and 69-ksi wings. It is also found that because of the better

adherence to the elliptical loading, there is less of an increase in the lift-induced drag for the more rigid wings. The difference in the lift-induced drag between the rigid and flexible wings is small, between 5 to 10 counts, but in this era of ultra-efficiency, every count of drag matters.

The analysis of the upper surface pressure distribution as a function of decreasing fuel loads showed an unexpected result. The more flexible 105-ksi and 180-ksi wings at lower fuel loadings showed lower upper surface pressures. In the case of the 180-ksi wing, the region of critical flow that is initially seen dramatically decreases as the fuel load decreases. This region of critical flow does eventually return. This would suggest that the potential degradation of the aerodynamic performance of a more flexible wing, which was initially suspected, is not as significant as anticipated. In fact, the more flexible wing might have better performance.

While the effects of the decreasing fuel load on the upper surface pressure distribution are unexpected, these results are primarily qualitative. This work employed aerodynamic solvers that cannot calculate the pressure drag associated with shockwaves. A more thorough analysis is required to truly determine the effect of aeroelasticity on the pressure drag.

This work focuses on aerodynamic performance, but it should be noted that the excessive wing deflection seen in the more flexible wing may have severe implications on the aircraft's lateral stability and control characteristics. A more in-depth analysis focused on lateral stability should be explored.

Finally, the models used in this analysis were simple 1-D beam-element models. They neglected 2-D and 3-D structural effects. Furthermore, the solution process assumed that the wing was subjected to pure bending. Any torsional effects were ignored. A more detailed analysis should be done to fully understand the results found in this work and verify the results. This detailed analysis would incorporate a 2-D structural model that can account for aeroelastic torsion and bending. Although not necessary, more advanced CFD software could be used to verify the wing pressure distribution.

REFERENCES

[1] "What are the effects of the Boeing 787's very flexible wing?," [Online]. Available: https://aviation.stackexchange.com/questions/838/what-are-the-effects-of-the-boeing-787s-very-flexible-wings. [Accessed 20 October 2021].

[2] SA Flyer Magazine, "How Wing Washout Makes Your Airplane More Stable," 7 August 2020. [Online]. Available: https://saflyer.com/how-wing-washout-makes-your-airplane-more-stable/.

[3] M. M. Munk, The Principles of Aerodynamics, Washington, D.C.: Max Munk, 1933.

[4] M. Blair, "M.S. Thesis: Conceptual Composite Wing Design," Arizona State University, Tempe, AZ, 2021.

[5] M. C. Blair and T. T. Takahashi, "Optimal Composite Structural Design of Unmanned Aerial System Wings," AIAA 2022-4009, 2022.

[6] T. T. Takahashi and T. Lemonds, "Transport Category Wing Weight Estimation Using A Optimizing Beam-Element Structural Formulation," AIAA 2015-3374, 2015.

[7] T. Takahashi, Aircraft Performance and Sizing, Volume II: Applied Aerodynamic Design, New York, New York: Momentum Press, LLC, 2016.

[8] J. Jensen and T. Takahashi, "Wing Design Challenges Explained: A Study of the Finite Wing Effects of Camber, Thickness, and Twist," AIAA 2016-0718, 2016.

[9] J. D. Anderson, Fundamentals of Aerodynamics, Boston: McGraw-Hill, 2001.

[10] E. Obert, Aerodynamic Design of Transport Aircraft, 1 ed., Amsterdam: IOS Press, Incorporated, 2009.

[11] J. Kirkman and T. Takahashi, "Critical Mach Number Prediction on Swept Wings," AIAA 2017-0266, 2017.

[12] D. Küchemann, The Aerodynamic Design of Aircraft, Reston, VA: AIAA, 2012.

[13] S. Neumark, "Critical Mach Numbers for Thin Unswepts Wings at Zero Incidence," British ARC R&M 2821, November 1949.a

[14] K. W. Newby, "The effect of leading-edge modifications on the buffet boundary of the Avro Vulcan," British RAE Technical Memo Aero 441, 1955.

[15] Rolls-Royce, "Trent 1000: Boeing 787 Engine," [Online]. Available: https://www.rolls-royce.com/products-and-services/civil-aerospace/widebody/trent-1000.aspx#/. [Accessed 29 September 2022].

[16] GE Aviation, "GEnx Datasheet," 2004. [Online]. Available: https://www.geaerospace.com/sites/default/files/2022-01/GEnx-Datasheet.pdf. [Accessed 29 September 2022].

[17] The Boeing Company, "Boeing 787: By Design: Advanced Composite Use," [Online]. Available: https://www.boeing.com/commercial/787/by-design/#/advanced-composite-use. [Accessed 29 September 2022].

[18] L. Miranda, R. Elliot and W. Baker, "A Generalized Vortex Lattice Method for Subsonic and Supersonic Flow Applications," Lockheed-California Company, Burbank, 1977.

[19] T.J. Souders and T. Takahashi, “VORLAX 2020: Making a Potential Flow Solver Great Again,” AIAA 2021-2458, 2021.

[20] S. Donovan and T. Takahashi, "A Rapid Synthesis Method to Develop Conceptual Design Transonic Wing Lofts," AIAA 2010-9025, 2010.

[21] The Math Works, Inc., MATLAB (Version 2021a), 2021.

[22] I. H. Abbott, von Doenhoff A. E and L. S. Strivers Jr., "NACA TR-824: Summary Of Airfoil Data," 1945.

[23] MIL-HDBK-5J, "METALLIC MATERIALS AND ELEMENTS FOR AEROSPACE VEHICLE STRUCTURES," 2003.

[24] MIL-HDBK-17-2F, "COMPOSITE MATERIALS HANDBOOK: VOLUME 2. POLYMER MATRIX COMPOSITES MATERIALS PROPERTIES," 2002.

[25] M. C.-Y. Niu, AIRFRAME STRUCTURAL DESIGN: Practical Design Information and Data on Aircraft Structures, Los Angeles: Conmilit Press LTD., 1988

[26] United States of America, "Code of Federal Regulations: Title 14, Aeronautics and Space," 13 October 2022. [Online]. Available: https://www.ecfr.gov/current/title-14/chapter-I/subchapter-C/part-25/subpart-C/subject-group-ECFR3e855ea22ea15d0/section-25.337. [Accessed 15 October 2022].

[27] United States of America, "Code of Federal Regulations: Title 14, Aeronautics and Space," 13 October 2022. [Online]. Available: https://www.ecfr.gov/current/title-14/chapter-I/subchapter-C/part-25/subpart-C/subject-group-ECFRea44cbb3048b817/section-25.303. [Accessed 15 October 2022].

APPENDIX A

WIDEBODY AIRCRAFT DATA

List of Comparable Widebody Aircraft

Aircraft	MTOW	OEW	Max Payload	Overall Length
A350-900	623,906 lb	313,998 lb	309,908 lb	219.2 ft
A350-1000	696,661 lb	342,000 lb	354,661 lb	242.1 ft
A380-800	1,258,839 lb	628,317 lb	630,522 lb	238.62 ft
A340-300	606,271 lb	289,000 lb	317,271 lb	208.9 ft
A340-600	804,687 lb	384,000 lb	420,687 lb	245.3 ft
A330-900 (NEO)	553,000 lb	300,000 lb	253,000 lb	208.9 ft
B767-200ER	395,000 lb	181,610 lb	213,390 lb	159.1 ft
B767-300ER	412,000 lb	198,440 lb	213,560 lb	180.25 ft
B767-400ER	450,000 lb	228,000 lb	222,000 lb	201.33 ft
B747-400	875,000 lb	400,000 lb	475,000 lb	231.8 ft
B747-8	987,000 lb	485,300 lb	501,700 lb	246.8 ft
B787-8	502,500 lb	264,500 lb	238,000 lb	186 ft
B787-9	560,000 lb	284,000 lb	276,000 lb	206 ft
B787-10	560,000 lb	298,700 lb	261,300 lb	224 ft
B777-200LR	766,000 lb	320,000 lb	446,000 lb	209 ft
B777-300ER	775,000 lb	370,000 lb	405,000 lb	242.3 ft
B777-9X	775,000 lb	400,000 lb *	375,000 lb	251.8 ft

Comparison of MTOW and OEW of Comparable Widebody Aircraft

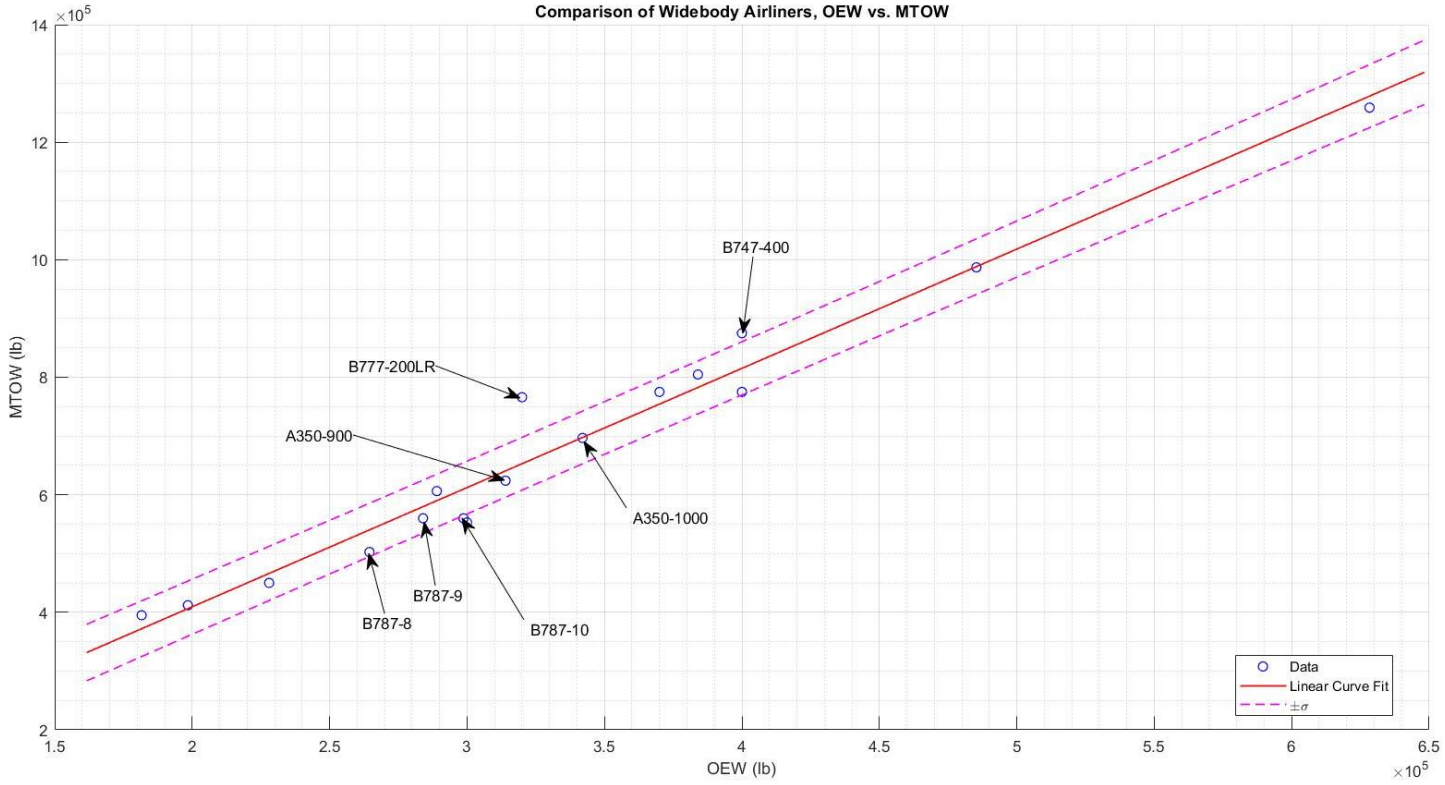

Comparison of MTOW and Overall Aircraft Length of Comparable Widebody Aircraft